PROTON CONDUCTIVITY STABILITY STUDIES BY MODELLING

LYNNDLE CAROLINE SQUARE

A thesis submitted in fulfilment of the requirements for the degree of Doctor Philosophiae in the Department of Physics, University of the Western Cape.

Supervisor: Prof. Christopher Arendse

November 2016

PROTON CONDUCTIVITY STABILITY STUDIES BY MODELLING

Lynndle Square

KEYWORDS

High temperature hydrogen fuel cell

Poly(2,5-benzimidazole)

Molecular modelling

Solubility

Miscibility

High pressure

Hydrogen bonded network

Mechanical properties

Phosphoric acid anion adsorption

Proton conductivity

ii

ABSTRACT

PROTON CONDUCTIVITY STABILITY STUDIES BY MODELLING

L. C. Square

PhD thesis, Department of Physics, University of the Western Cape.

In this thesis, some of the challenges experienced by high temperature polymer electrolyte membrane fuel cells are explored through material modelling techniques. A very important aspect for a fuel cell is that it should have high proton conductivity. As hydrogen enters a fuel cell it gets broken down into its constituents, protons and electrons. The electrons travel to an external load, whilst the protons travel through a diffusive layer, catalyst layer and membrane area, before recombining with oxygen to form water and leave the system. In this particular study, polytetrafluoroethylene and carbon form the diffusive layer, platinum the catalyst and poly(2,5-benzimidazole) doped with phosphoric acid the membrane area. The effects to proton conductivity are investigated as a result of the mixing of materials and adsorption of the phosphoric acid on the platinum active sites. A third study as an alternative avenue for proton conductivity improvements, is also explored. The results from these investigations promotes the idea that polytetrafluoroethylene, which is found in the ionomer layer, should be replaced as its mechanical properties decrease significantly with increase in temperature. Increasing pressure would further promote proton transfer over the doped polymer membrane region.
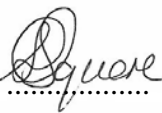
iii

Declaration

I declare that *Proton Conductivty Stability Studies by Modelling* is my own work, that it has not been submitted before for any degree or examination in any other university, and that all the sources I have used or quoted have been indicated and acknowledged as complete references.

Lynndle Caroline Square

November, 2016

Signed: ....

Acknowledgements

UNIVERSITY *of the* WESTERN CAPE

Contents

vii

List of Tables

UNIVERSITY *of the*

WESTERN CAPE

List of Figures

xii

Nomenclature

$[\overline{w}(n_i)]$ statistical weight $[\beta]$ reciprocal temperature

$[\breve{H}]$ Enthalpy $[L]$ Hill energy

$[R]$ Ray Enthalpy $[\chi]$ spin orbital

$[\delta]$ Solubility parameter $[F]$ Helmholtz free energy

$[\varepsilon_0]$ permittivity of free space $[\exp[-\beta U(\mathbf{r}^N)]]$ Boltzmann factor

$[\hat{H}]$ Hamiltonian operator $[\Lambda]$ Thermal de Broglie wavelength

$[\sigma]$ Stess Tensor $[\xi]$ Strain Tensor

$[\mu]$ chemical potential $[\mu]$ chemical potential

$[\nabla^2]$ Laplacian operator $[\phi]$ molecular orbitals

$[\Psi]$ multi-body wavefunction $[G]$ metric tensor

$[T]$ Transpose $[\tilde{Z}]$ charge of the nucleus

$[\varepsilon_{XC}[\rho(r)]]$ exchange-correlation energy $[\vec{a}]$ acceleration vector

$[\vec{r}_n]$ position vector $[C_{lmnk}]$ Elastic Stiffness Coefficient

$[D]$ Self-diffusion Coefficient $[dQ]$ heat added to system

$[dW]$ work done $[e]$ charge of an electron

$[E_n]$ particle energy $[h]$ Planck's constant

$[k_B]$ Boltzmann constant $[m_e]$ mass of an electron

$[m_n]$ mass of the nuclei $[N_e]$ number of electrons

$[N_n]$ number of nuclei $[PBI]$ Polybenzimidazole

$[S]$ Entropy $[s]$ spin eigenfunction

$[T]$ Temperature $[t]$ time

$[U(\vec{r})]$ potential energy function $[V_{cell}]$ Volume of Cell

$[Z]$ Partition function   [ABPBI] Poly($2,5$−polybenzimidazole)

[COMPASS] Condensed-phased Optimized Molecular Potentials for Atomistic Simulation

xiv

Studies

[FFT] Fast Fourier Transform

[HTPEMFC] High Temperature Polymer Electrolyte Membrane Fuel Cell

[LDA] local density approximation   [MD] molecular dynamics

[MEA] membrane electrode assembly   [MSD] mean square displacement

[PA] Phosphoric Acid   [PV] Photovoltaic

[REIPPPP] Renewable Energy Independent Power Producer Procurement Program

Chapter 1: Introduction

1.1   Energy Crises

The energy constraints currently experienced globally are as a result of the rapid population growth and the improved, energy dependent standard of living of many people [230]. In South Africa 88% of the energy mix is made up from coal electricity generation [229] and as a result South Africa is the 12th highest carbon dioxide emitter globally [232]. South Africa is currently experiencing national energy constraints and as a result power outages occur due to many reasons, and this despite an abundant supply of coal. To meet its current energy shortfalls and its commitment to reduce its carbon footprint, the Department of Energy (DoE) of South Africa has deployed initiatives to use alternative renewable energy resources to supplement their energy requirements.

Renewable sources are those derived from natural processes and are replenished at a rate faster than consumed. Renewable energy is produced from renewable sources in a sustainable manner. These energies include bioenergy, wind energy, geothermal energy, ocean wave energy, solar energy and hydropower [256]. The world total primary energy supply for 2013 is given in figure 1.1. Since 1973 the oil supply has decreased by approximately 15% , natural gas has increased by 5% and the use of coal and nuclear power have both grown by approximately 4% [255]. In comparison with 2012 , the following entities continued to grow year on year: biofuels and waste; natural gas and what is classified as other, which includes geothermal, solar, wind, heat etc [255]. Each of the renewable energy forms have limitations.

1
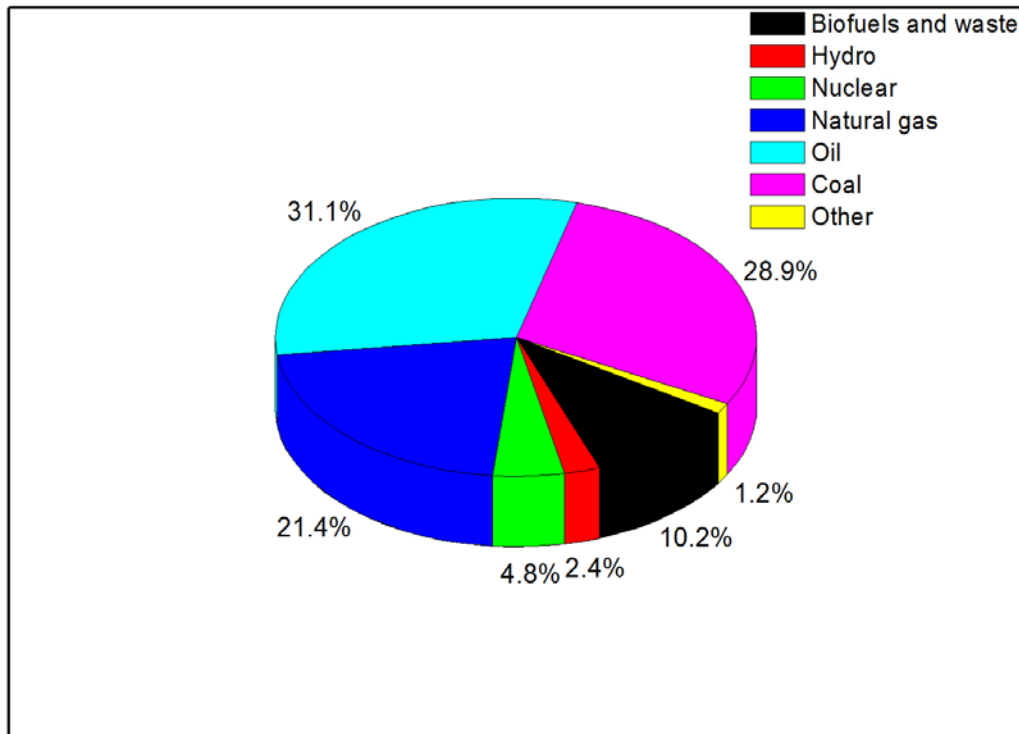
Figure 1.1: World total primary energy supply (2013) [255]

For any country what their renewable energy mix comprises of and the capital invested is dependent on the technological advances in a particular field, the natural resources and topographical features pertaining to it. In South Africa, announced in the DoEs annual performance plan (2015/2016) [233], one of the initiatives to change the country's energy mix is to increase its nuclear power generation. Six additional nuclear power stations are to be built which are anticipated to add $9600MW$ to South Africa's power generation capacity by 2020 [247]. The cost implication hereof would however not be favourable to the country. With regards to coal base-load power generation, figure 1.2 illustrates the eleven coal power stations that are currently in operation, as well the three coal power stations intended to return to service.

2

Eskom, South Africa's state owned enterprise, generates approximately 95% of its electricity and approximately 45% of the electricity used in Africa. It plans to add two more coal power stations. These two power stations, named Medupi and Kusile, are super-critical coal-fired power stations, intended to generate an output of $4764MW$ and $4800MW$ respectively [249]. Included in the country's planned new total energy mix is solar and wind power, both of which will feed into the national electricity grid as shown in figure 1.2. The DoE also intends to further strengthen work in the hydroelectric energy field [233].

UNIVERSITY *of the*
WESTERN CAPE

3

Eskom power stations
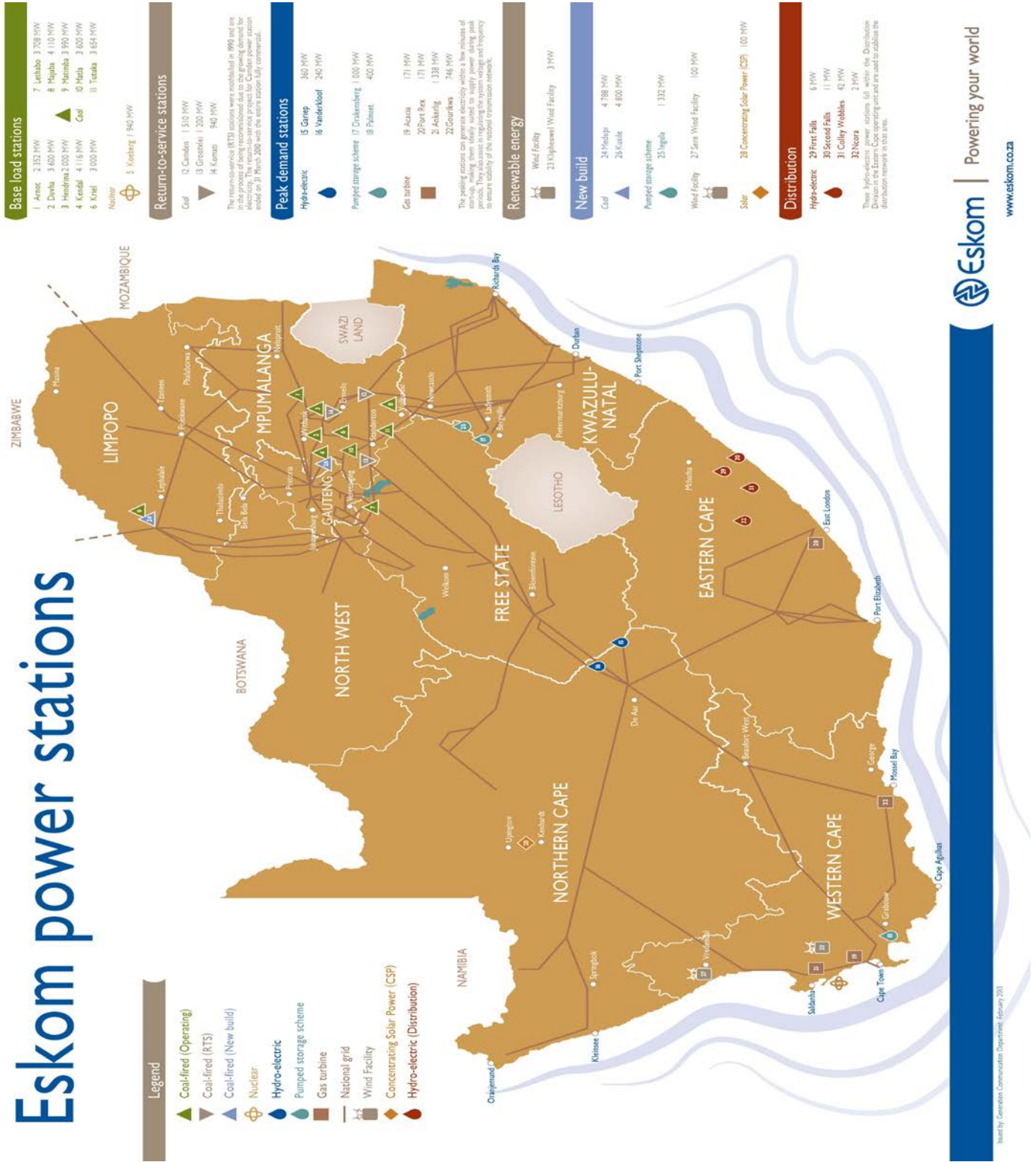
Figure 1.2: South Africa's national electricity energy grid and power stations provided by Eskom [248]

4

1.2   Solar Energy

The energy provided by the sun is the largest and most abundant form available to our planet. For many years it has been harnessed to produce light, heat and to grow food. For household heating and hot water supplies the sun's direct and diffuse rays can be used. Solar thermal technologies are used to concentrate rays to allow for the accumulation of high-temperature heat for a wide spread of applications [244]. According to Pascal et al [244] the peak solar radiation intensity on earth is in the region of $1kW/m^2$. A good solar power plant site can have a minimum of $2,500kW/m^2$, equivalent to an average $6.8kWh/m^2$ daily sunlight. Solar energy technologies in both thermal and electrical forms [214] utilise the energy from the sun. Solar thermal energy technology uses the power of the sun directly to heat water systems. Electrical solar energy includes a variety of techniques used to convert the energy found in sunlight to electrical energy [213].

The basis for solar thermal energy technology is dependent on the amount and the levels of global horizontal irradiation [216]. South Africa has solar resources which are amongst the highest in the world. It receives approximately $220W/m^2$ solar radiation, whereas only parts of the United States of America receives $150W/m^2$, and Europe and the United Kingdom receives $100W/m^2$ [216]. Figure 1.3 shows the country wide distribution of global horizontal irradiation, where areas with the highest concentration are found in the interior of the country [215]. The DoE South Africa is aggressively pursuing a national solar water heating programme, where according to Hon. Tina Joemat-Petterson, over one million homes over the medium term will be equipped with solar water heaters [233].

Solar thermal technologies rely on four basic components: a collector, receiver, transport storage, and power conversion part [244]. The three major solar-thermal technologies are parabolic trough, the central receiver and the parabolic dish. Table 1 lists the 5 concentrating solar power systems completed and/ or under construction. These are produced by the Renewable Energy Independent Power Producer Procurement Program

5

(REIPPPP) in South Africa.
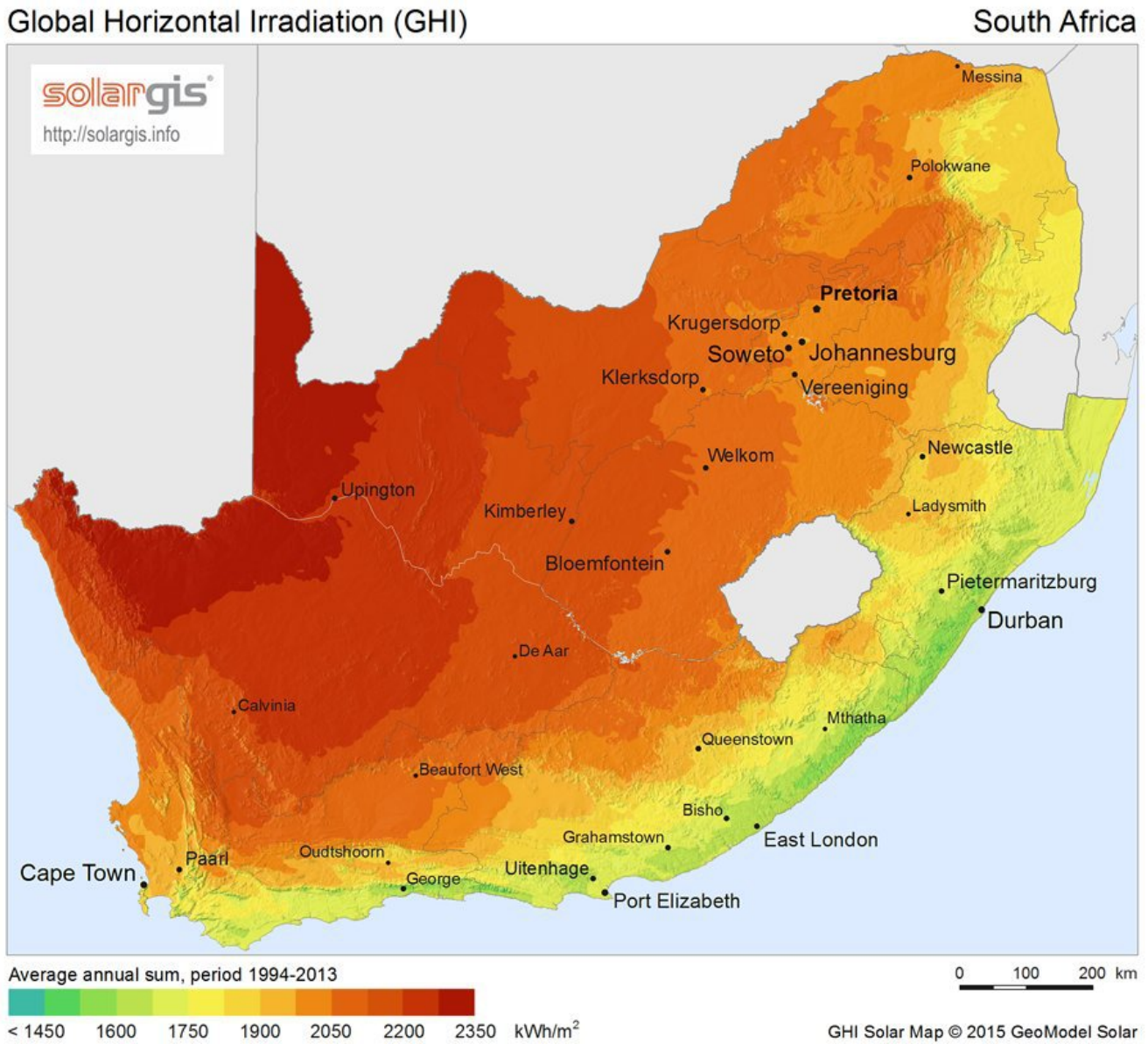
Figure 1.3: Solar GIS map of South Africa [215]

Project Name	Technology	Contracted Capacity (MW)
XiNa Solar One	Concentrated Solar Power - Parabolic trough	100
Bokpoort CSP project	Concentrated Solar Power - Parabolic trough	50
Ilanga CSP 1 / Karoshoek Solar One	Concentrated Solar Power - Parabolic trough	100
Kaxu Solar One	Concentrated Solar Power - Parabolic trough	100
Khi Solar One	Concentrated Solar Power - Power Tower	50

Table 1.1 REIPPP concentrating solar power systems projects [259][260]

An example of solar electrical technology include photovoltaic solar panels. A photovoltaic device differs fundamentally from heat engines in that it exploits a process called the internal photoelectric effect. The photoelectric effect is where through the absorption of photons, electrons from the valence band of a semi-conductor are excited into the conduction band [245]. Photovoltaic devices are therefore able to operate without emissions and requires little to no maintenance [244]. Photovoltaic, PV devices all have two basics components: a PV module and a mounting structure that supports the modules [244]. The limitation in PV technology is the high cost associated with it. Two approaches to reduce costs are to reduce the cost of the PV modules and/ or alternatively lenses or other optical devices can be used to focus the sunlight. A method used to reduce the cost of the modules have been to produce large areas of active material at a reduced cost [244]. These large areas of active material are known as a flat-plate system and have two categories, Crystalline and Polycrystalline Silicon Solar Cells and Amorphous Silicon Photovoltaic Thin Film systems [244]. Table 1.2 shows the number of Renewable Energy Independent Power Producer Procurement Program (REIPPPP) Photovoltaic Projects in South Africa as well as the technology used in production. The total 33 projects are contracted to produce approximately $1500MW$.

7

Project Name	Techonology	Contracted Capacity (MW)
Touwsrivier Solar Park	Photovoltaic Crystalline - Dual Axis	36
Adams Solar PV 2	Photovoltaic Crystalline – Fixed	75
Aries Solar Energy Facility	Photovoltaic Crystalline – Fixed	9.65
Aurora-Rietvlei Solar Power	Photovoltaic Crystalline – Fixed	9
Electra Capital (Pty) Ltd	Photovoltaic Crystalline – Fixed	75
Jasper Power Company	Photovoltaic Crystalline – Fixed	75
Kalkbult	Photovoltaic Crystalline – Fixed	72.5
Konkoonsies Solar Energy Facility	Photovoltaic Crystalline – Fixed	9.65
Lesedi Solar Photovoltaic Park	Photovoltaic Crystalline – Fixed	64
Letsatsi Solar Photovoltaic Park	Photovoltaic Crystalline – Fixed	64
Mainstream Renewable Power De Aar PV	Photovoltaic Crystalline – Fixed	45.6
Mainstream Renewable Power Droogfontein	Photovoltaic Crystalline – Fixed	45.6
Mulilo Solar PV De Aar	Photovoltaic Crystalline – Fixed	10
Mulilo Solar PV Prieska	Photovoltaic Crystalline – Fixed	20
Mulilo Sonnedix Prieska PV	Photovoltaic Crystalline – Fixed	75
RustMo1 Solar Farm	Photovoltaic Crystalline – Fixed	6.93
Slimsun Swartland Solar Park	Photovoltaic Crystalline – Fixed	5
Vredendal Solar Park	Photovoltaic Crystalline – Fixed	8.82
Boshoff Solar Park	Photovoltaic Crystalline - Single Axis	60
Dreunberg	Photovoltaic Crystalline - Single Axis	69.6
Greefspan PV Power Plant	Photovoltaic Crystalline - Single Axis	9.9
Herbert PV Power Plant	Photovoltaic Crystalline - Single Axis	19.98
Kathu Solar Plant	Photovoltaic Crystalline - Single Axis	75
Linde	Photovoltaic Crystalline - Single Axis	36.8
Mulilo Prieska PV	Photovoltaic Crystalline - Single Axis	75
Sishen Solar Facility	Photovoltaic Crystalline - Single Axis	74
Soutpan Solar Park	Photovoltaic Crystalline - Single Axis	28
Witkop Solar Park	Photovoltaic Crystalline - Single Axis	30
Pulida Solar Park	Photovoltaic Thin Film Fixed	75
Solar Capital De Aar	Photovoltaic Thin Film Fixed	75
Solar Capital De Aar 3	Photovoltaic Thin Film Fixed	75
Tom Burke Solar Park	Photovoltaic Thin Film Fixed	60
Upington Airport	Photovoltaic Thin Film Fixed	8.9

Table 1.2: Renewable Energy Independent Power Producer Procurement Program (REIPPPP) Photovoltaic Projects [259]

1.3 Hydropower

Hydropower utilizes the gravitational force on flowing water to drive turbines that generate electricity [238]. Dams are used as storage facilities to compensate seasonal shortfalls and increase water levels, which as a result raises the potential energy of the water [244]. For hydroelectricity the basic energy conversions are well understood; however factors that impact full exploration concern aspects of social and environmental nature in local communities, as well as the natural hydrology [244]. A baseline study on the micro hydropower potential in South Africa was done in an assessment conducted by the Department of Minerals and Energy (DME) [234]. As a result, it is evident that specific areas in the country have a significant potential for development of all categories of hydropower in the short and medium term. Figure 1.4 shows hydropower station locations in South Africa and whether they are decommissioned, and could potentially be refurbished or are operational, under construction or if the area has the potential for a station[226]. The areas of the Eastern Cape and KwaZulu-Natal provinces hold significant capacity and notably, with the best potential for the development of small, hydropower stations(less than 10MW)[226].

Despite the many avenues to explore Hydropower in South Africa, a major limiting factor is that South Africa is a water scarce country [258]. In 2015 South Africa experienced one of the worst droughts to date where 5 of its 9 provinces were declared disaster areas towards the end of the year. This extraordinary weather has been attributed to the effects of one of the strongest El Niño events on record [257]. Mindful of this recurring event and the water constraints the country is experiencing, alternative methods to harness energy would most likely be considered first.

9
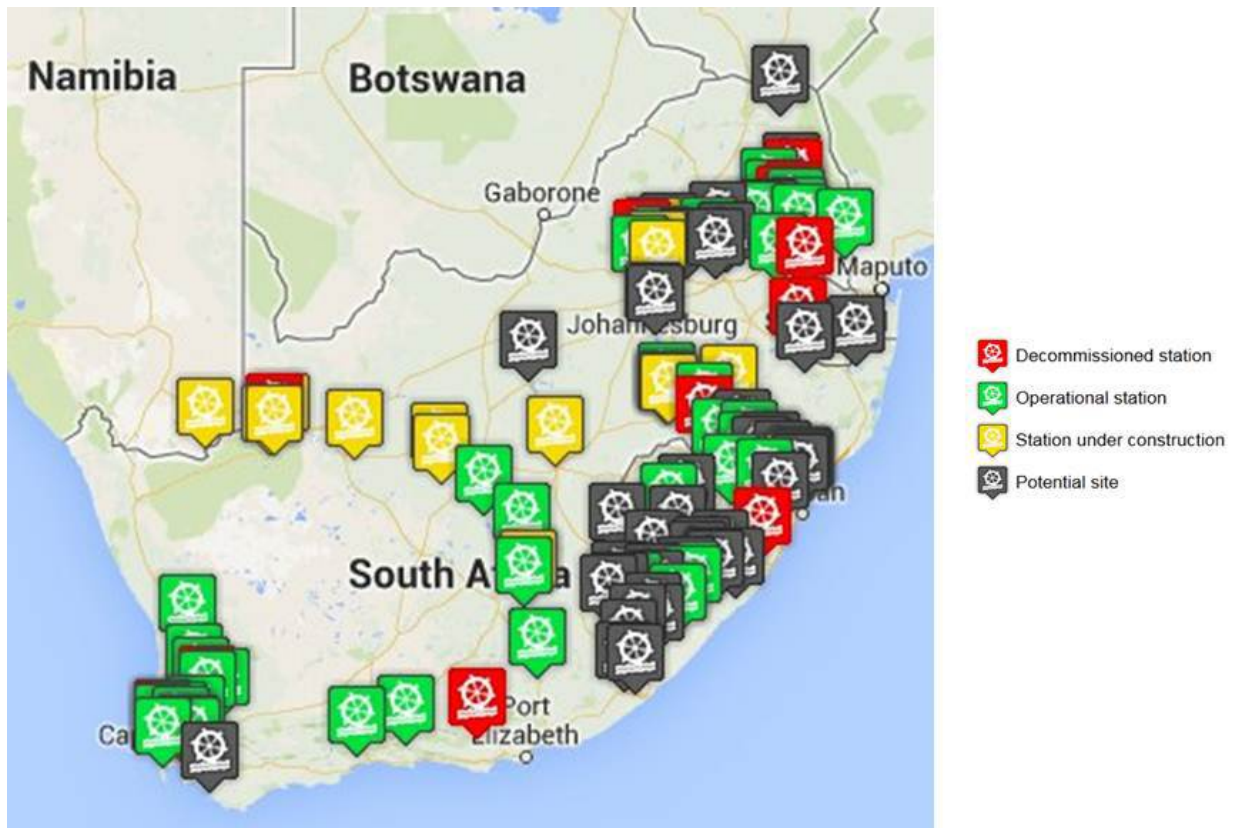
Figure 1.4: South African hydropower database [226]

1.4   Wind Power

Wind power, like hydroelectricity, is also of solar origin. Wind power and its strength is due to temperature differences between land, sea and air [244]. Electricity created as a result of wind power works on the following principle: wind turns the blades of a wind turbine, which in turn spins the shaft, which is connected to a generator and produces electricity [236]. Wind speed, the driving factor influencing the amount of energy derived, is affected by height of air flow, altitude and surface terrain [244]. In 1995, Daib [235] presented an estimate on the wind power potential in South Africa. Diab concluded that the potential in certain localised areas along the coast to be very good. In South Africa there are 22 REIPPPP onshore wind projects, which collectively produce almost $2000MW$.

10

1.5 Biofuel

In terms of the world energy usage, biomass/ plant matter contributes approximately 15% . In developing countries this percentile increases to 38% . The misfortune is that in most instances it is used inefficiently [244]. Biomass is a promising candidate since it can take on gaseous, solid and liquid forms which extends its application. According to Hall et al [244], urban migration can be curbed when biomass energy development fuels rural development and increases employment. A second benefit of biomass utilization is that an area's overall carbon footprint can be reduced. In liquid form biofuels are designed to replace petrol, diesel and coal. Much like these fossil fuels, as biofuels combust, energy is released that can be converted to motion in a car, or heating of a house. In South Africa biomass comprises of bagasse and field residue from the sugar industry, soft and hard wood from the forestry industry, chips, dust and bark from the saw mill industry, and black liquor, sludge and bark from the pulp and paper industry [234]. Most of the country, excluding most parts of the Northern Cape and parts of the Western, Eastern and Free State are able to yield $1 - 50 GJ/ha/yr$ [239]. The constraint on biomass contribution is ultimately limited by the land and water resources available.

In the Department of Energy of Republic of South Africa, Annual Performance Plan (2015/2016) [233], it states that the DoE intends to make it mandatory for crude oil refining companies to blend biofuels into petrol and diesel as of 2015. This enforcement gives surety for biofuel and biodesiel producers that the blended product will reach the market through oil providers. The potential for job creation will also increase as the industry grows. The immediate discussions involve reaching and finalizing a subsidy framework for the manufacturers, and an attractive price point of blended product for the end user.

1.6 Wave Energy

A natural form of energy can be extracted from the world's ocean waves, tides, thermal and salinity gradients. The overall consensus is that despite the total energy flux being so great only a small fraction would be usable in the near and foreseeable future. Cavanagh et al [237] pins this down to two reasons; the area over which the energy is diffused is large and the equipment required to harvest it would be large and costly, secondly, frequently the areas where the energy can be provided is remote and far from areas for consumption. Ocean thermal energy is limited to tropical regions and is in the prototype stage [244]. Salt gradient was once of great interest but it is said to be unlikely to be exploited in the near future. Tidal energy technology has been proven to be a dependable and long lived source of power [244]. Of the four ocean energy forms, the least explored is wave energy. The Cape coastline, in particular the Cape Peninsula, has great wave power potential. From about 900 km of the countries coastline, South Africa can produce an average energy intensity in the region of 25 MW/km [240]. In the medium term, due to costs and lack of technological resources wave energy is unlikely to be executed on a large scale.

1.7 Fuel Cells

From the preceding sections it becomes evident that renewable electricity production is limited by the intermittent nature of solar radiation and wind energy [244]. This dependency however limits applications in areas of transportation. To serve the fluid fuel market and transportation a renewable energy source is required that can be converted to an energy carrier that be easily stored and transported. Fuel cells, some of which use hydrogen as fuel, have been used for diverse applications including transportation vehicles, backup power devices, astronautical applications and residential micro-combined heat and power units, amongst others [244]. Globally there has been an increase in the number of hydrogen refuelling stations and in the variety of vehicle options, making the transition from petroleum/diesel based vehicles easier.

12

A hydrogen economy is one where hydrogen is used as an energy source. Hydrogen is used as fuel in an electrochemical device called a fuel cell. A fuel cell converts the chemical energy of a fuel directly into electrical energy. As an energy carrier, hydrogen has low polluting properties and has an above average efficiency for heating, transportation and power generation [244]. Hydrogen plays an important role in embarking on zero emission vehicles, and its advantage over electric battery vehicles is that refuelling times are substantially less and storage systems are less bulky, lighter and cheaper [244].

In most fuel cells the key element for the catalyst layer is from the platinum group metals. Over 80% of platinum deposits can be found in South Africa [243]. According to research by Cawthorn [228], using current mining techniques, the Bushveld Complex area in South Africa could supply the world demands for many decades, or even a century. This is an excellent opportunity for socio-economic upliftment for the country. It is with this mind that the South African Department of Science and Technology (DST) established three competence centres to implement the Hydrogen South Africa (HySA) strategy [242]. The objective of these competence centres is such that collectively, South Africa could provide 25% of the global platinum group metal based catalyst demand by 2020 [242].

1.7.1 Fuel Cell History and Development

William Grove (1811-1896), a Welsh lawyer, developed the wet-cell battery in 1838 [217]. The wet-cell battery later became known as the "Grove cell", consisted of two electrodes, one made of platinum which was immersed in nitric acid, and another made of zinc and immersed in zinc sulphate [217]. In 1889 Ludwig Mond and Carl Langer built the first fuel cell prototype [217]. A century later, in the $1900s$ it became an area of intensive research. Fuel cells have thus been around for over two hundred years!

The development of the Nafion membrane by DuPont in the $1960s$ moved the hydrogen economy concept to a possibility at around the $1970s$ [197]. In the $1980's$ the British Royal Navy installed proton exchange membrane (PEM) fuel cells in their submarine fleet

for nautical applications [218]. Hereafter, PEM fuel cells have been extensively researched for transportation, stationary, and portable power market applications.

There are several types of fuel cells, each of which have been developed for a particular purpose. The proton exchange membrane fuel cells (PEMFC) were designed primarily for transportation applications, direct methanol fuel cells (DMFC) for portable power generation, and alkaline fuel cells (AFC) for space programs for producing electricity and drinking water for astronauts [196]. Phosphoric acid fuel cells (PAFC), molten carbonate fuel cells (MCFC) and solid oxide fuel cells (SOFC) are intended for stationary power generation applications [196].

1.7.2   Polymer Electrolyte Membrane Fuel Cell

Of the six fuel cell technologies, the polymer electrolyte membrane, also known as the proton exchange membrane fuel cell (PEMFC), is considered in this work. Its popularity is driven by diverse applications including cars, buses, backup power devices and residential micro-combined heat and power units. Fuel cells have gained an increasing popularity and according to the 2013 fuel cell market report, the global shipment of fuel cell systems increased by 26% year on year [208]. In 2012, light duty vehicles costs have been reduced by 80% since 2002. In the same time frame the durability of the fuel cell systems have doubled and the cost of electrolyser stacks has reduced by 60% since 2007 [207]. In the automotive industry Hyuandai started delivery of their ix 35 fuel cell electric vehicle to Europe in 2013 and in the US as of 2014. Honda and Toyota intend for the commercial release of their fuel cell electric vehicles to global markets as of 2015 [208]. There has also been a significant increase in residential applications as Japan launched their Ene-Farm residential fuel cell program [208].

14
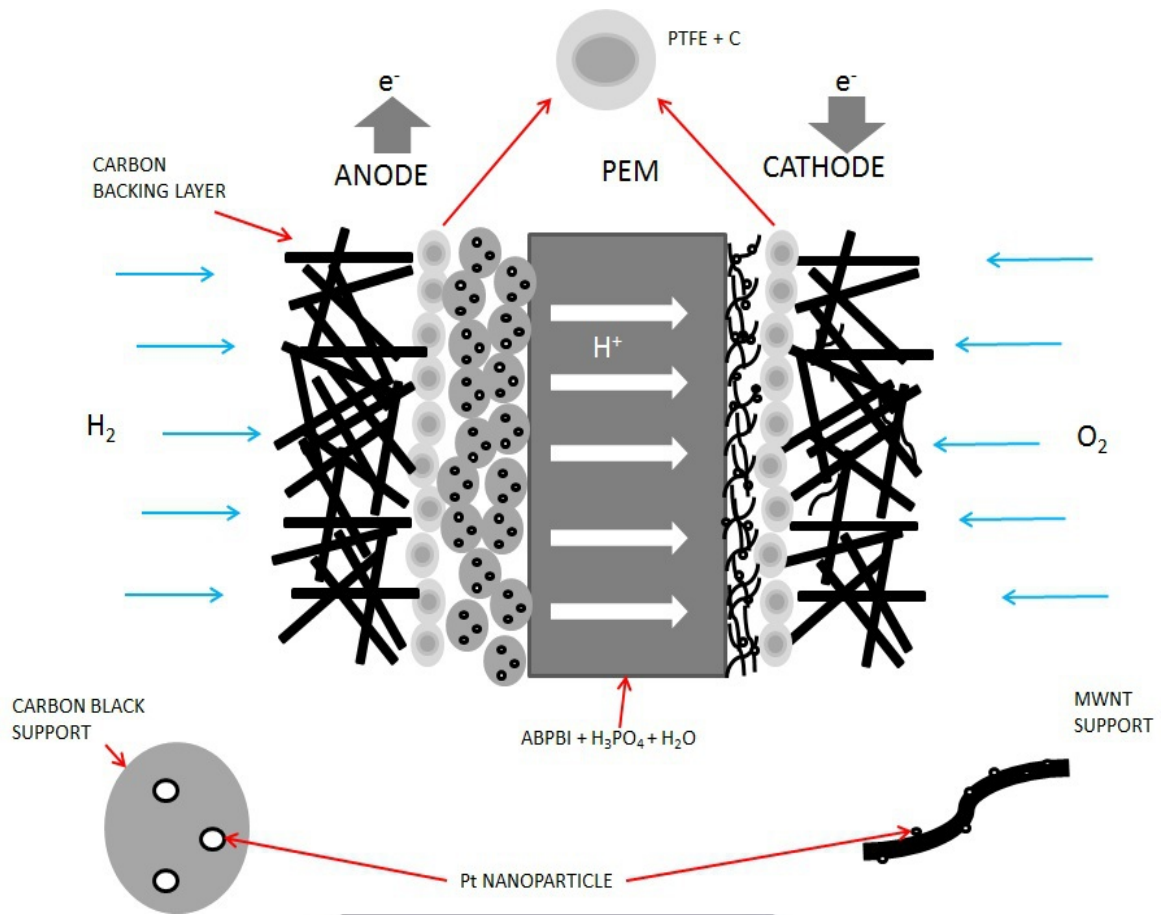
Figure 1.5: Schematic of the hydrogen fuel cell Membrane Electrode Assembly [193]

PEMFCs main features are: high power density, low operational temperature, pollution free operation and an all-solid construction, which implies less corrosion [219]. The first application of the PEMFCs was in the early 1960s in the Gemini space program [220]. To reach a stage where intensive commercialization is realisable is of great focus. Factors preventing this are that the fuel cells are high in cost and has poor durability.

A hydrogen fuel cell unit components are bipolar plates, anode and cathode flow channels, anode and cathode gas diffusion layers (GDL), anode and cathode catalyst layers (CL) and a membrane. Numerous fuel cell units form a fuel cell stack. The method in which a fuel cell operates, shown schematically in figure 1.5, is as follows; the hydrogen flows with respect to its channels, meets the electrode layer where it diffuses in the gas diffusion layer.

15

At the anode end the hydrogen is separated into protons and electrons. The electrons travel to the carbon cloth, flow field plate, to the contact, and then to the load. The protons travel through the polymer exchange membrane to the cathode. At the cathode catalyst layer, oxygen combines with the protons to form water and absorbing the electron [221]. An illustration of a high temperature fuel cell MEA with the specific materials discussed in this work is shown in figure 1.5 [193].

1.7.2.1 High Temperature Polymer Electrolyte Membrane Fuel Cell

PEMFCs' are further subdivided into two classes, low temperature PEMFC, (LTPEMFC) with temperature range from $[0-100°\,C]$ and high temperature (HTPEMFC), which is designed to operate in temperatures greater than $100°\,C$. HTPEMFCs is considered in all investigations to follow. When comparing the two classes, the advantage of operating at a higher temperature is that the oxygen electro-reduction rate at the cathode is faster, there is an improvement in the catalysts' tolerance to contaminants, in water management, gas transportation and heat rejection due to the difference in temperature between itself and its environment [222, 17]. A further disadvantage when operating at a temperature range below $100°\,C$, is that the catalyst of the fuel cell is susceptible to poisoning by even small amounts $(10\ \text{to}\ 100)$ part per million of carbon monoxide in the fuel stream [199]. In HTPEMFCs, since water is in its vapour form, an improvement in the overall stability and durability of the fuel cell system exists, and there is no longer a need to undertake complex shut down procedures previously required in the LTPEMFC.

The disadvantages of increasing the temperature is that elevated temperatures tend to stress the critical issues of thermal, chemical and mechanical stabilities of polymer materials, [222, 72]. The most significant fact is that without modification polymer membranes are incapable of operating at high temperatures because water from the membrane evaporates, resulting in a loss of proton conductivity [12]. High proton conductivity is crucial to achieve a high power density in fuel cells and therefore numerous approaches have been adopted to modify the polymeric membrane, in order to maintain the proton conductivity

16

as well as the performance of the membrane at high temperatures. Research into identifying a suitable polymer membrane for high temperature fuel cell application is an area of continuous investigation, primarily due to its incapability to be, without any modification done to it, competitive in terms of conductivity to that of Nafion in LTPEMFCs'.

Despite the ability of HTPEMFC's to provide improvements in water management, proper water management still needs to be taken into account. The significance of water management is that when the water content is too high it could flood the catalyst and porous transport layers. As a result the transportation of reactants is prevented. If the water content within a fuel cell is low then the polymer electrolyte membrane can become a poor proton conductor, and the reactivity at the electrodes is affected [188].

Dupuis et al   [196] formulated that there are two different approaches to realize anhydrous polymer membranes; to form an acid-base complex by impregnating a polymer membrane bearing basic sites with an acid, and secondly to use a polymer matrix containing protic ionic liquids. The focus of this study is thus the acid-base complex, and in particular poly(2,5-benzimidazole) (ABPBI), which is from the polybenzimidazole (PBI) family, doped with phosphoric acid (H_3PO_4) [250].

PBI membranes were proposed by Aharoni et al [202] and the phosphoric acid doped PBI membrane was suggested for fuel cell applications by Wainright et al [203] [204]. PBI is an amorphous thermoplastic polymer and is considered to be a basic polymer with excellent mechanical and chemical stability in temperature ranges greater than $100°$ C. Focus has been placed on the polymer because over and above the membrane application, it forms excellent textile fibres and has been used in blood-related dialysis and reverse osmosis at high temperature and harsh environments [219, 223].

H_3PO_4 is a weak acid that supports conductivity even in anhydrous conditions by forming

17

a hydrogen-bonded network [196]. Yan et al [17] states that H_3PO_4's ability to conduct protons in the anhydrous form is due to its proton-solvating ability and self-ionization behaviour. In other words, H_3PO_4 acts as a proton donor and acceptor in the membrane and plays a vital role in proton transport [224].

The challenges discovered with the development of reliable ABPBI membranes doped with H_3PO_4 are the adsorption of phosphate anions on the catalyst, a high corrosion rate of the amorphous carbon catalyst support, dissolution and sintering of catalyst particles at high temperature, and an accelerated degradation of the membrane electrode assembly (MEA) to open circuit voltage in the no-load state [17]. From the study of He et al [205] it is evident that it is because of these acid molecules that the mechanical strength of the membrane deteriorates, and an increase in the gas permeability of the membrane exists. The mechanism whereby the acid molecules manage this is that it reduces the intermolecular forces in the polymer by increasing the distance of the polymer backbones. Li et al [72] found that over and above the fact that concentrated H_3PO_4 imposes slow kinetics for oxygen reduction on the cathode due to the strong adsorption effect of anions onto the active sites of catalysts, the solubility and diffusivity of oxygen is reduced. The loss and movement of H_3PO_4 occurs through different mechanisms such as diffusion, capillary transport, membrane compression, evaporation, leaking from the doped membrane, and leaching by condensed water during shutdown and cold start [72]. Scott et al [206] points out that the potential loss of acid into the fuel cell gas/ vapour exhaust streams is another issue associated with the use of H_3PO_4 as a doping agent. A further challenge is the development of reliable ABPBI doped with H_3PO_4 membranes, and incorporating the combination as a proton conducting ionomer.

1.8   Computer Modelling for HTPEMFCs

The manner in which the material properties and challenges to the proton conductivity are

investigated is done through material modelling. Modelling is considered an accepted, extensively researched and utilized method to numerically simulate structures, processes and properties based fully or in part on fundamental laws of physics. It plays an instrumental role in either supporting or replacing experimental studies. Modelling and simulation allow for a more efficient use of research and development resources as there is a better understanding of how and why a product or process occurs. It is because of the use of modelling that in many research fields there is a faster delivery of products to market and solutions to critical research problems can be addressed, as often the solutions lie in controlling or adapting the process or behaviour at a molecular level [41].

The flow of fuels and the electrochemical phenomena in PEMFCs feature length scales ranging from nanometres in the membrane to centimetres in the flow channels. Such multi-scale phenomena cannot be fully described by one set of equations and a hierarchy of modelling and simulation techniques exists for different length and time scales [225]. Modelling of the fuel cell flow channels and stack are many, some of which have been done by Pukrushpan et al [263], Berning et al [264], Kazim et al [265], Salim et al [266] and Saripella et al [267]. At the atomistic scale Zhang [261] and Paddison et al [262] discuss the fundamentals required to study materials and devices at this scale. Atomistic and multi-scale modelling are also numerous some of which include work done by Brandell et al [23], Selvan et al [188], Devanathan et al [22], Scott et al [206] and Quiroga et al [268].

1.9 Aims and Outlines of Thesis

The aim of this work to use modelling and simulation tools to study the material properties affecting proton conductivity of the high temperature phosphoric acid doped ABPBI membrane fuel cell. The challenges addressed are reviewed at a fundamental level. It is the hope that the results hereof would enable us to establish preventative measures against the current challenges and methods to improve the actual fuel cell performance.

19

An overview of the theory used is given in chapter 2. In chapter 3, because of the pivotal role phosphoric acid plays in MEA, its diffusive properties, solubility and activation energy is investigated. Various thermostats are used in this study to test, compare and as a result form the ground work for the molecular dynamics studies that follow. It has been found that without modification polymer membranes are incapable of operating at high temperatures as a result of water from the membrane evaporating and resulting in a loss of proton conductivity [12]. A disadvantage of increasing the temperature is that critical issues of thermal, chemical and mechanical stabilities of the polymer materials would have to be taken into account   [222, 72]. In chapter 4 the mechanical and solubility properties of the two polymers, ABPBI and polytetrafluorethylene (PTFE) at room and at an elevated temperature is studied. Chapter 5 investigates proton conductivity using an alternative approach, where the effects of increased pressure on the PEM structure is studied. The diffusion of H_3PO_4 which has been found to decrease under normal HTPEMFC operating conditions and it too is studied under the influence of increased pressure. The final chapter includes a study of the structural orientation, bond lengths and scanning tunnelling microscopy of the adsorption of phosphoric acid anions onto platinum, which gives valuable insight into the resultant structure formed due to acid leaking from the doped membrane and leaching by condensed water during shutdown and cold start [72].

20

Chapter 2:   Material Modelling

Material modelling can be considered to be a method whereby experimental procedures are performed computationally. Approaches vary in scale, complexity and levels of computing power required. This chapter aims to give a summary of the theory used in the investigations that follow. The mathematical description for the atomic movement and changes to a system is known as the multi-body wavefunction, $\Psi(\vec{r}_1,\vec{r}_2,\ldots)$, Ψ many-body wavefunction [140], where $\vec{r}_n$ are the position vectors of electrons and nucleons, n in a system. The joint probability, $\wp$, expresses the likelihood of two particles being at positions $\vec{r}_1$ and $\vec{r}_2$ at the time t [140] and shown by the following equation:

$$\wp(\vec{r}_1,\vec{r}_2,\ldots;t) \propto \Psi^*(\vec{r}_1,\vec{r}_2,\ldots,t)\Psi(\vec{r}_1,\vec{r}_2,\ldots,t). \tag{2.1}$$

The symbol * represents the complex conjugate.

The Schrödinger equation for a single particle influenced by a potential energy field equation reads as follows:

$$-\frac{\hbar}{2m}\nabla^2\Psi(\vec{r},t) + U(\vec{r})\Psi(\vec{r},t) = i\hbar\frac{\partial\Psi(\vec{r},t)}{\partial t}. \tag{2.2}$$

h represents Planck's constant, where $\hbar = h/2\pi$. ∇^2, known as the Laplacian operator, in Cartesian coordinates is given by:

$$\nabla^2 = \frac{\partial^2}{\partial x^2} + \frac{\partial^2}{\partial y^2} + \frac{\partial^2}{\partial z^2}, \tag{2.3}$$

and $U(\vec{r})$ the potential energy function. The time-independent Schrödinger equation reads as follows:

$$-\frac{\hbar}{2m}\nabla^2\Psi(\vec{r})+U(\vec{r})\Psi(\vec{r})=E_n\Psi(\vec{r}).\tag{2.4}$$

E_n is the possible energy in the n-th state and the term on the left-hand side is commonly known as the Hamiltonian operator, $\hat{H}$.

$$\hat{H}\Psi(\vec{r})=E\Psi(\vec{r}),\tag{2.5}$$

It portrays the signature of an eigenvalue problem where an operator is applied to an eigenvector and results in the product of an eigenvalue and eigenvector [138], [139]. In this instance Ψ is the eigenfunction and E the eigenvalue [139]. ψ forms a orthonormal basis set such that:
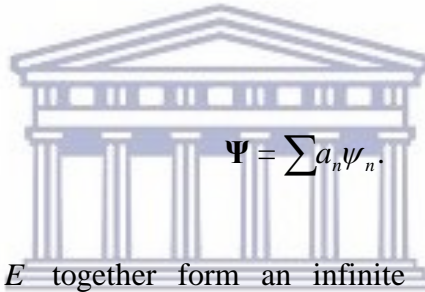
$$\Psi=\sum a_n\psi_n.\tag{2.6}$$

The solutions Ψ and E together form an infinite family of eigenfunctions and eigenvalues. To study the transformation of any material, Ψ would have to be calculated with respect to nucleon and electron degrees of freedom. Born-Oppenheimer [147] deduced that since the mass of an electron is significantly less than that of a nucleus, and is able to adjust its position with respect to the nuclei, the electrons and nuclei can strategically be studied separately. As a result of their work, Ψ can be rewritten as a product of electron and nucleon wavefunctions. The decoupling of Schrӧdingers' equation with respect to nuclei and electron components is as follows:

$$\hat{H}(R,r)\Psi(R,r)=E_n\Psi(R,r),\tag{2.7}$$

where R and r are the coordinates of the nuclei and electrons respectively. The Hamiltonian for a system consisting of the number of nuclei, N_n and number of electrons,

22

N_e is as follows [153]:

$$\hat{H}(R,r) = \underbrace{\sum_{\alpha=1}^{N_n} -\frac{\hbar^2}{2m_n}\nabla_\alpha^2}_{\text{Nuclear Kinetic Energy}} + \underbrace{\sum_{j=1}^{N_e} -\frac{\hbar^2}{2m_e}\nabla_j^2}_{\text{Electronic Kinetic Energy}} + \underbrace{U(R,r)}_{\text{Potential Energy}} , \qquad (2.8)$$

where m_n is the mass of the nuclei and m_e the mass an electron. For the Hamiltonian, the first two terms are representative of the kinetic energy of electrons and nuclei. The third term, the potential energy, is further expanded into corresponding components below:

$$U(R,r) = \underbrace{-\sum_{\alpha=1}^{N_n}\sum_{i=1}^{N_e} \frac{e^2}{4\pi\varepsilon_0} \frac{\tilde{Z}_\alpha}{|\vec{R}_\alpha - \vec{r}_i|}}_{U_{eN}} + \underbrace{\sum_{i<k}^{N_e} \frac{e^2}{4\pi\varepsilon_0} \frac{1}{|\vec{r}_i - \vec{r}_k|}}_{U_{ee}} + \underbrace{\sum_{\alpha<\beta}^{N_n} \frac{e^2}{4\pi\varepsilon_0} \frac{\tilde{Z}_\alpha \tilde{Z}_\beta}{|\vec{R}_\alpha - \vec{R}_\beta|}}_{U_{NN}}. \qquad (2.9)$$

For the potential, the first contributor U_{eN} represents the attractive electrostatic relationship between the nuclei and electrons. The second and third terms, U_{ee} and U_{NN} are repulsive potentials as result of the electron-electron and nuclei-nuclei interactions. $\tilde{Z}$ refers to the charge of the nucleus, e denotes the electron charge and ε_0 is the permittivity of free space. The equations used in the work to follow will be in the form where atomic units are considered, the conversion table can be found in appendix A.1.

2.1 Quantum Modelling, QM

When the electronic component is under investigation, the nuclear component is considered fixed and the wavefunction for all electrons in the system is considered. This still involves numerous solutions as energies arise from electron-electron and electron-proton interactions. The electron property of atomic excitation and de-excitation implies that electrons can exist in any number of states which further complicates the calculation.

23

2.1.1 Exact solution for Hydrogen atom

Due to its complexity, the Schrödinger equation can only be solved analytically for the hydrogen atom [137, 139]. The Hamiltonian corresponding to the hydrogen atom is:

$$\hat{H} = -\frac{\hbar}{2m}\nabla^2 + U_{eN},$$
(2.10)

where U_{eN} is also known as the Coulomb potential energy. To solve ψ the electron position has to be transformed into spherical coordinates, and separation of variables has to be applied. The Schrödinger equation in three dimensional spherical coordinates becomes [135] [136]:

$$-\frac{\hbar^2}{2m}\left[\frac{1}{r^2}\left(r^2\frac{\partial}{\partial r}\right) + \frac{1}{r^2\sin\theta}\frac{\partial}{\partial\theta}\left(\sin\theta\frac{\partial}{\partial\theta}\right) + \frac{1}{r^2\sin^2\theta}\frac{\partial^2}{\partial\theta^2}\right]\psi + U(r)\psi = E\psi,$$
(2.11)

where in spherical coordinates, $\psi = \psi(r,\theta,\phi)$. Through the implementation of separation of variables ψ is re-written such that

$$\psi_{nlm} = R_{nl}(r)Y_{lm}(\theta,\phi).$$
(2.12)

$R_{nl}(r)$ is considered to be the radial component and $Y_{lm}(\theta,\phi)$ the angular component. n,l,m are integer quantum numbers which corresponds to the size, shape and orientation in space of an atomic orbital respectively [134]. For the energy eigenvalue only the shell number/orbital size, n, also known as the principal quantum number, is required such that:
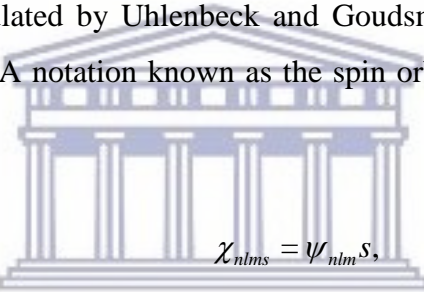
$$E = -\frac{\mu e^4}{8\varepsilon_0^2 h^2 n^2}$$
(2.13)

with

24

$$\mu = \frac{m_p m_e}{m_p + m_e}. \tag{2.14}$$

2.1.2 Multi-electron Systems

It becomes a challenging task to solve the Schr$\ddot{o}$dinger equation for multi-electron systems exactly [113]. Adding more electrons into the model for a calculation increases the number of interacting bodies, influences orbital motions and an account of electron spin would have to be incorporated. A method used to approximate a solution utilizes the variational principle as a platform. To fully describe the system, two additional postulates would have to be taken into account. One accounts for the fact that electrons have an intrinsic spin angular momentum, postulated by Uhlenbeck and Goudsmits [112] and the other is the Pauli exclusion principle. A notation known as the spin orbital, χ, aims to take this into account such that:

$$\chi_{nlms} = \psi_{nlm} s, \tag{2.15}$$

where $s = \alpha$ for up spin or β for down spin and is known as the spin eigenfunction. ψ_{nlm} is known as the spatial orbital [111]. The variational principle stipulates that for a trial wavefunction the expectation value for the energy will give an energy greater than or equal to the ground-state energy [97]. It is with this in mind that we can approximate solutions from trial solutions, determined by minimizing the expectation energy.

2.1.3 Common trial solutions to the wavefunctions, Ψ

Hartree-Fock proposed a trial solution to the $N-$electron wavefunction. This is known as the **Hartee product, HF** [133]:

$$\psi(1,2,3,\ldots,N) = \chi_1(1)\chi_2(2)\ldots\chi_N(N). \tag{2.16}$$

25

The pitfall of this form is that it does not obey the antisymmetry principle. The antisymmetry principle requires that when two particles are swapped an identical but negated wavefunction [133] is generated.

A method that can be used to ensure the results is negative on swapping, would be to use the determinant of the matrix. This is known as the so-called **Slater Determinant** [132] and is shown in the following form below:

$$\psi(1,2,\ldots,N) = \frac{1}{\sqrt{N!}} \begin{vmatrix} \chi_1(1) & \chi_2(1) & \ldots & \chi_N(1) \\ \chi_1(2) & \chi_2(2) & \ldots & \chi_N(2) \\ \vdots & \vdots & \ddots & \vdots \\ \chi_1(N) & \chi_2(N) & \ldots & \chi_N(N) \end{vmatrix}$$

Roothaan [108] and Hall [110] suggested the use of an orbital basis set to transform the Hartree-Fock equations into linear equations. ψ is modified such that:

$$\psi_i(r) = \sum_{v=1}^{K} c_{vi}\phi_v(r). \tag{2.17}$$

ϕ_v is known as a basis function and provides solutions to the wavefunction eigenfunction expansion. c_{ij} are coefficients determined through optimisation of variational minimization of the expectation energy. Roothan-Hall proposed the following relationship [110]:

$$\mathbf{FC} = \mathbf{SCE}. \tag{2.18}$$

26
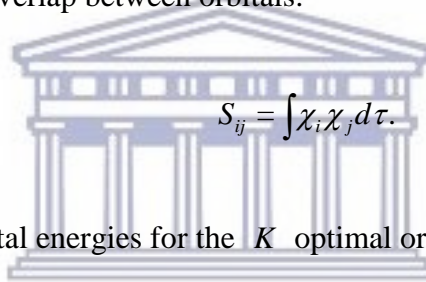
$$
\begin{aligned}
F_{\mu\nu} \quad &= \int d\mu_1 \phi_\mu(1) \left[-\frac{1}{2}\nabla_i^2 - \sum_{k=1}^{N} \frac{Z_k}{R_{1k}} \right] \phi_\nu(1) \\
&= \sum_{j=1}^{N/2}\sum_{\lambda=1}^{K}\sum_{\sigma=1}^{K} \left[2\int d\nu_1 d\nu_2 \phi_\mu(1)\phi_\nu(2)\left(\frac{1}{r_{12}}\right)\phi_\lambda(2)\phi_\sigma(2) \right] \\
&\quad + \sum_{j=1}^{N/2}\sum_{\lambda=1}^{K}\sum_{\sigma=1}^{K} \left[\int d\nu_1 d\nu_2 \phi_\mu(1)\phi_\lambda(2)\left(\frac{1}{r_{12}}\phi_\nu(2)\phi_\sigma(2)\right) \right]
\end{aligned}
\tag{2.19}
$$

The matrix **C** contains the coefficients to be determined:
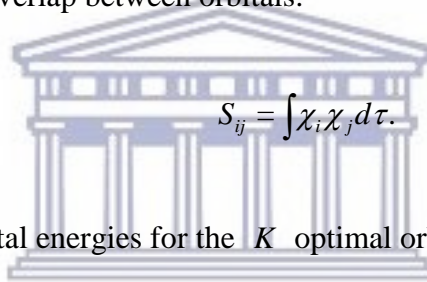
$$
C_{vi} = c_{vi}.
\tag{2.20}
$$

The matrix **S** gives the overlap between orbitals:

$$
S_{ij} = \int \chi_i \chi_j \, d\tau.
\tag{2.21}
$$

Finally, **E** gives the orbital energies for the K optimal orbitals that are determined:

$$
\mathbf{E} = \begin{pmatrix}
\varepsilon_1 & 0 & \cdots & 0 \\
0 & \varepsilon_2 & \cdots & 0 \\
\vdots & \vdots & \ddots & \vdots \\
0 & 0 & \cdots & \varepsilon_K
\end{pmatrix}
\tag{2.22}
$$

The Roothan-Hall equation are matrices which when solved gives back the optimal coefficients and orbital energies. The disadvantage of this method is that the equations must be solved iteratively since elements of both **F** and **S** depend on the resultant optimized coefficients. Further detailed descriptions and insight on the complexity and explanations on each of the coefficients can be found in books by Bort and Rusca [110], and Ramachandran et al [109]. To solve the Roothan-Hall equations numerically mostly involves computation Fock overlap matrices. An alternative approach is known as

27

Slater-type orbitals (STOs) [109], which are used to form the basis functions for ϕ_v. These have a general form[110]:

$$\phi_{\xi,n,l,m}(r,\theta,\varphi) = Nr^{n-1}Y_{l,m}(\theta,\varphi). \tag{2.23}$$

Where N is the normalization constant, r is the radial function, and is dependent on the nuclei electron distance, and Y is the spherical harmonic. An alternative to STO, and easier to compute, uses Gaussians to approximate the STO. These are known as **Gaussian type orbitals (GTOs)**.

2.1.4 Density Functional Theory (DFT)

An alternate Ab-initio method to the HF method is known as density functional theory (DFT) [118]. DFT works on the premise that the probability with which we expect to find an electron at a particular point and instant in time, gives significant properties of a molecule. For DFT, the ground state energy functional, which was first developed by Kohn and Sham [131], and later generalised by Levy [130], is given as follows:

$$E_t[\rho(r)] = \int V(r)\rho(r)dr + E_{KE}[\rho(r)] + E_H[\rho(r)] + E_{xc}[\rho(r)], \tag{2.24}$$

where

$$\rho(r) = \sum_{i=1}^{N} |\phi_i(r)|^2 \tag{2.25}$$

accounts for the density in terms of molecular orbitals ϕ.

$$\int V(r)\rho(r)dr = -\int \sum_{K=1}^{M} \frac{\rho}{|r_1 - R_k|} dr, \tag{2.26}$$

28

represents the interactions that electrons have with external potentials. This arises primarily from the interaction with the nuclei. The nuclei position is given by R_k. The second term, E_{KE}, is related to the molecular orbital as follows:

$$E_{KE}[\rho(r)] = \sum_{i=1}^{N} \int \phi_1(r) \left(-\frac{\nabla^2}{2} \right) \phi_1(r) dr. \tag{2.27}$$

This accounts for a system whereby electrons are non-interacting. The third term E_H, known as the Hartree term, is associated with electron - electron repulsive interactions. It is related to the molecular orbitals and 2.25 as follows:

$$E_H[\rho(r)] = \frac{1}{2} \iint \frac{\rho(r_1)\rho(r_2)}{|r_1 - r_2|} dr_1 dr_2. \tag{2.28}$$

The final term in equation 2.24 is known as the exchange correlation, for which there is no known exact solution. There are several approximations for this value, the simplest of which is known as the local density approximation (LDA). LDA for the exchange-correlation energy was based on the known result for the uniform electron gas [41], [129], [122]:

$$E_{xc}[\rho(r)] = \int \rho(r) \varepsilon_{XC}[\rho(r)] dr. \tag{2.29}$$

$\varepsilon_{XC}[\rho(r)]$ is the exchange-correlation energy per particle in a uniform electron gas, which Slater [128] describes in its simplest form as:

$$\varepsilon_{XC}[\rho(r)] = -(3/4)(3/\pi)^{1/3} \rho^{4/3}. \tag{2.30}$$

Approximations developed to a higher degree of complexity have been developed, some of which were done by Perdew and Wang [127], Gunnarsson and Lundqvist [126] and Von

29

Barth and Hedin [125]. Density gradient expansion is a method which improves on LDA by taking into account inhomogeneity of the electron gas, and is often referred to as the non-local spin-density approximation [41]. The variational principle is once again used to minimize the electron density functional, such that:

$$\frac{\partial}{\partial \rho(r)}\Big[E[\rho(r)] - \mu \int \rho(r)dr\Big] = 0,$$

(2.31)

where μ is a Lagrange multiplier. The purpose of μ is to guarantee that the density integral is constant and equal to the total number of electrons, N. This leads to what is known as the Kohn-Sham equation:

$$\left\{-\frac{\nabla_1^2}{2} - \left(\sum_{k=1}^{M}\frac{Z_k}{|r_1 - R_k|}\right) + \int \frac{\rho(r_2)}{|r_1 - r_2|}dr_2 + \frac{\partial E_{xC}[\rho(r_1)]}{\partial [\rho(r_1)]}\right\}\phi_i(r_1) = \varepsilon_i \phi_i(r_1).$$

(2.32)

The Kohn-Sham operator is therefore depended on the determination of molecular orbitals. The implementation of the Kohn-Sham method is explained in the following procedure, by Martin [107]:

1. an educated guess for $\rho(r)$ is made

2. the effective potential is calculated

3. the Kohn-Sham equation is applied to calculate a set of orbitals for ψ_i and respective energies ε_i. The self-consistent field calculation is used, an iterative procedure, to determine the orbital.

4. The value for ϕ is then used as input

5. the procedure is repeated at step 3 until the density converges.

2.2 Molecular Mechanics (MM)

30

QM methods are computationally expensive and for this reason are usually only applied to small systems of the order of 100 atoms [143]. For larger systems molecular mechanics (MM) can be used. For the nucleus component of the Schr$\ddot{o}$dinger equation, the above mentioned Born-Oppenheimer approximation is as follows:

$$\hat{H}(R,r)_{nucleus} \Psi(R,r) = E_{nucleus} \Psi(R,r), \tag{2.33}$$

where

$$E_{nucleus} = K + U_{pot}. \tag{2.34}$$

K and U_{pot} are the kinetic and potential energy, respectively. Using classical mechanics, Newtons second law for two particles is [142]:

$$\vec{F}_{net} = m\vec{a}, \tag{2.35}$$

where the resultant force, $\vec{F}_{net}$ relates the acceleration experienced $\vec{a}$, and the mass of an object. This force also has a relation to the potential energy as follows [150], [148]:

$$\vec{F} = -\frac{\partial U(\vec{r})}{\partial \vec{r}}. \tag{2.36}$$

In molecular dynamics, MD, $U(\vec{r})$ is broadly classified as the forcefield and generally given by the following equation [38]:

$$U = \sum_{S} U_b + \sum_{B} U_\theta + \sum_{D} U_\phi + \sum_{OOP} U_\chi + \sum_{NB} U_{LJ} + \sum_{C} U_{elec}. \tag{2.37}$$

U_b is the potential due to bond stretching, U_θ the potential due to bond bending to create

31

an angle θ between three atoms. U_ϕ considers the torsion angle, ϕ formed by four particles and its change with respect to an equilibrium position. The fourth term U_χ is a potential which considers angles formed between four particles where an inversion angle is formed. The last two potentials take into account non-bonded and Coulomb interactions.

2.2.1 Numerical Integration

The simplest, and usually the best [37] manner, to solve the equations of motions numerically is by using the Verlet algorithm, [149]. Its derivation utilizes the Taylor expansion and leads to [148]:

$$r(t+\delta T) \approx 2r(t) - r(t-\Delta t) + \frac{\vec{F}}{m}\Delta t^2 \tag{2.38}$$

and

$$\dot{\vec{r}}(t) = \vec{v}(t) = \frac{\vec{r}(t+\Delta t) - \vec{r}(t-\Delta t)}{2\Delta t} + \vartheta(\Delta t^2), \tag{2.39}$$

where $\vartheta(\Delta t^2)$ refers to terms of the order Δt^2.

2.3 Monte Carlo (MC) Method

The basic Monte Carlo method utilizes the Metropolis method [115]. In this method a process of a random walk is established such that:

$$\mathbf{r}^N \propto \exp[-\beta U(\mathbf{r}^N)]. \tag{2.40}$$

$\mathbf{r}^N$ describes a particular point in space and time. $\exp[-\beta U(\mathbf{r}^N)]$ [37] is known as the Boltzmann Factor, where:

32

$$\beta = \frac{1}{k_B T}, \tag{2.41}$$

and β is known as the reciprocal temperature. T is the absolute temperature [41]. $U(\mathbf{r}^N)$ is the energy of a particle. A manner in which a random walk can be implemented, shown in Frenkel and Smit [37] and as Metropolis describes it where, its energy is calculated once a particle is selected. The randomly selected particle is then given a random displacement and its new energy calculated. The move from $\mathbf{r}^N$ to $(\mathbf{r}+\Delta\mathbf{r})^N$ is accepted based on the following probability:

$$\wp_{\mathbf{r}^N \to \mathbf{r}+\Delta\mathbf{r}^N} = \min(1, \exp - \beta(U(\mathbf{r}^N) - U((\mathbf{r}+\Delta\mathbf{r})^N))). \tag{2.42}$$

For the application used later in this work, the software package Adsorption Locator, replaces $U(\mathbf{r}^N)$ with E_r, which denotes the total energy of a configuration r. E_r is calculated as follows [41]:

$$E_r = E_r^S + E_{SS} + U_r^S, \tag{2.43}$$

where E_r^S symbolizes the intermolecular energy between adsorbed molecules, E_r^{SS} the interaction energy between adsorbed molecules and the substrate and U_r^S the intramolecular forces between absorbed molecules. The probability function is now replaced with:

$$\wp_{r \to t} = \min(1, \exp - \beta(E_r - E_t)). \tag{2.44}$$

This says the minimum of "1" and the exponent will be chosen. The value "1" numerically signifies the current configuration. Therefore transitions to a lower energy,

$(E_t < E_r)$, are always accepted, but transitions to higher energy configurations, $(E_t > E_r)$, are only accepted with a probability which decreases exponentially when the difference energy is tending towards zero. Another transition configuration is then chosen and the same procedure implemented.

2.4 Statistical Mechanics

Statistical mechanics and thermodynamics form the fundamental framework for molecular dynamic simulations [114]. The number of atoms forming the building blocks of all nature is quantum by nature. These systems of building blocks have quantum states. The number of states for a "closed" finite system is finite, however, usually very large. In a closed system consider that every system is equally likely to be observed [37], [103]. It is because of this equally likely observation that all of equilibrium statistical mechanics and thermodynamics can be used.

To demonstrate how this comes about we start by considering a bag of infinite size where there are yellow blocks and black blocks [37]. We denote the number of yellow blocks by N_Y and the number of black blocks by N_B. The total number of blocks in the bag is denoted by N. The number of times N_Y and N_B can be drawn is given by:

$$\omega(N_Y, N_B) = \frac{N!}{N_Y! N_B!}.$$ (2.45)

If we consider $N_Y = N_B = N/2$, the above becomes

$$\omega(N/2, N/2) = \frac{N!}{(N/2)!(N/2)!}.$$ (2.46)

The best way to explain is by example, if we had a set $N = \{1,2,3\}$ and $P(N)$ be the

number of different ways in which we can write N, then $P(N) = 6$. i.e. $\{1,2,3\},\{3,2,1\},\{2,1,3\},\{2,3,1\},\{3,1,2\},\{1,3,2\}$. $P(N)$ in fact is $= N!$ [101]. For large N however, we use the Stirling approximation [96], [37], [106].

$$P(N) = N! = (N/e)^N, \tag{2.47}$$

alternatively written in the form of

$$\ln(N!) = N \ln N - N. \tag{2.48}$$

If we now have $P(N,n)$, the number of different ways of selecting n elements out of N elements is [101]:
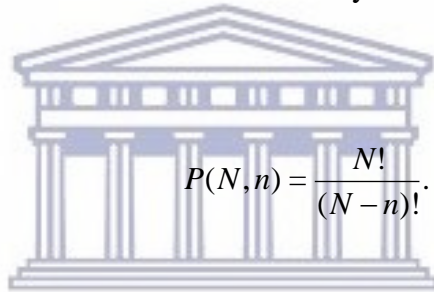
$$P(N,n) = \frac{N!}{(N-n)!}. \tag{2.49}$$

We have $C(N,n)$ the number of distinct groups of elements n from N.

$$C(N,n) = \frac{N!}{n!(N-n)!}. \tag{2.50}$$
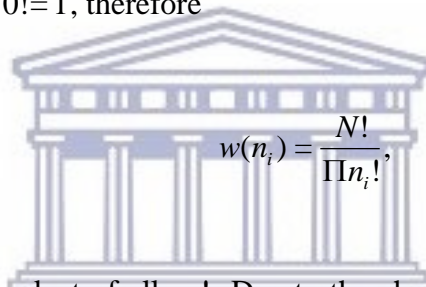
So if $N = \{1,2,3\}$ and we want $P(3,2)$ we have $(1,2),(1,3)(2,3)(3,2)(3,1)(2,1)$ therefore $P(3,2) = 6$. For $C(N,n)$ the number of distinct groups are $(1,2)(1,3)(2,3)$ and therefore $C(3,2) = 3$. These can also be calculated using equations, 2.49 and 2.50. We now have $w(n_1,n_2)$ which is the number of distinct ways of selecting two or more groups of a sample N:

$$w(n_1,n_2) = \frac{N!}{n_1!n_2!(N-n_1-n_2)!}. \tag{2.51}$$

35

If we had a system of N particles, these particles could be at different energy states and therefore we attempt to count the number of particles in each state. If the system of particles was to be subdivided into k groups according to the different energy groups then for each group k_i there would be n_i number of particles, i,e $n_i \in k_i$ and $\sum_{i=1}^{i=k} n_i = N$. If we were to now calculate $w(n_i)$ we would have

$$w(n_i) = \frac{N!}{n_1! n_2! \ldots n_i! (N - \sum n_i)!},$$ (2.52)

where $N - \sum n_i = 0$ and $0! = 1$, therefore

$$w(n_i) = \frac{N!}{\Pi n_i!},$$ (2.53)

where we let Π be the product of all $n_i!$. Due to the chaotic motion of all the groups k or micro-configurations, each is equally probable and therefore we are permitted to average [101]. This is also known as the statistical weight, $\overline{w}(n_i)$ $\overline{w}(n_i)$ statistical weight. The desired and most probable distribution is where $\overline{w}(n_i)$ reaches a maximum. To determine this the Stirling approximation, mentioned earlier, can be used when n is strictly greater than one. $\overline{w}$ can therefore be rewritten as:

$$\ln \overline{w}(n_1, n_2, \ldots n_i, \ldots) = N \ln N - N - \sum (n_i \ln n_i - n_i),$$ (2.54)

which leads to:

$$\ln \overline{w}(n_1, n_2, \ldots n_i, \ldots) = N \ln N - \sum n_i \ln(n_i).$$ (2.55)

36

We consider that in each energy state, ε_i, we have n_i particles. To determine the maximum, Lagrange multipliers is used [101]. The constraints are that the total number of particles and energy of the system has to be conserved [104], i.e

$$N = \sum n_i,$$ (2.56)

$$E = \sum \varepsilon_i n_i,$$ (2.57)

respectively. Let $f(n_i) = \ln \overline{w}_i$, which is subject under the constraints $g_1 = N - \sum n_i = 0$ and $g_2 = E - \sum \varepsilon_i n_i = 0$.

The Lagrange formula is
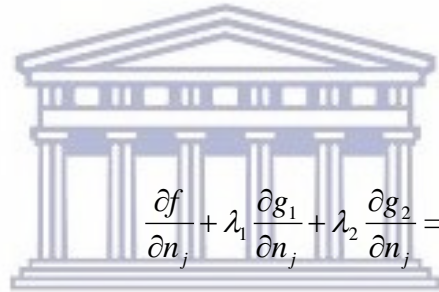
$$\frac{\partial f}{\partial n_j} + \lambda_1 \frac{\partial g_1}{\partial n_j} + \lambda_2 \frac{\partial g_2}{\partial n_j} = 0.$$ (2.58)

Now the partial derivative of w_i with respect to n_j, is

$$\frac{\partial f}{\partial n_j} = \frac{\partial \ln \overline{w}}{\partial n_j} = -\frac{n_j \ln n_j - n_j}{\partial n_j} = [\ln n_j + n_j(1/n_j) - 1] = -\ln n_j.$$ (2.59)

From the constraints we arrive at:

$$\frac{\partial g_1}{\partial n_j} = \frac{\partial}{\partial n_j}(\sum n_i - N) = 1,$$ (2.60)

and

$$\frac{\partial g_2}{\partial n_j} = \frac{\partial}{\partial n_j}(\sum \varepsilon_i n_i - E) = \varepsilon_j. \tag{2.61}$$

The resultant Lagrange equation is

$$-\ln(n_j) + \lambda_1 + \lambda_2 \varepsilon_j = 0. \tag{2.62}$$

Traditionally the notation for $\lambda_1 = \alpha$. λ_2 is found to be the reciprical temperature, β. The derivation of β can be found in, amongst others, "Statistical Mechanics and Properties of Matter: Theory and Applications" by Gopal [101]. Taking the exponential throughout this equation and making n_j the subject of the formula we arrive at:

$$n_j = \exp \alpha \exp \beta \varepsilon_j. \tag{2.63}$$

If we let $\exp \alpha = A$ and we know that $\sum n_j = N$, the above can be rewritten as $\sum [A \exp \beta \varepsilon_j] = N$. Since A is constant we have;

$$A = \frac{N}{\sum \exp \beta \varepsilon_j}. \tag{2.64}$$

We denote the denominator with Z such that

$$Z = \sum \exp \beta \varepsilon_j. \tag{2.65}$$
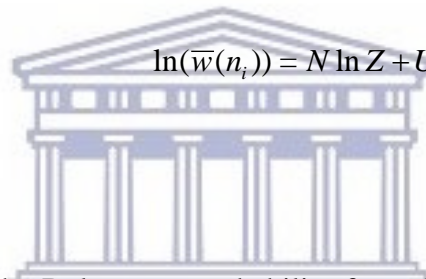
Z is known to be the partition function. Equation 2.64 would therefore mean that the total system divided by the number of partitions is constant. Substituting this into our value for n_i, we have:

$$n_i = \frac{N}{Z} \exp \beta \varepsilon_i. \tag{2.66}$$

38

The maximum of $\ln(w(n_i))$ in equation 2.54 can now be found. Using the system constraint equations 2.56, 2.57, and the above equation for n_i, $\ln(w(n_i))$ for a single particle becomes:

$$\ln(\overline{w}(n_i)) = N \ln Z + E\beta, \tag{2.67}$$

for a single particle. In thermal equilibrium with a heat reservoir, U, the internal energy of a system is the average value of E_i in a canonical ensemble. Canonical and other ensembles are discussed in the Thermodynamics section of this work, however this leads to

$$\ln(\overline{w}(n_i)) = N \ln Z + U\beta \tag{2.68}$$

for an entire system.

Concluding this section, the Boltzmann probability formula for a system to be in state of E_i is given by the following formula [101]:

$$\wp_i = \lim_{N \to \infty} \frac{n_i}{N} = Z^{-1} \exp \beta \varepsilon_i. \tag{2.69}$$

The normalization constant is such that:

$$\sum \wp_i = \sum \frac{n_i}{N} = 1. \tag{2.70}$$

When the partition function is calculated, often the ground states are considered only. This is primarily due to the separation between electronic states, which is significantly greater than the thermal energies [102].

39

2.5 Thermodynamics

The first law of thermodynamics accounts for the change in the internal energy of a system, dU [114].

$$dU = dQ + dW,$$ (2.71)

where dQ is the heat added to the system and dW the work done by the system. The heat added too, has the following relationship:

$$(dQ)_{rev} = TdS,$$ (2.72)

where S and T are known as the entropy and temperature of the system respectively. The subscript rev indicates that the process is reversible. The mechanical work done by a system is controlled by the volume variable such that:

$$(dW^{mech})_{rev} = -PdV.$$ (2.73)

The negative sign indicates that work is positive under compression. The chemical work done by increasing the number of particles is given by:

$$W_{chem} = \sum_{N_i = N_1}^{N_2} \mu(N_i),$$ (2.74)

where $N_2 > N_1$. μ is the chemical potential and N_i the number of particles. Therefore the total reversible work done by the system is:

40

$$(dW)_{rev} = (dW^{mech})_{rev} + (dW^{chem})_{rev} = -PdV + \mu dN. \qquad (2.75)$$

Therefore the change in internal energy can be rewritten as follows:

$$dU = TdS - PdV + \mu dN. \qquad (2.76)$$

To determine how the disorder of the system has changed, dS, the above is reaaranged to make the change in entropy the subject of the formula, i.e,

$$dS = \frac{1}{T}dE + \frac{P}{T}dV - \frac{\mu}{T}dN. \qquad (2.77)$$

From this it can be seen that entropy is directly related to the change in three control variables, N, V, E. Using the chain rule, dS can be rewritten as follows:

$$dS = \left(\frac{\partial S}{\partial E}\right)_{N,V} dE + \left(\frac{\partial S}{\partial V}\right)_{N,E} dV + \left(\frac{\partial S}{\partial N}\right)_{V,E} dN. \qquad (2.78)$$

Relating equations 2.77 and 2.78 the following relationships is established:

$$\left(\frac{\partial S}{\partial E}\right)_{N,V} = \frac{1}{T} \qquad (2.79)$$

$$\left(\frac{\partial S}{\partial V}\right)_{N,E} = \frac{P}{T} \qquad (2.80)$$

$$\left(\frac{\partial S}{\partial N}\right)_{V,E} = -\frac{\mu}{T}. \qquad (2.81)$$

Ludwig Boltzmann first proposed, which was later formalized by Max Planck, the relationship between entropy and the maximum of the statistical weight [104], [105]:

41

$$S(N,V,E) = k_B \ln w(N,V,E), \tag{2.82}$$

the Stirling approximation can once again be applied to arrive at

$$S = k_B[N \ln N - \sum n_j \ln(n_j)]. \tag{2.83}$$

Another function of state is the Helmholtz free energy, F, which has the following relationship with entropy:

$$F = U - TS \tag{2.84}$$

$$dF = dU - SdT - TdS. \tag{2.85}$$

2.6 Ensembles

At the quantum level consider a phase space, $[p,q]$, where p is the momentum and q the particles coordinates. For each degree of freedom $\Delta p \Delta q \rangle\rangle h$. The quasi-classical limit for the intervals between the neighbouring energy states of a system $\Delta E \approx E_{i+1} - E_i$ are extremely small and each state occupies a cell of volume h^f [101]. h raised to the power of f is indicative of the number of degrees of freedom.

In the number of states, dn, consider coordinates and momenta lying within intervals $\{q_v, q_v + dq_v\}$ and $\{p_v, p_v + dp_v\}$, where $v = 1;2;3;\ldots;f$. Consider the notation such that:

$$d^f p d^f q = \Pi_v dp_v \times \Pi_v dq_v, \tag{2.86}$$

where

$$\Pi_v dp_v = dp_1 \cdot dp_2 \cdot dp_3 \cdot \ldots dp_f \tag{2.87}$$

and

$$\Pi_v dq_v = dq_1 \cdot dq_2 \cdot dq_3 \cdot \ldots dq_f. \tag{2.88}$$

The number of states in a system is large such that $dn \rangle\rangle 1$ and determined by:

$$dn = \frac{d^f p\, d^f q}{h^f}. \tag{2.89}$$

For all dn states in the volume $(d^f p\, d^f q)$ the values of energy E_i can be replaced by an average value $E(p,q)$ [101]. The Hamiltonian for a system can be presented as a function of generalized $[p,q]$, $E = H(p,q)$. The Hamiltonian operator allows the use of this notation at each point in the phase space, which has a Boltzmann factor $\exp^{[-H(p,q)/k_B T]}$ associated with it. The quasi-classical partition function can therefore be rewritten as:

$$Z = \sum_i \exp\left(\frac{-\varepsilon_i}{k_B T}\right) = \frac{1}{h^f} \int \ldots \int_{2f} \exp\left(\frac{-H(p,q)}{k_B T}\right) d^f p\, d^f q. \tag{2.90}$$

The symbol $\int \ldots \int_{2f}$ denotes a volume integral in the phase space, where the limits of the integral are determined by the arrangement of the system.

Once the sample has been constructed and geometry optimization has been performed, a decision on what exactly needs to be determined from the experiment, needs to be refined. As with a physical experiment, in a simulated experiment the fluctuating of the chosen parameters needs to be carefully considered. This brings us to what is classified as ensembles. An ensemble is what is referred to as the average behavior of a many body

43

system over all possible quantum states [37], or alternatively referred to as a collection of configurations. As stated by Frenkel and Smit [37] "the idea behind Molecular Dynamics simulations is precisely that we can study the average behavior of a many-particle system by computing the natural time evolution that a system reaches numerically, and averaging the quantity of interest over a sufficiently long time". The *Ergodic Hypothesis* states that the time average yields the same as the average over the ensemble [154] i.e.

$$< X > = \lim_{t \to \infty} \frac{1}{t} \int_0^t X(t)dt = \lim_{M \to \infty} \frac{1}{M} \sum_i^M X_i, \qquad (2.91)$$

where M is the number of points.

An ensemble is classified by the variables that are kept constant, the independent variables, and those that are allowed to fluctuate, the dependent variables. The four major thermodynamical ensembles are listed in table 2.1, where the intensive variables are the chemical potential μ, the pressure P and the temperature, T. The extensive variables are the number of particles N, the volume V, enthalpy, $\breve{H}$ where $(\breve{H} = E + PV)$, Hill energy, L, where $(L = E - \sum \mu_i N_i)$ or Ray enthalpy, R, where $(R = E + PV - \sum \mu_i N_i)$ [78].

Ensemble name	Independent Variable	Dependent Variable
Microcanonical	NVE	μ PT
Canonical	NVT	μ PE
Grand-canonical	μ VT	NP L
Isothermal-isobaric	NPT	μ V $\breve{H}$

Table 2.1: Different thermodynamic ensembles

In each of these ensembles the partition function changes accordingly. The derivations and

44

explanations can be found in the books by Tuckermann [114] and Frenkel and Smit [37]. A summary of the partition function in MC simulations and in each of these ensembles can be found in table 2.2

Ensemble name	Partition Function
Microcanonical	$Q = c\int dp^N dr^N \delta(\mathrm{H}(p,q) - \varepsilon)$
Canonical	$Q = \dfrac{1}{\Lambda^{3N} N!}\int dr^N \exp\{-\beta U(r^N)\}$
Grand-canonical	$Q \equiv \sum_{N=0}^{\infty} \dfrac{\exp \beta\mu N V^N}{\Lambda^{3N} N!}\int ds^N \exp -\beta U(s^N)$
Isothermal-isobaric	$Q = \dfrac{\beta P}{\Lambda^{3N} N!}\int d\ln V V^{N+1}\exp\{-\beta PV\}\int ds^N \exp\{-\beta U(s^N; L)\}$

Table 2.2: Partition functions in thermodynamic ensembles for MC Simulations.

Λ is known as the thermal de Broglie wavelength where:

$$\Lambda = \sqrt{\frac{h^2}{(2\pi m k_B T)}},$$
(2.92)

and H, the Hamiltonian defined in equations 2.5 and 2.8. The s^N are the scaled coordinates and $L = V^{1/3}$.

2.6.1 Thermostats

With a microcanonical ensemble it is possible to estimate the temperature; however sometimes, having the temperature as a control variable is desired. In MD however, temperature is not a variable which can be preselected [155]. The modification to a molecular dynamics scheme with the intention of generating a thermodynamical ensemble at constant temperature, is called a thermostat algorithm [78]. The temperature in

45

molecular dynamics is related to the particles' momentum as follows:

$$\sum_{i=1}^{N} \frac{|p_i|^2}{2m_i} = K.$$

(2.93)

By the equipartition theorem, the average value for the internal kinetic energy K of a system is related to its macroscopic temperature T through [78]

$$K = <\mathrm{K}> = \frac{1}{2} k_B N_{df} T_{inst},$$

(2.94)

where T_{inst} is the instantaneous temperature, and K its instantaneous internal kinetic energy. N_{df} is calculated as:

$$N_{df} = 3N - N_c - N_r.$$

(2.95)

N is the number of atoms in the system, N_c the number of geometrical constraints and N_r the external degrees of freedom. When in the presence of stochastic and frictional forces, N_r is considered to be zero, when periodic boundary conditions are considered $N_r = 3$, and under vacuum conditions $N_r = 6$.

2.6.1.1 Velocity-Scaling Thermostat

Velocity scaling could be considered as the first port of call for the implementation of a thermostat algorithm. This is primarily due to its simplicity. Temperature is imposed on a system by considering the (translational) kinetic energy per particle [95], [77] in the following relationship:

$$k_B T = m < v_\alpha^2 >.$$

(2.96)

46
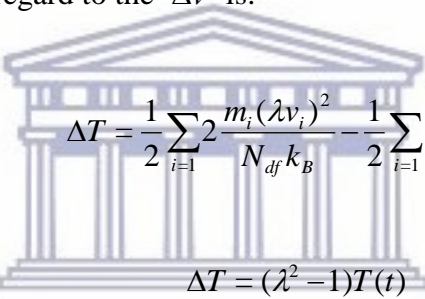
Here the mass of the particle is denoted by m and the α'th component of its velocity by v_α. Then with rearrangement the above becomes:

$$T_i = \frac{mv_i^2}{k_B},$$

(2.97)

and if we were to scale the velocity of v_{i+1} by a factor λ such that

$$v_{i+1} = \lambda v_i,$$

(2.98)

then the temperature with regard to the Δv is:

$$\Delta T = \frac{1}{2} \sum_{i=1} 2 \frac{m_i (\lambda v_i)^2}{N_{df} k_B} - \frac{1}{2} \sum_{i=1} 2 \frac{m_i v_i^2}{N_{df} k_B}$$

(2.99)

$$\Delta T = (\lambda^2 - 1) T(t)$$

(2.100)

$$\lambda = \sqrt{\frac{T_0}{T(t)}}.$$

(2.101)

Therefore the most straightforward way to control the temperature is done through scaling the velocity by a factor λ. The limit of this approach is that the temperature fluctuations, which are found in the canonical ensembles, are not factored in [95].

2.6.1.2 Andersen Thermostat

Another approach to implementing a thermostat was proposed by Andersen [25], where the system is connected to what is known as a heat bath. The purpose of the heat bath is to impose the required temperature. The manner by which this is done is through selecting a random particle and allowing it to encounter a stochastic impulsive force. The system

47

throughout collisions progresses at constant energy with respect to Newtonian laws of motion [37]. For a single particle that is randomly chosen its velocity is updated and drawn from the Maxwell-Boltzmann distribution. If successive collisions are not related then the probability, $\wp(v,t)$ that the next collision will occur in the time interval Δt follows a Poisson distribution [37]:

$$\wp(v,t) = v\exp(-vt). \tag{2.102}$$

Ultimately, the Andersen thermostat, despite its ability to rigorously generate the correct canonical ensemble probabilities, the presence of random collision causes the velocities of particles to de-correlate and results the true kinetics of the system not preserved [151].

2.6.1.3 Nose Thermostat

In the Andersen approach the desired temperature is realized through stochastic collisions with a heat bath. Nosé [67], [68], [80] showed that one could implement a thermostat through deterministic molecular dynamics and this could be achieved by introducing an extended system method.

The extended system is done through the incorporation of an artificial variable $\tilde{s}$, which has an associated "mass" $A > 0$, a velocity $\dot{\tilde{s}}$ and momentum $p_{\tilde{s}}$. $\tilde{s}$ is considered to be the "position" of the fictitious heat bath coupled to the system. The relation of the variables is given as:

$$p_{\tilde{s}} = A\dot{\tilde{s}}. \tag{2.103}$$

The strength of the correlation between these two variables is determined by the magnitude of A. The role of the artificial variable $\tilde{s}$ is to introduce a parameter that scales with respect to the time accordingly. In the extended system this is taken into account as

48

follows:

$$d\tilde{t} = \tilde{s}\,dt. \qquad (2.104)$$

The Hamiltonian now becomes [37]:

$$H = \frac{1}{2}\sum m_i \mid p_i \mid^2 + U(r^N) + \frac{p_{\tilde{s}}^2}{2A} + k_B T N_{df} \ln \tilde{s}, \qquad (2.105)$$

where the last two terms gives the kinetic and the potential energy for the heat bath. Another function of interest is the Lagrangian of the system. It in its general form has the following relationship with the total kinetic and potential energy of the system:
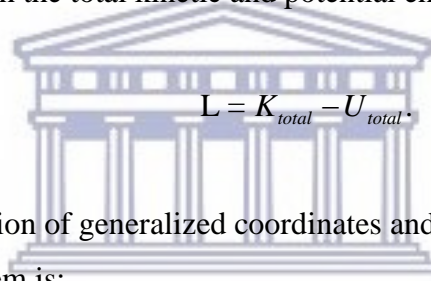
$$\mathrm{L} = K_{total} - U_{total}. \qquad (2.106)$$

The Lagrangian is a function of generalized coordinates and velocities. Its relationship with the Hamiltonian of a system is:

$$H(\mathbf{r}_i,\mathbf{p}_i,t) = \sum \dot{\mathbf{r}}_i \mathbf{p}_i - \mathrm{L}(\mathbf{r}_i,\dot{\mathbf{r}}_i,t). \qquad (2.107)$$

In terms of the extended system the Lagrangian is as follows [37]:

$$\mathrm{L} = \sum_i \frac{m_i}{2}\tilde{s}^2\dot{\tilde{r}}_i^2 - U(\tilde{r}) + \frac{1}{2}A\dot{\tilde{s}}^2 - k_B T_0 N_{df} \ln \tilde{s}. \qquad (2.108)$$

The advantage of the Nose thermostat is that because time evolution is deterministic, it meticulously produces canonical ensemble thermodynamics, approximating the actual dynamics of a system   [151]. The disadvantage is that the formulation is not convenient to implement and therefore improvements were made, known as the Nose-Hoover thermostat;

49

a further improvement is known as the Nose-Hoover chains. In the latter, numerous heat baths are incorporated thereby increasing the number of degrees of freedom, which is associated with improving temperature equilibration.

2.6.2 Barometers

As with thermostats, there are many ways in which the pressure can be adjusted and is formally known as barostat techniques. The manner in which this is done is by adjusting the simulation volume. The progression of adjusting the pressure follows much like that of temperature. Firstly one could just do a volume re-scaling, then weakly coupled it to a pressure bath, and then ultimately deduce an extended ensemble for the barostat.

2.7 DFT, MD and MC Applications in Materials Studio
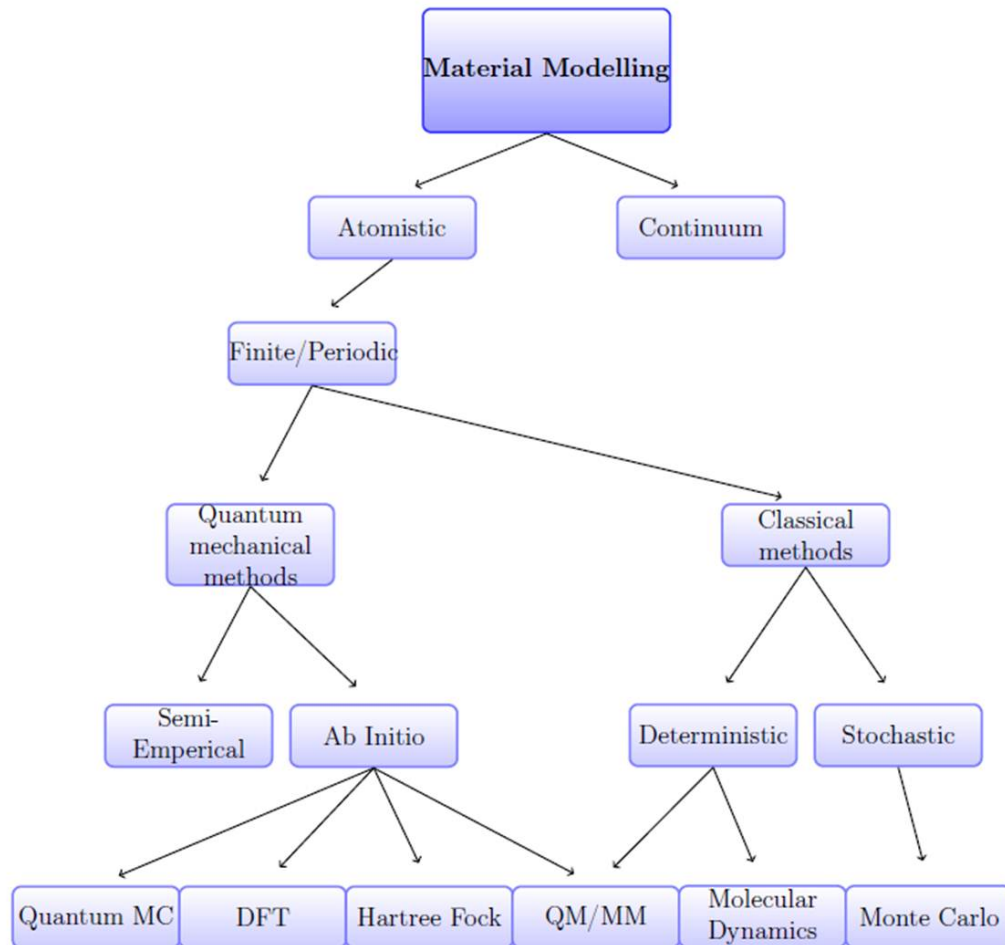
Figure 2.6: Computational tools and methods used to model materials

A summary of computational methods used to model materials is shown in figure 2.1. The methods used in this work is density functional theory, (DFT), monte carlo, (MC), and molecular dynamics, (MD).

Materials Studio, developed and distributed by Accelrys, is a software package for simulating and modelling materials [41]. In South Africa a national license is provided by the Centre for High Performance Computing, (CHPC). When the package is installed and opened, a materials visualizer, graphical interface, appears where projects can be created and three dimensional structures can be imported, edited and sketched. Charts and forcefields can also be viewed, created and edited. Materials Studio allows for the

execution of user created code to automate repetitive tasks, links several tasks or calculations, perform additional calculations and/ or integrate other software. The programming language supported is Perl. Material Studio allows for modelling of materials of varying orders of magnitude under one umbrella, and therefore for this purpose and the availability of the national license, it is used throughout this project.

2.7.1 CASTEP - Density Functional Theory Application

CASTEP is a software package which implements density functional theory [186]. The following concepts are the basis for the implementation of DFT, particularly in CASTEP.

2.7.1.1 Supercell approach

The supercell method utilized by CASTEP enforces periodicity, even though it is superficial. When periodic conditions are imposed, Bloch's theorem can be used. The advantage hereof is that each electronic wavefunction can be written as a product of a cell-periodic and wavelike components [124]:

$$\psi_{nk}(x) = \exp(ikx)u_{nk}(x). \tag{2.109}$$

The argument of the exponent ikx is the plane wave of wavenumber k and $u_{nk}(x)$ the cell periodic part. $u_{nk}(x) = u_{nk}(x+L)$ and L is the length of the unit cell [187]. Alternatively this can be written as:

$$\psi_{nk}(r+R) = \exp ikx \psi_{nk}(r). \tag{2.110}$$

52
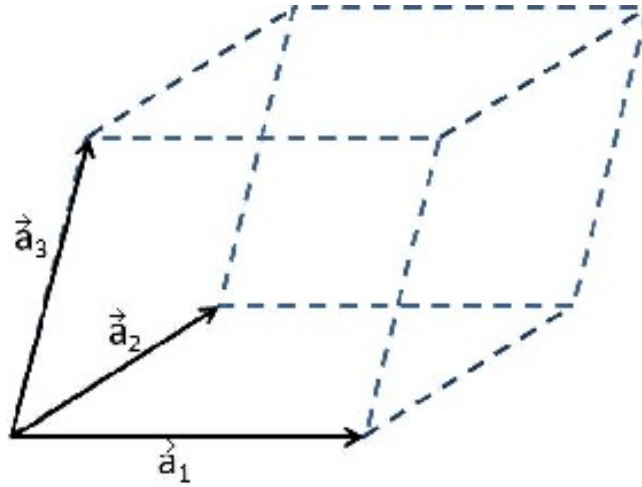
Figure 2.7: Unit Cell

If we were to consider a computational cell as in figure 2.2, where for a cell matrix, $\mathbf{h} = [\vec{a}_1, \vec{a}_2, \vec{a}_3]$ and the volume, V_{cell}, is calculated by:
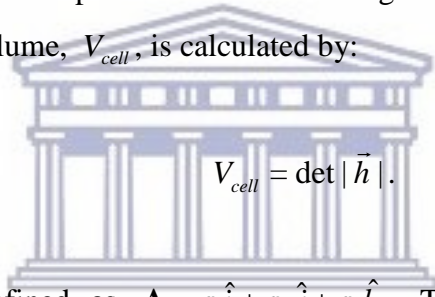
$$V_{cell} = \det |\vec{h}|. \tag{2.111}$$

The lattice vector is defined as $\mathbf{A} = a_1\hat{i} + a_2\hat{j} + a_3\hat{k}$. The reciprocal lattice, G, in components is as follows:

$$\vec{b}_1 = 2\pi \frac{\vec{a}_2 \times \vec{a}_3}{\Omega}; \vec{b}_2 = 2\pi \frac{\vec{a}_3 \times \vec{a}_1}{\Omega}; \vec{b}_3 = 2\pi \frac{\vec{a}_1 \times \vec{a}_2}{\Omega}, \tag{2.112}$$

where $\mathbf{G} = b_1\hat{i} + b_2\hat{j} + b_3\hat{k}$.

In equation 2.110, ψ can now be rewritten, incorporating basis sets such that it consists of a discrete set of plane waves whose wave vectors are reciprocal lattice vectors of the crystal [94]:

$$\psi_i(r) = \sum C_{i,\mathbf{G}} \exp(i\mathbf{G} \cdot \mathbf{R}). \tag{2.113}$$

53

Each electronic function can therefore be written as a sum of plane waves. To calculate the independent-particle electronic states in materials three basic approaches can be used, known as **plane waves**, **localized atomic orbitals** and **Augmented methods** [107]. Plane wave functions are ideal for the periodic systems of crystals and are simple to implement. The simplicity of this method lies in the utilization of fast Fourier transforms, FFT. The latter two methods are not used in this work and further explanations on each can be found in books by Martin [107] and Ferrario et al [93].

Implementation of the plane waves basis set

In CASTEP a pseudopotential approximation is used to calculate the plane wave basis set. The primary reason for this is that the number of plane waves required for a calculation would be very large, $> 10^6$. In pseudopotential approximations the nucleus and core electrons is replaced by a fixed effective potential and only valence electrons are considered in the calculation. The prerequisite however, is that the scattering properties be conserved exactly. A cutoff for the plane waves must be implemented because in theory an endless number of plane waves are required. However, practically, the number of plane waves is determined a cutoff kinetic energy, E_{cut}. E_{cut} limits the number of reciprocal lattice vectors that meet the following criterion:

$$|k + G|^2 \leq E_{cut}. \tag{2.114}$$

This leads to a simplified Kohn-Sham equation [41], described earlier in equation (2.32):

$$\sum [|k + G|^2 \delta_{GG'} + V_{ion}(G - G') + V_H(G - G') + V_{xC}(G - G')]C_{i,k+G'} = \varepsilon_i C_{i,k+G} \tag{2.115}$$

where the various potentials, *V*, due to electron-ion, Hartree and exchange-correlation are described in terms of their Fourier transformations.

Usage of Fast Fourier Transform (FFT) in Plane Wave Calculation

Using FFT the calculation of the product of the Hamiltonian with a wavefunction is

54

simplified since the kinetic energy operator of the Hamiltonian, the Hartree operator and the local pseudopotential operator, has a diagonal representation in reciprocal space. The exchange-correlation potential, E_{XC}, has a diagonal representation in real space.

Exchange-correlation functional

There are many exchange-correlation functionals available in CASTEP. These functionals fall in the following categories; Local Density Approximation (LDA), gradient-corrected Generalised Gradient Approximations (GGA) and fully nonlocal (based on the exact and screened exchange formalism). The functional by Perdew and Zunger [123] is the only LDA provided in CASTEP. This functional uses parameterizations of numerical results found by Ceperley and Alder [122]. GGA functionals, also known as non-local functionals, depend on $d\rho/dr$ as well as ρ. This provides a considerable increase in the accuracy of predicted energies and structures, but with an additional computational cost. The nonlocal functionals available in CASTEP include: Perdew-Wang generalized gradient approximation [121], [127], Perdew-Burke-Ernzerhof (PBE) functional [120] and revised Perdew-Burke-Ernzerhof [119]. The GGA functional determined by Wu and Cohen [195] shows improvements on accuracy. Perdew et al [194] provide a version of the Perdew-Wang generalized gradient approximation functional, which gives better equilibrium properties of densely packed solids and their surfaces.

2.7.1.2 Simulation Setup

After a suitable cell is created in the materials visualizer, in CASTEP the setup tab allows the user to choose the type and quality of a calculation. The types of calculations that can be executed are, single point energy calculations, geometry optimization, molecular dynamics, the calculation of elastic constants, a transition state search and further refinement of the reaction path based on the transition state search.

2.7.1.3 Geometry Optimization

After an initial structure of a material has been created, the geometry would have to be optimized. Within the CASTEP module a task called Geometry Optimization allows for the refinement of a structure until a specified convergence criteria is met. The process is iterative where atomic coordinates and/ or cell parameters are amended, until the total energy of the structure is minimized. CASTEP utilizes two algorithms to perform geometry optimization. These are BFGS created by Pfrommer et al [92] and damped molecular dynamics. Further properties can then be calculated, which is discussed in the Analysis section.

2.7.1.4 Analysis

The following analysis techniques are available in CASTEP; band structure, core level spectroscopy, density of states, elastic constants, electron density, electron density difference, electron localization function, energy evolution, Fermi surface, infrared (IR) spectrum, nuclear magnetic resonance (NMR), optical properties, orbitals, phonon dispersion, phonon density of states, population analysis, potentials, Raman spectrum, scanning transmission microscope (STM) profile, structure and thermodynamic properties.

2.7.2   FORCITE - Molecular Dynamics Application

2.7.2.1 Cell Creation - Amorphous Cell

Once a suitable specimen of the material of interest is either imported or created, a periodic cell on which simulations will be calculated, is created within Material Studio using the Amorphous Cell. The Amorphous Cell module provides a comprehensive set of tools to create three-dimensional periodic structures of molecular liquids and polymeric systems. It uses Monte Carlo methods to minimize close contacts between atoms, and ascertaining realistic spread of torsion angles for a specified forcefield [41].

56

2.7.2.2 Geometry Optimization

The geometry optimization algorithms available in FORCITE are; Steepest descent, Conjugate gradient, Quasi-Newton, Adjusted basis set Newton-Raphson and Smart. For the most part of the molecular dynamics simulations done in this work the Smart algorithm is used, which is a combination of Steepest descent, Newton-Raphson and Quasi-Newton methods [118], [41].

2.7.2.3 Annealing

By annealing the geometry optimized structure it is periodically subjected to fluctuations in temperatures, so that conformational space can be explored for low energy structures. This also prevents a structure from being trapped in a conformation that is a local energy minimum, and not global [41].

2.7.2.4 Dynamics

In the dynamics task of FORCITE, the time evolution of a material under thermodynamic constraints can be implemented. In the selected ensemble a preferred thermostat, barostat and time step can be chosen. An integration constraint is held such that, when a simulation becomes unphysical the simulation would terminate. Equilibrium is considered to have been reached when the energy and/ or temperature fluctuates around a constant average.

2.7.2.5 Energy

The energy tab in FORCITE is where the forcefield U, first mentioned in equation 2.37, can be chosen. For the energy calculation, the accuracy for non-bond evaluations can be set, and methods for calculating charges and non-bond interactions can be chosen. FORCITE provides the six options for forcefields; COMPASS, COMPASSII, Dreiding,

57

Universal, cvff and pcff. The forcefield used in this work is COMPASS (Condensed-phased Optimized Molecular Potentials for Atomistic Simulation Studies), where the forcefield is given to be [24]:

$$U = U_b + U_\theta + U_\phi + U_\chi + U_{bb'} + U_{b\theta} + U_{b\phi} + U_{\theta\theta'} + U_{\theta\theta'\phi} + U_{elec} + U_{LJ}. \tag{2.116}$$

The terms, $U_{bb'} + U_{b\theta} + U_{b\phi} + U_{\theta\theta'} + U_{\theta\theta'\phi}$ are additional to that specified in equation 2.37 and are termed as cross-coupling terms between internal coordinates. These terms are important for the calculation of the vibrational frequencies and structural variations as a result of conformational changes. COMPASS was the first ab initio forcefield that enabled accurate and simultaneous prediction of gas-phase properties and condensed-phase properties for a wide range of molecules and polymers [41]. What makes COMPASS an ab initio forcefield is that its parameters were derived based on ab initio data.

2.7.2.6 Mechanical Properties – Optional

The general formulation for a physical characteristic or property T that serves to link two vectors $\vec{R} = [r_1 r_2 r_3]$ and $\vec{D} = [d_1 d_2 d_3]$ is given by:

$$\begin{pmatrix} r_1 = T_{11}d_1 + T_{12}d_2 + T_{13}d_3 \\ r_2 = T_{21}d_1 + T_{22}d_2 + T_{23}d_3 \\ r_3 = T_{31}d_1 + T_{32}d_2 + T_{33}d_3 \end{pmatrix}. \tag{2.117}$$

For convenience this can be rewritten as:

$$r_i = \sum_{j=1}^{3} T_{ij}d_j, \tag{2.118}$$

58
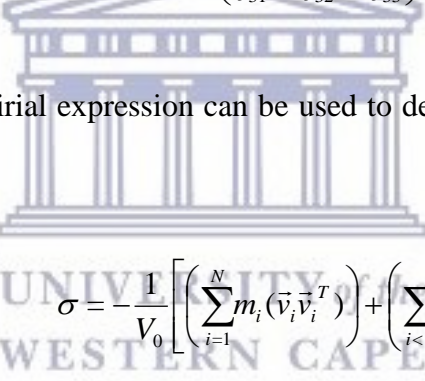
where $i = 1,2,3$. The constants T_{ij} determine how the three components r_i varies when different values are given to the components d_j. This mathematical relationship is similar to when a body is acted on by external forces, stress and the strain experienced as a result thereof. Stress, σ and strain, ξ are second order rank tensors with components such that:

$$\sigma = \begin{pmatrix} \sigma_{11} & \sigma_{12} & \sigma_{13} \\ \sigma_{21} & \sigma_{22} & \sigma_{23} \\ \sigma_{31} & \sigma_{32} & \sigma_{33} \end{pmatrix}, \tag{2.119}$$

and

$$\xi = \begin{pmatrix} \xi_{11} & \xi_{12} & \xi_{13} \\ \xi_{21} & \xi_{22} & \xi_{23} \\ \xi_{31} & \xi_{32} & \xi_{33} \end{pmatrix}. \tag{2.120}$$

At the atomic level, the Virial expression can be used to determine σ. This expression is given by [41]:

$$\sigma = -\frac{1}{V_0}\left[\left(\sum_{i=1}^{N} m_i (\vec{v}_i \vec{v}_i^{\,T})\right) + \left(\sum_{i<j} \vec{r}_{ij} \vec{F}_{ij}^{\,T}\right)\right]. \tag{2.121}$$

i is the running index over all particles. The mass, velocity, displacement and force vectors acting on particle i is denoted by m_i, $\vec{v}_i$, $\vec{r}_{ij}$ and $\vec{F}_i$. V_0 is the original system volume.

At the molecular level when a body experiences an applied stress the particles within it are displaced by a distance $\Delta \vec{r}$ and the resultant cell accordingly. A periodic cell can be represented by a three column vector at time instant zero as $\vec{h}_0 = [\vec{a}_0,\ \vec{b}_0,\ \vec{c}_0]$ and after a strain has been placed by $\vec{h} = [\vec{a},\ \vec{b},\ \vec{c}]$. The strain tensor with respect to these two column vectors is given by [41]:
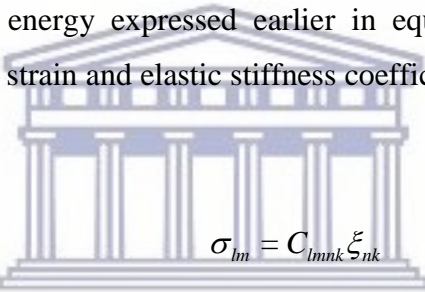
$$\xi = \frac{1}{2}\left[\left(\vec{h}_0^T\right)^{-1}\vec{G}\vec{h}_0^{-1}\right].\tag{2.122}$$

G is the metric tensor such that $G = h^T h$, and T denotes the transpose.

The elastic stiffness coefficients, C_{lmnk}, relating the various components of stress and strain is:

$$C_{lmnk} = \frac{\partial \sigma_{lm}}{\partial \xi_{nk}}\Big|_{T\xi_{nk}} = \frac{1}{V_0}\frac{\partial^2 F}{\partial \varepsilon_{lm}\partial \varepsilon_{nk}}\Big|_{T\varepsilon_{lm}\varepsilon_{nk}}.\tag{2.123}$$

F is the Helmholtz free energy expressed earlier in equation 2.84. The generalized Hooke's law relates stress, strain and elastic stiffness coefficients for small deformations as follows [99], [100]:

$$\sigma_{lm} = C_{lmnk}\xi_{nk}\tag{2.124}$$

and

$$\xi_{ml} = S_{lmnk}\sigma_{nk},\tag{2.125}$$

where S_{lmnk} denotes the compliance components. The symmetry of the stress and strain tensors allows us to use Voigt vector notation. For the Stress tensor it follows [98], [41] that:

$$\begin{pmatrix} \sigma_{11} & \sigma_{12} & \sigma_{13} \\ \sigma_{21} & \sigma_{22} & \sigma_{23} \\ \sigma_{31} & \sigma_{32} & \sigma_{33} \end{pmatrix} \rightarrow \begin{pmatrix} \sigma_1 & \sigma_2 & \sigma_3 \\ \sigma_4 & \sigma_5 & \sigma_6 \\ \sigma_7 & \sigma_8 & \sigma_9 \end{pmatrix}\tag{2.126}$$

60

and

$$\sigma = \left[\sigma_{11}\sigma_{22}\sigma_{33}\sigma_{23}\sigma_{13}\sigma_{12}\right]^{T}. \tag{2.127}$$

The Strain tensor can then also be rewritten as:

$$\begin{pmatrix} \xi_{11} & \xi_{12} & \xi_{13} \\ \xi_{21} & \xi_{22} & \xi_{23} \\ \xi_{31} & \xi_{32} & \xi_{33} \end{pmatrix} \rightarrow \begin{pmatrix} \xi_1 & \xi_6/2 & \xi_5/2 \\ \xi_6/2 & \xi_2 & \xi_4/2 \\ \xi_5/2 & \xi_4/2 & \xi_3 \end{pmatrix}, \tag{2.128}$$

where

$$\xi = \left[\xi_{11}\xi_{22}\xi_{33}2\xi_{23}2\xi_{13}2\xi_{12}\right]^{T}. \tag{2.129}$$

An in depth discussion and derivation on how the partition function and thermodynamic properties are affected can be found in the book by Frenkel and Smit, called "Understanding Molecular Dynamics" [37]. The section called linear response theory discusses how constants are measured in a computer simulation for crystals under isotropic (hydrostatic) pressure.

2.7.2.7 Analysis

There are three categories under which analysis occurs in FORCITE, these are then further subdivided according to the table below:

61

	Rotational time correlation function, Space time correlation function
	Stress autocorrelation function, Temperature profile
Dynamic	Velocity autocorrelation functions, Velocity profile
	Dipole autocorrelation function, Fluctuation properties
	Mean square displacement
	Cell parameters, Density
	Hamiltonian, Potential energy components
Statistics	Pressure, Temperature
	Total kinetic energy
	Angle distribution, Angle evolution
	Concentration profile, Density field
	Length distribution, Radial distribution function
Structural	Radius of gyration, Radius of gyration evolution
	Scattering, Spatial orientation correlation function
	Torsion distribution, Torsion evolution

Table 2.3: FORCITE categories of analysis

2.7.3   Adsorption Locator - Monte Carlo Application

Adsorption Locator is a simulation package that utilizes Monte Carlo searches of a samples' configurational space to identify possible adsorption configurations [37] [116], [117]. The Metropolis Monte Carlo method [115] provides four means, that are selected at random, of arriving at a canonical ensemble. These are known as conformer, rotation, translation and regrowth step types [41]. For the conformer step type to be executed, a

62

trajectory of conformations of the sorbate should be provided. When this step type is used the sorbate it is replaced with a randomly chosen conformation from the trajectory for that species. When executed, the rotation step type is where the adsorbate is rotated about its center of geometry by an angle $\delta\theta$ about an axis, $\vec{B}$. The axis $\vec{B}$ is drawn from a random point on a sphere to its origin. $\delta\theta$ is drawn from a uniform distribution between $-\Delta\alpha$ and $\Delta\alpha$. $\Delta\alpha$ is the maximum rotation amplitude. The chosen step type is implemented to a random sorbate of a random component. The procedure followed is such that when the translation step type is executed the sorbate is translated by a distance of Δr along an axis $\vec{B}$. $\vec{B}$ is once again drawn from a random point on a sphere to its origin. The translational distance Δr is drawn from a uniform distribution between 0 to Δ_t, where Δ_t is the maximum translation amplitude. This is specified at the start of the Sorption run.

When the regrowth step type is chosen, a new sorbate from the same species replaces the initial selected sorbate and is inserted at a random position in the framework. At the new position the sorbate has a random orientation and, if a trajectory of conformations was supplied, with a random conformation.

As with the MC procedure mentioned in section 2.3, the probablity of acceptance takes on a similar form. The probability of a configuration in the grand canonical ensemble, leads to an acceptance probability of:

$$\wp_{r \to t} = \min(1, \frac{F(\{N\}_t)}{F(\{N\}_r)} \exp - \beta(E_r - E_t)).$$ (2.130)

2.8 Implementation

The computational methods implemented in this work utilized molecular dynamics and

63

Monte Carlo methods for chapters 3 – 5 and the results have been, where possible, compared to experimental findings. The work done in chapter 6 implemented density functional theory and Monte Carlo methods. All of these investigations have been able to give very valuable insight about processes that occur at the nanoscale within high temperature proton exchange membrane fuel cells.

64

Chapter 3: The study of Increased Temperature on Phosphoric Acid using three different Thermostat Algorithms

Abstract

Molecular dynamics was used to study the doping agent, phosphoric acid, of a high temperature fuel cell membrane. Previous studies using molecular dynamics have utilised either Andersen or velocity scaling thermostats. Andersen or velocity scaling thermostats are considered to be the two least accurate of the thermostat algorithms and therefore the objective of this section is to, through the application of a more accurate thermostat, quantify and compare the solubility, activation energy and transportation properties of phosphoric acid. Increasing the accuracy of the model directly influences the computational time. A comparison of the computational time taken to perform the calculations was done and on the basis thereof informed decisions for further calculations were made.

3.1   Introduction

The exorbitant increase in global electricity demands, consequently prices, and the limitations in fossil fuel resources and climate change propel research and development in alternative energy resources. Some of the areas of research cover solar energy, wind power, geothermal energy, hydro power and fuel cells. Of these, fuels cells is considered throughout this work, which is subdivided into two categories according to their temperature of operation. High temperature fuel cells operate at temperatures greater than $100°C$ [200]. For High Temperature Polymer Electrolyte Membrane Fuel Cells

(HTPEMFC) operation one of the most extensively investigated polymer membranes is Polybenzimidazole (PBI). From the PBI family, a very good contender, Poly($2,5$–polybenzimidazole) (ABPBI) came to light. ABPBI differs from PBI in that it does not have the connecting phenyl rings [190]. The motivation for this preference is because it can be polymerized from a single monomer and is less expensive, it is commercially available and non-carcinogenic [72]. ABPBI, because it has a higher concentration of basic sites, has also been found to have a higher affinity towards acids, allowing for greater adsorption of the doping agents [192].

For either of these polymers to reach suitable levels of conductivity for HTPEMFC operation, the most preferred substance for doping is phosphoric acid (PA). In fuel cell operation, phosphoric acid is of particular interest because of its amphoteric characteristic [73]. This ability for PA to be a proton donor or acceptor assists proton transfer along the hydrogen bonded network [73, 74]. The other characteristic of PA beneficial to HTPEMFC operation is its ability to conduct protons even in its anhydrous form [74]. The acid also has an excellent thermal stability and low vapour pressure at high temperatures [17, 72].

In light of investigating the proton conductivity of PA-doped ABPBI membrane for high temperature fuel cell operation this section therefore considers the doping agent PA, in isolation. Studies of PA are extensive, some of which were done by Spieser et al [75], Dippel et al [191] and Tromp [79]. Molecular dynamics (MD) studies on PA have been done by Li et al [39] and More et al [76]. In these studies Andersen and velocity scaling thermostat algorithms were used respectively. For thermostat algorithms three main pillars can be considered i.e. velocity scaling[77, 78], Anderson [25] and Nosé [80, 68, 67]. If the thermostats are implemented correctly, the accuracy increases in the order of listing [37], [82]. The objective is to determine the effect of temperature on the solubility, self-diffusion and activation energy of PA by means of MD and the Nosé thermostat algorithm. These results will aid in establishing whether the sacrifice of computational time for accuracy is worthwhile in the rest of the investigations to follow.

66

3.2   Method

The manner in which a system evolves to the desired temperature in MD has been an area that over the years has seen many improvements. As mentioned, the three main fundamental thermostat algorithms are velocity scaling, Anderson and Nosé. In velocity scaling the temperature of a system is achieved through scaling of the velocity of each atom at each time step, by a factor to create the desired temperature [37]. With an Andersen thermostat, constant temperature is obtained through stochastic collisions of particles with a heat bath [37]. Nosé however, showed that with the introduction of an extended Lagrangian, deterministic MD could be performed [37]. Many extensions of these methods have since then been accepted, one of which is the Nosé-Hoover thermostat [81].

A sample consisting of 125 PA molecules was created using a program called Amorphous Cell, in the Materials Studio suite, provided by Accelrys [41]. An initial density of $1.8\,g/cm^3$ was implemented, followed by a process of annealing, energy minimization and $50\,ps$ equilibration simulation where the number of particles, pressure and temperature were kept constant (NPT ensemble). This was done using an Andersen thermostat. To compare values determined using different thermostat algorithms, the temperature set considered was $298K$, $333K$, $393K$, $423K$ and $453K$. For each temperature velocity scaling, Anderson and Nosé thermostats were implemented. To determine the solubility parameter a NPT ensemble simulation dynamics was implemented for $300\,ps$. An ensemble where the number of particles, volume and temperature (NVT), was considered to determine the self-diffusion coefficient and derive the activation energy of PA. Simulation dynamics duration was $1ns$ with a time step of $1fs$. A standard Ewald summation was used for both Van De Waals and Coulomb interactions. The properties of PA were determined using a forcefield called COMPASS [24]. COMPASS is an acronym for Condensed-phase Optimized Molecular Potentials for Atomistic Simulation Studies and is available on the commercial material modelling platform known as Materials Studio,

67
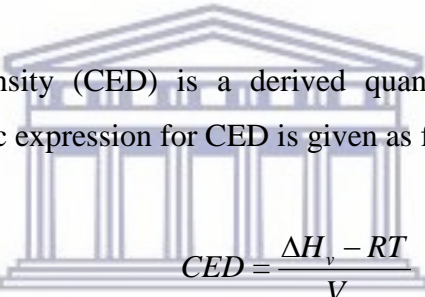
provided by Accelrys.

For a sample, pressure is determined using the Virial theorem [83]. The Virial theorem shows the relationship between pressure and temperature as follows:

$$PV = Nk_BT + \frac{1}{2}\sum_{i=1}^{N}\Delta\vec{r}_i \cdot \vec{f}_i$$

(3.1)

where k_B is the Boltzmann constant, $\Delta\vec{r}_i$ the displacement vector and $\vec{f}_i$ the force on atom i due to all other atoms . The pressure represents external forces imposed by the walls of the container [83].

The cohesive energy density (CED) is a derived quantity related to the energy of vaporization. The algebraic expression for CED is given as follows:

$$CED = \frac{\Delta H_v - RT}{V_m}$$

(3.2)

where ΔH_v is the heat of vaporization, R the gas constant, T the temperature and V_m the molar volume. CED is also a direct indicator of the strength of the Van de Waals forces holding the molecules of a liquid together [84]. In liquid or gas phases it is deemed to be the energy required to remove a molecule from its nearest neighbours [85]. This would infer that the greater the van de Waals forces, the greater the difficulty in removing a molecule from its position, and the amount of heat required to separate the molecules.

The ease with which two materials are able to mix is dependent on how close the strength of the intermolecular forces is to each other. The solubility parameter δ, found by taking the square root of the CED, is merely a numerical value indicating whether a substance is soluble in another. PA has an experimental solubility parameter of $35.7(J/cm^3)^{1/2}$ [53].

68

For this study, the solubility parameter of PA was determined over the before-mentioned temperature set.

The self-diffusion coefficient, D, for phosphoric acid, was determined through the application of an Einstein equation to the $1ns$ NVT dynamics. The Einstein equation referred to here is as follows:

$$D = \lim_{t \to \infty} \frac{1}{6t} <| r(t) - r(0) |^2>$$

(3.3)

where $<| r(t) - r(0) |^2>$ is the mean square displacement, (MSD), and the term between the angular brackets indicates the ensemble average. $r(t) - r(0)$ is the vector distance travelled by particles over the time interval of length t. The square magnitude of this vector is averaged over many time intervals. D is calculated as one sixth of the slope from the plot of the MSD versus time [41].

From the self-diffusion coefficient one can determine the activation energy, E_a, using the Arrhenius equation [86]:

$$D = D_0 \exp(-\frac{E_a}{RT}).$$

(3.4)

PA when used as a doping agent in the membrane electrode assembly (MEA), forms part of the hydrogen bonded network with the polymer membrane. E_a introduced by Svante Arrehenius [86], describes this value as the minimum energy required by a chemical system that would result in a chemical reaction. Where the results were compared to published simulated and/ or experimental work.

3.3   Results and Discussion

The resultant simulated cells PA is displayed in figure 3.1, where the red atoms are representative of oxygen, purple phosphorous and white the hydrogen atoms in the schematic representation.
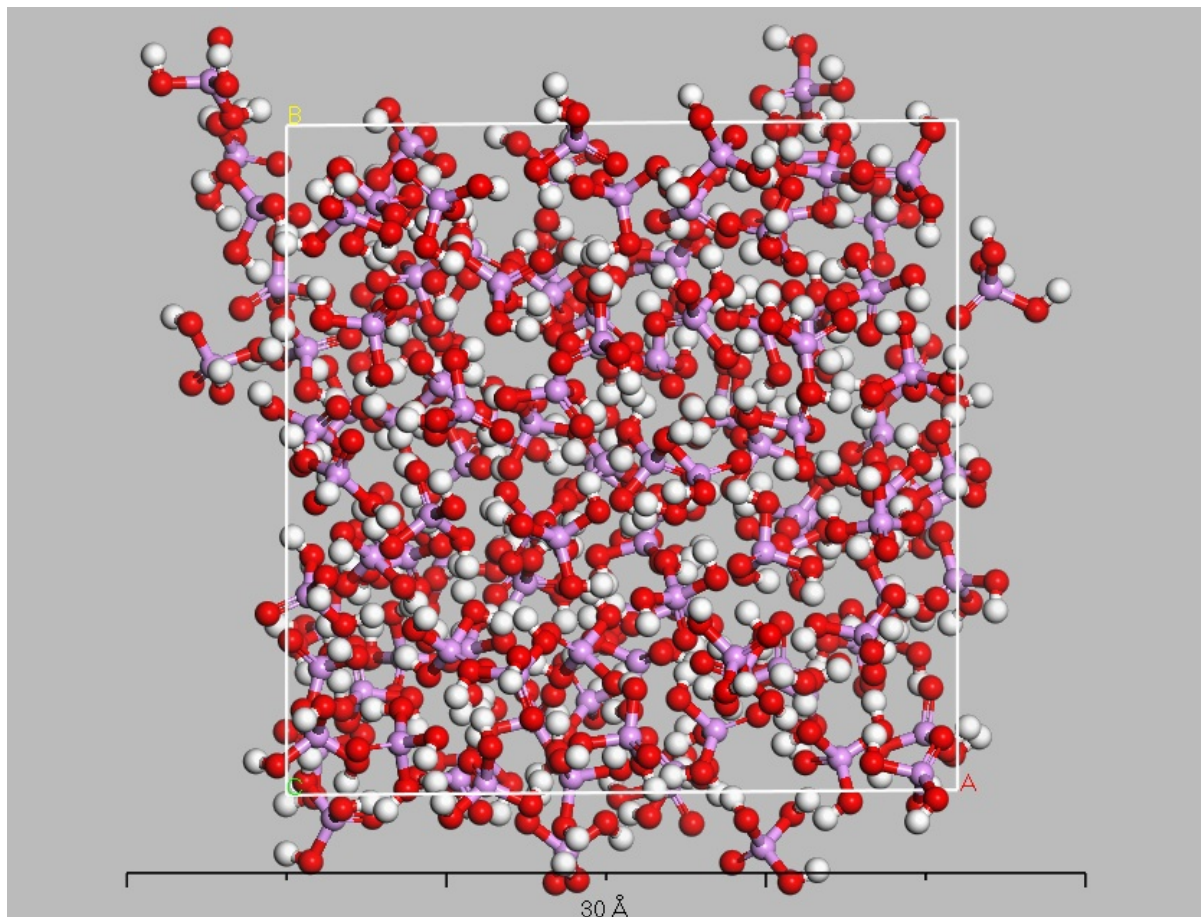
Figure 3.1: Illustration of simulated cell of Phosphoric Acid

3.3.1 Density

The density of PA was determined and results compared to experimentally determined reported values. As displayed in table 3.1, at $298K$ the Nosé thermostat shows good agreement to the experimental values. For all thermostats the trend observed is that an increase in temperature causes a reduction in the density. The discrepancy between the simulated and experimental results has been previously found. This variation, has been

70

said, can be reduced through the use of an equation of higher order or higher precision [189].

Thermostat	298K		333K		393K		423K		453K	
	ρ	σ_ρ	ρ	σ_ρ	ρ	σ_ρ	ρ	σ_ρ	ρ	σ_ρ
Velocity Scaling	2.161	0.022	2.124	0.020	2.039	0.022	1.922	0.026	1.911	0.039
Anderson	2.180	0.017	2.156	0.017	2.066	0.020	2.025	0.025	1.958	0.031
Nosé	2.053	0.026	2.136	0.019	2.028	0.021	2.010	0.025	1.942	0.035
MacDonald et al [90]	1.8818	0.0002	-	-	-	-	1.7752	0.002	-	-
Egan et al [91]	1.8818	0.0002	-	-	-	-	1.7752	0.002	-	-

Table 3.1: Phosphoric acid density as a function of temperature using Velocity Scaling, Andersen and Nosé thermostats

3.3.2   Solubility parameter

In figure 3.2, the solubility of PA is plotted as a function of temperature. The general trend is that the solubility parameter decreases with an increase in temperature. The cohesive energy density of a liquid is a numerical value indicating the energy of vaporization, and is a direct reflection of the strength of the van de Waals forces and hydrogen bonds holding the molecules of the liquid together. The implication of the results is that with increase in temperature the strength of the Van de Waals forces decreases [84]. This would make mixing with other materials easier. To determine whether materials mix, their solubility parameters are compared. When values are very similar, mixing is most likely to occur. In the chapters to follow the the solubility parameter of ABPBI is determined and quantifying the solubility parameters of these two materials assists in determine the the type of interaction that exists between these two materials.

71
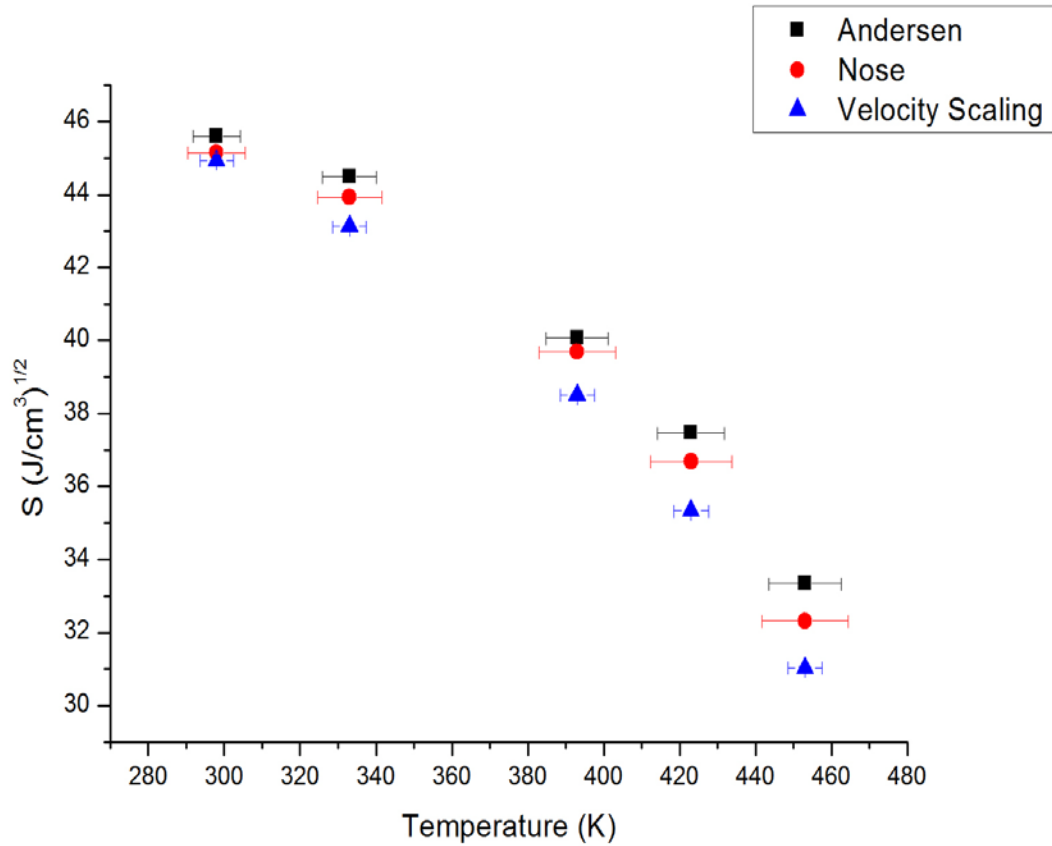
Figure 3.2: Solubility parameter of Phosphorous evaluated over 298K-453K temperature range

3.3.3 Self-diffusion Coefficient and Activation Energy

The average ensemble Self-diffusion coefficient was calculated using multiple time origins which is recommended to improve the statistics [87]. At room temperature Spieser et al [75] found the self-diffusion coefficient to be $2.3 \times 10^{-7} cm^2/s$. At $298K$, for the Nosê thermostat the value for the self-diffusion coefficient was found to be approximately $4.0 \times 10^{-7} cm^2/s$. This is in good agreement with the experimental results determined by Spieser et als. The relationship that D has with temperature is shown in figure 3.3. Here it becomes evident that as temperature increases the self-diffusion of PA increases. This implies that the vector distance travelled by particles increases with increasing

72

temperature.

The activation energy determined experimentally by Aihara et al [88] for $95wt\%$ sample results found was $29.8 \pm 0.2 kJ/mol$. In more recently simulated, published work by More et al [76], an activation energy of $44 kJ/mol$ was found and they attribute the difference between their and Li et al [13] result due to the different force fields used. As mentioned earlier, More et al used a velocity re-scaling thermostat, which is the least preferred method for isothermal investigations as one does not arrive at the true constant temperature of the ensemble [37]. Li et al [39], using an Andersen thermostat, arrives at a value of $23.8 kJ/mol$; it is however difficult to compare either results without an indication of their uncertainty.

At $298K$ the values for the Self-diffusion coefficients are similar. As temperature increase the difference in the values obtained by the different thermostats become more apparent. The value for the activation energies of Velocity scaling, Anderson and Nosé thermostats was determined from the linearization of the equation 3.4, where the activation is the slope of the curve. For the Anderson thermostat the activation energy was found to be $24527.1 \pm 3.0 J/mol$, for the Nosé thermostat $23286.2 \pm 2.2 J/mol$ and $22009.0 \pm 1.7 J/mol$ for the velocity scaling thermostat. The activation energy is a quantitative measure of the energy required by reacting species to undergo a reaction and therefore the lower its value the more likely a reaction would occur. If mixing does not occur then the interaction between materials is most likely through a chemical reaction.
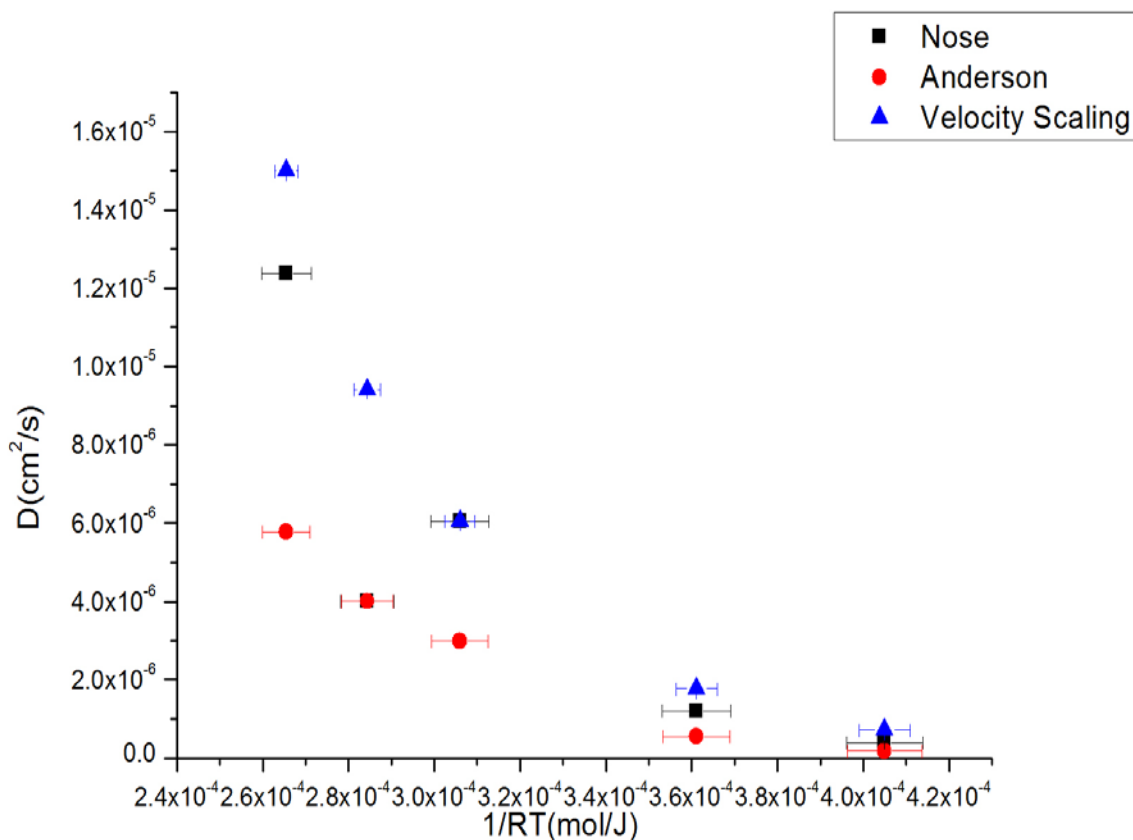
Figure 3.3: Self-diffusion Coefficient (D) of Phosphorous evaluated over 298K-453K temperature range

3.3.4 Thermostat time comparison

In table 3.2 the time taken for each of the simulations is provided. Each of the $300\,ps$ simulations were run over 16 processors in parallel and 32 for each of the $1ns$ runs. When comparing the time taken for each of the thermostats it becomes apparent that the differences are of the order of minutes. This allows us to comfortably utilize the Nosé thermostat, of higher accuracy, in the investigations to follow.

Temperature	Thermostat	300 *ps* NPT ensemble time	1*ns* NVT ensemble time
298*K*	Velocity Scaling	46:02 minutes	1:39:54 hours
	Anderson	46:19 minutes	1:39:41 hours
	Nosé	46:04 minutes	1:40:51 hours
333*K*	Velocity Scaling	45:49 minutes	1:40:35 hours
	Anderson	45:53 minutes	1:40:14 hours
	Nosé	45:48 minutes	1:42:38 hours
393*K*	Velocity Scaling	45:25 minutes	1:40:17 hours
	Anderson	45:29 minutes	1:39:41 hours
	Nosé	45:39 minutes	1:41:48 hours
423*K*	Velocity Scaling	44:59 minutes	1:40:34 hours
	Anderson	45:23 minutes	1:39:40 hours
	Nosé	45:28 minutes	1:41:59 hours
453*K*	Velocity Scaling	46:47 minutes	1:40:53 hours
	Anderson	45:00 minutes	1:39:55 hours
	Nosé	44:55 minutes	1:46:16 hours

Table 3.2: A comparison in the computational time required using Velocity Scaling, Andersen and Nosé thermostats in studying phosphoric acid.

3.4   Conclusion

Three thermostats algorithms were used to investigate the solubility, self-diffusion and activation energy of phosphoric acid. The significance of studying these properties is that with further studies of the other materials found in the MEA, the type of interaction can be established. These properties have previously been investigated using velocity scaling and the Andersen thermostat algorithm, and the intention of this work is to compare these results to that found by a more accurate thermostat. In the results for all three properties, the Nosé thermostat algorithm gave results between the Andersen and velocity scaling. A deduction from this is that through deterministic MD, results for the solubility,

75

self-diffusion and activation energy of phosphoric acid can be found to fall between those from temperature scaling and the stochastic collision of particles with a heat bath algorithms for temperature. A comparison in the computational time required was done and as result the investigations to follow will implement thermostats of higher order.

UNIVERSITY *of the*

WESTERN CAPE

Chapter 4: The Influence of Increased Temperature on the Miscibility and Mechanical Properties of poly(2,5-benzimidazole) and polytetrafluoroethylene

Abstract

Molecular dynamics was used to study the effects of temperature on the miscibility and mechanical properties of two polymers used in the membrane electrode assembly (MEA) of a high temperature polymer electrolyte fuel cell. The polymers, poly(2.5-benzimidazole) (ABPBI) and polytetrafluoroethylene (PTFE), are respectively found as constituents of the membrane and ionomeric layers of the membrane electrode assembly. The temperatures considered are $298K$ and $383K$ for the mechanical properties calculations and a range of $[298K - 383K]$ to study the temperature dependence of the solubility parameter. Of the two polymers, PTFE has the lower solubility parameter, which we have found to decrease by 6% as temperature increases. The ABPBI solubility parameter decreases by less than 1% as temperature increases. The greater difference between these two values indicates that at an elevated temperature of $383K$ these two polymers are even more unlikely to mix. For the mechanical properties calculation, the molecular dynamics approach used implements a constant strain algorithm. The significance of this work is that it gives insight into the mechanical robustness for materials found within the MEA and confirms that miscibility is unlikely to occur as temperature increases.

4.1 Introduction

Two key characteristics contributing to a fuel cell membranes' high power density, is high proton conductivity and for the polymer found in the membrane electrode assembly (MEA) to act as an excellent gas diffusion barrier for gases supplied on the anode and cathode sides [44, 31]. For the membrane to be impermeable and for it to achieve high proton conductivity, the membrane would have to be chemically stable and mechanically robust [31]. The aim of this investigation is to test the mechanical properties of two of the constituents of the membrane electrode assembly using molecular dynamics. The constituents considered is the polymer found in the membrane area, poly(2.5 -benzimidazole) (ABPBI) and the polymer found in the ionomer layer polytetrafluoroethylene (PTFE), of a high temperature polymer electrolyte membrane fuel cells (HTPEMFCs). These properties are studied at $298K$ and $383K$, of which $383K$ is within the HTPEMFC operational temperature and yet below the glass transition temperature of PTFE of $388K$ [60]. Above the glass transition temperature additional calculations would be required to take into account the change in phase [57].

ABPBI is an amorphous polymer [45] and a change in temperature results in changes of the tensile behaviour and physical state of the polymer [46]. In general; as temperature increases polymers change from being brittle to being more resilient, until it reaches a brittle-ductile phase [46]. As the temperature is increased, a decrease in the elastic modulus [47] and a reduction in the tensile strength [48] should be observed. At room temperature Zheng et al [252] investigated ABPBI and their results indicate the stress breakpoint to be $0.6MPa$ and yield stress to be $19.1MPa$. The form of PTFE considered is semi-crystalline. The degree of crystallinity influences the mechanical properties of a material [251]. The areas of crystallinity are those where molecular chains are closely packed and aligned in an orderly, parallel manner [251].

Helminiak et al [49] reported on the mechanical properties of ABPBI, specifically a modulus of $14.41GPa$. Liu et al [50] reported a value for Young's modulus for

78

anhydrous pristine ABPBI of $3.0 \pm 0.3 GPa$. Using molecular dynamics, Cagin [51] investigated the mechanical properties for poly(2,5-benzoxazole) ABPBO, ABPBI and poly(2,6-benzothiazole) ABPBT at room temperature. Cagin's paper however, only reports the bulk modulus and chain modulus for ABPBO and ABPBT. From Cagins work ABPBI is reported to have the highest chain modulus of the three polymers. The significance of this work is that through the technique of molecular dynamics, a theoretical Youngs modulus for ABPBI is determined at a temperature within the HTPEMFC operational range. For PTFE the Young's modulus was reported to be between $0.4 GPa$ and $0.522 GPa$ [52].

The second part of this study is an investigation of the interaction of ABPBI and PTFE, and in particular their miscibility. The solubility parameter, δ, used to determine miscibility is a measure of the degree of interaction between materials which works especially well as a measure for polymers [57]. If ABPBI and PTFE were to mix, the properties contributing to ABPBI having good thermal stability and proton conductivity [55, 54] would be altered and therefore it would imperative that mixing does not occur. In the event mixing does occur then the results of this investigation would give insight how durability, thermal stability and proton conductivity in the HTPEMFC can be improved. Hansen [53] proposed that liquids with similar solubility parameters, δ, are miscible and that polymers would dissolve in solvents with solubility parameters "not too different" from each other. For polymers, the solubility parameter is a thermophysical property that shows a high dependency on temperature [56, 57]. The solubility parameters of PTFE and ABPBI were determined as a function of temperature and compared to determine miscibility. As far as the authors are aware the solubility parameter of ABPBI as function of temperature and potential miscibility with PTFE, from a molecular dynamics approach has not been reported before. The known reported value for the solubility parameter for PTFE is $12.7 (J/cm^3)^{1/2}$ [58] and $27.43 (J/cm^3)^{1/2}$ for ABPBI [158].

79

4.2   Method

4.2.1   Mechanical Properties

A material undergoes deformation as a result of it undergoing an applied stress, $\boldsymbol{\sigma}$. Strain, $\boldsymbol{\varepsilon}$, a measure of deformation, is directly proportional to the applied stress up until the so-called elastic limit is reached [61, 41]. Hooke's law relates these two variables as follows:

$$\boldsymbol{\sigma} = S\boldsymbol{\varepsilon}, \tag{4.1}$$

where is S is a constant called the elastic compliance. The inverse of S is known as the modulus of elasticity, E, alternatively also known as the Young's modulus. Extended to three dimensions, the following relationship hold:

$$\boldsymbol{\sigma}_{ij} = S_{ijkl}\boldsymbol{\varepsilon}_{kl}, \tag{4.2}$$

and
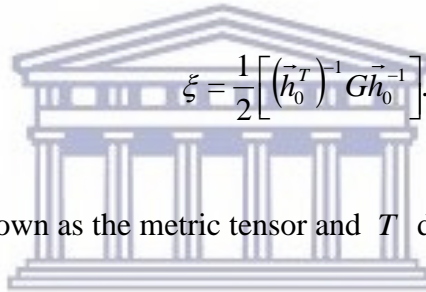
$$\boldsymbol{\varepsilon}_{ij} = C_{ijkl}\boldsymbol{\sigma}_{kl}. \tag{4.3}$$

Here the constant C is known as the elastic stiffness constant. C and S are 6×6 matrices. At the atomic level the Virial expression can be used to determine σ. This expression is given by [41]:

$$\sigma = -\frac{1}{V_0}\left[\left(\sum_{i=1}^{N} m_i(\vec{v}_i \vec{v}_i^{\,T})\right) + \left(\sum_{i<j} \vec{r}_{ij} \vec{F}_{ij}^{\,T}\right)\right], \tag{4.4}$$

80

where i is the running index over all particles. The mass, velocity, displacement and force vectors acting on particle i is denoted by m_i, $\vec{v}_i$, $\vec{r}_{ij}$ and $\vec{F}_i$. V_0 is the original system volume.

At the molecular level when a body experiences an applied stress the particles within it are displaced by a distance $\Delta\vec{r}$ and the resultant cell shifted as a repercussion hereof. A periodic cell can be represented by a three column vector at time instant zero as $\vec{h}_0 = [\vec{a}_0$, $\vec{b}_0$, $\vec{c}_0]$, and after a strain has been placed by $\vec{h} = [\vec{a}$, $\vec{b}$ $\vec{c}]$. The strain tensor with respect to these two column vectors is given by [41]:

$$\xi = \frac{1}{2}\left[\left(\vec{h}_0^T\right)^{-1} G \vec{h}_0^{-1}\right]. \tag{4.5}$$

$G = h^T h$, where G is known as the metric tensor and T denotes the transpose.

The elastic stiffness coefficients, C_{lmnk} relating the various components of stress and strain are:

$$C_{lmnk} = \frac{\partial \sigma_{lm}}{\partial \xi_{nk}}\Big|_{T\xi_{nk}} = \frac{1}{V_0}\frac{\partial^2 F}{\partial \varepsilon_{lm}\partial \varepsilon_{nk}}\Big|_{T\varepsilon_{lm}\varepsilon_{nk}}. \tag{4.6}$$

F is the Helmholtz free energy [41].

In FORCITE, a molecular dynamics software program, a constant strain approach is utilized [41] to calculate the mechanical properties for a sample. The constant strain approach is where the extension to which a sample is allowed to reach, is limited by what is termed the strain pattern. The strain amplitude is the maximum distortion the structure can have. For each sample and temperature the maximum distortion has to be determined. Intuitively the greater maximum distortion is tested for the higher temperatures. The recommendation taken into account was to exclude values less than 0.001 i.e. 0.1%

81

strain, as the resultant structures would be similar to each other. A second recommendation is to exclude maximum distortion values greater than 0.01, i.e. 1% strain, as it is likely to be beyond the structure's linear elasticity region [41]. The number of steps or number of distorted structures that can be taken to reach the maximum distortion can be adjusted. When this is 6, the resultant range is: $[-0.003, -0.0018, -0.0006, 0.0006, 0.0018, 0.003]$. Increasing the number of steps increases the computing time.

From the resultant dynamics simulated sample cell, a strain pattern matrix is determined by the symmetry of the input structure and is not editable [41]. Each strain pattern represents the strain matrix in Voigt notation. For a maximum amplitude of 0.003 the strain matrix would therefore be:

$$
\begin{pmatrix}
0.003 & 0.0015 & 0.0015 \\
0.0015 & 0.003 & 0.0015 \\
0.0015 & 0.0015 & 0.003
\end{pmatrix}.
$$

A stiffness matrix, $\mathbf{S}$ is built up from a linear fit between the applied strain and resulting stress patterns [41]. In the case of a trajectory this is averaged over all frames specified. The Young's modulus in Cartesian coordinates is calculated as follows:

$$E_x = S_{11}^{-1} \tag{4.7}$$

$$E_y = S_{22}^{-1} \tag{4.8}$$

$$E_z = S_{33}^{-1}. \tag{4.9}$$

4.2.2 Miscibility

The solubility parameter, δ, provides a quantitative guideline to compare and predict the cohesive and adhesive abilities of a material [62]. E_{coh}, which is the magnitude of the internal energy, U per unit volume, was the basis of the work done by Hildebrand [65, 63], Scott [64] and Scatchard [66]. The solubility parameter is determined by:

$$\delta = \sqrt{E_{coh}},$$ (4.10)

which can be written in terms of its molar energy of vaporization ($\Delta H_{vap} - RT$) divided by its molar volume as:
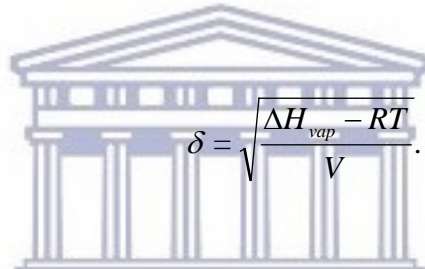
$$\delta = \sqrt{\frac{\Delta H_{vap} - RT}{V}}.$$ (4.11)

δ was further expanded by Hansen [53] to include effects contributed by dispersion forces, δ_d, by the polar forces, δ_p and by the hydrogen bonding forces, δ_h such that equation (4.10) for the solubility can be written as [57]:

$$\delta = \sqrt{\delta_d^2 + \delta_p^2 + \delta_h^2}.$$ (4.12)

In molecular modeling the cohesive energy density comprises of contributions made by the van der Waals (vdw) and electrostatic (Q) forces. δ in terms of these contributions is as follows:

$$\delta = \sqrt{\delta_{vdw}^2 + \delta_Q^2}.$$ (4.13)

In the work done by Chen et al [57], where molecular modeling was done to investigate the temperature dependence of solubility parameters for amorphous polymers, very good

83

agreement was found between experimental and computational results. In light of the investigation and equation (4.11), it is anticipated that the solubility parameter for ABPBI would decrease with increase in temperature.

4.3   Computational Procedure

The mechanical and solubility property investigation of ABPBI and PTFE was done using molecular dynamics. The computational results in this work were obtained using software programs available from Accelrys Software Inc. The molecular dynamics calculations were performed with the FORCITE program, and graphical displays generated with Materials Studio.

The sample cell created for PTFE had a chain length of 80 repeat units and the number of chains loaded was 3. An initial density of $2.15 g/cm^3$ was set and built at random torsion angles in AMORPHOUS Cell. AMORPHOUS Cell is a software package provided within the Materials Studio suite. A geometry minimization procedure was performed to optimize the cell. For the geometry minimization the SMART algorithm was used, which is a cascade of methods successively using steepest descent and conjugate gradient algorithms. A Condensed-phase Optimized Molecular Potentials for Atomistic Simulation Studies [24] (COMPASS) forcefield was used, which is suitable for materials investigated here. A 50 ps canonical, NVT molecular dynamics simulation was performed, followed by $800 ps$ and 1500 ps isothermal-isobaric, NPT simulation dynamics for ABPBI and PTFE respectively. NVT and NPT ensembles indicate the parameters held constant during the simulations where the number of particles is denoted with N, the volume with V, the pressure P and the temperature, T. The larger simulation dynamics for PTFE was required to ensure an adequate period of investigation that falls within the convergence criterion. A time step of $1 fs$ was used in all simulations. Temperature and pressure was controlled using the Nosé thermostat [68, 67] and Berendsen barostat [69].

84

4.4   Results and Discussion

The resultant simulated cells for PTFE and ABPBI are displayed in figures 4.1 and 4.2 respectively, where the light blue atoms are representative of fluorine, grey carbon, white hydrogen while dark blue represents the nitrogen atoms.
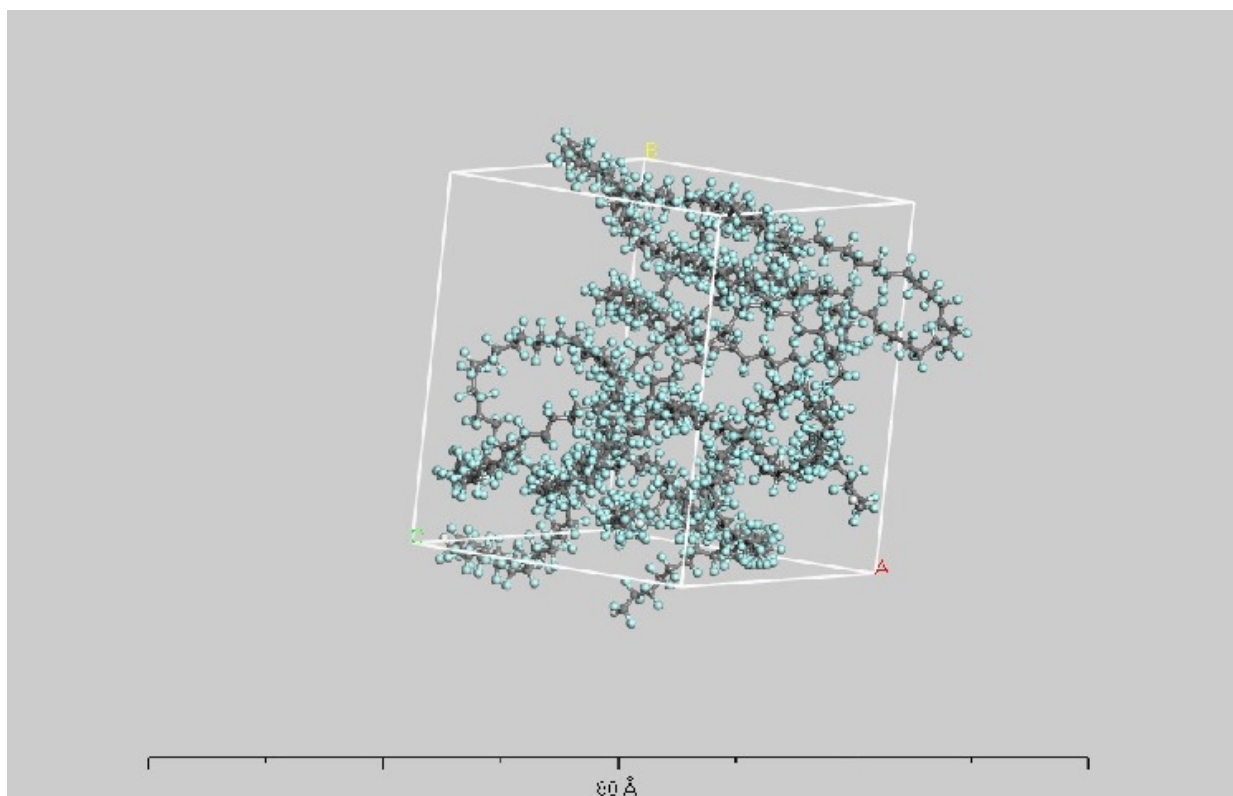
Figure 4.1: Illustration of simulated cell of PTFE

85
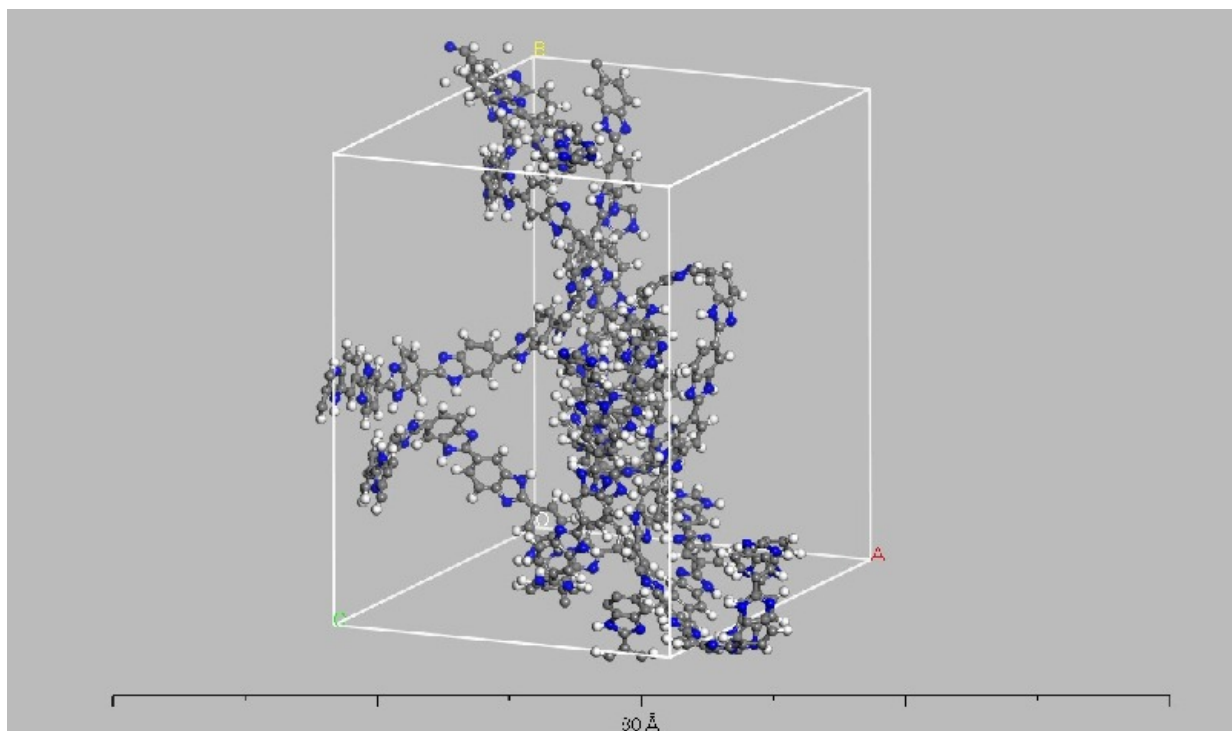
Figure 4.2: Illustration of simulated cell of ABPBI

4.4.1 Density

The density for PTFE at atmospheric pressure for temperatures of $298K$ and $383K$, was $1.70 \pm (4.2 \times 10^{-1}) g/cm^3$ and $1.60 \pm (3.9 \times 10^{-1}) g/cm^3$ respectively. For 100% crystalline PTFE at $25°C$ a density of $2.302 \times 10^{-1} g/cm^3$ [71] was found and $2.00 g/cm^3$ [70] for amorphous PTFE. The density of the ABPBI sample at atmospheric pressure was $1.200 \pm (7 \times 10^{-3} g/cm^3)$. Li et al [39], after molecular dynamics simulations and investigations, reports a density for neat ABPBI to be $1.173 g/cm^3$. He attributes higher densities found in experimental work, [70,71] to be a consequence of the refinement of polybenzimidazole structures in post-treatments. For both polymers the density is within range of respective published work [70,71] and is used here as one of the guides to ensure that the material modelled is a true representative of what is found elsewhere.

86

4.4.2 Wide Angle X-ray Diffraction

The X-ray diffraction patterns shown in figures 4.3 and 4.4 were calculated using the REFLEX module available from Materials Studio, where $\lambda = 1.5418\,\text{Å}$, Cu K$\alpha$ radiation was used for 2θ between 5 and 45° with a 0.05° step. In experimental investigations of PTFE, Lebedev et al [253], found similar patterns for samples of PTFE where the composition consisted of percentages of crystalline and amorphous phases. In figure 4.3 a broad peak was found at approximately $2\theta = 38^\circ$, representative of the amorphous sections of the sample and a narrower peak, with far greater intensity at approximately $2\theta = 17^\circ$. For the narrower peak this corresponds to a d-spacing of $5.2\,\text{Å}$ between parallel PTFE chains. The X-ray diffraction pattern for ABPBI has a broad peak centered approximately between $2\theta = 18^\circ$, where this display the amorphicity of the sample. This is in agreement with work done by Li et al [13], whereby using molecular dynamics, they found the broad peak for ABPBI to be 16.8°. The figures compare the two temperatures and the results display that with an increase in temperature the intensity of these peaks increases.

87
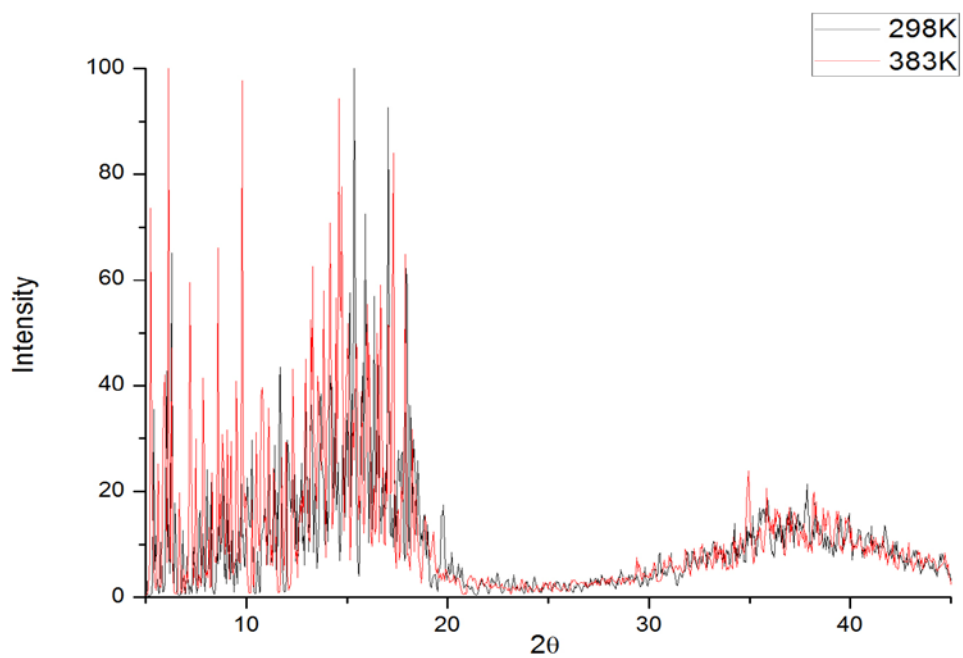
Figure 4.3: The X-ray diffraction pattern for semi-crystalline PTFE
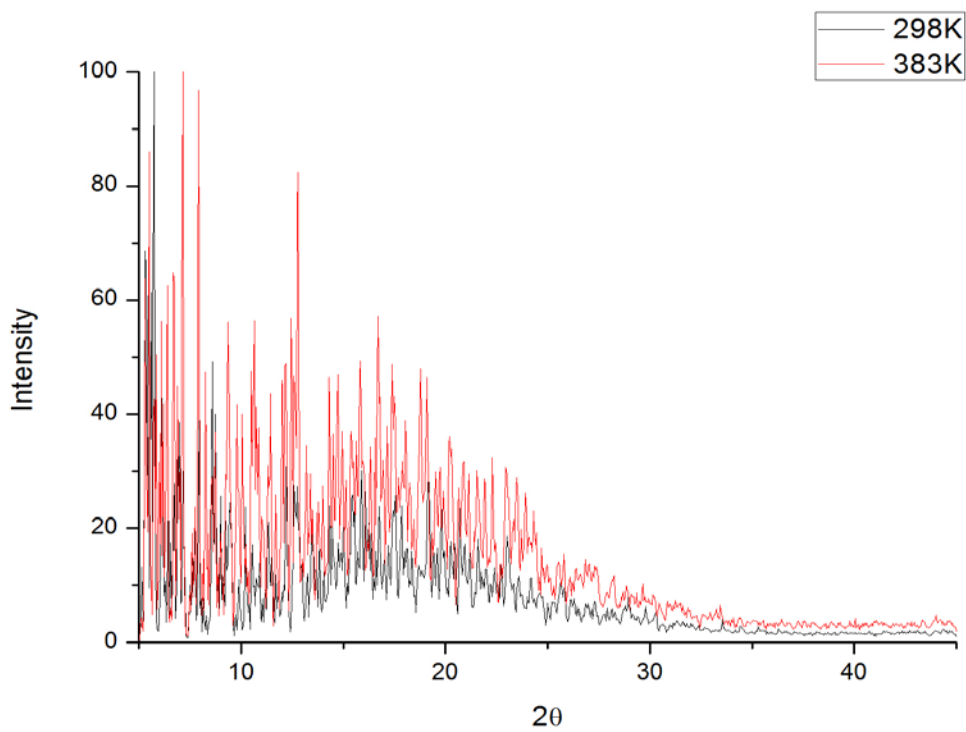
Figure 4.4: The X-ray diffraction pattern for amorphous ABPBI

88

4.4.3 Mechanical Properties Calculation

For the mechanical properties calculation the last 20 frames of the NPT calculation was considered. The cells were optimized and the number of strains considered was 4. For each frame the cell would reach maximum distortion in four steps. At each step the respective cell is subjected to stresses such that the Young's, shear and bulk modulus can be calculated. The overall mechanical properties for a specified maximum distortion is calculated then as an average of the number of frames considered in the calculation. The Young's modulus is given with respect to x, y and z Cartesian directions and uncertainties determined using propagation of uncertainty of calculated results.

The maximum strain amplitude, indicated in table 4.1, shows that as temperature increases the maximum strain determined is greater. This can be interpreted as, for the same stress applied to two samples of a polymer, the sample at higher temperature would experience a greater strain, resulting in a lower Youngs modulus. This corresponds to what is to be expected of polymers below glass temperature, where the Youngs modulus decreases as temperature increases [42]. This could be as a result of increased temperature increasing the thermal motion of the polymer chains and in doing so may result in the breaking of bonds [43]. At $298K$ the Youngs modulus for ABPBI is from approximately 2.1 to 3.8 GPa which is in good agreement with reported experimental values of $3.0 \pm 0.3 GPa$ [50]. Similarly, Zheng et al [252] found values of 1.78 GPa for ABPBI abd 2.38 GPa for porous ABPBI. Boa et al [254] however found the Youngs modulus of pure ABPBI to be $1.30 \pm 0.38 GPa$, and this difference could be as a result of structural changes occurring during membrane casting and preparation. The Youngs modulus with respect to each direction can be found in table 4.1. As temperature increases, the Youngs modulus for ABPBI range shifts from $[2.16 \quad 3.79]$ GPa at $298K$ to $[1.1 \quad 2.6]$ at $383K$. This shows that even at elevated temperatures ABPBI displays mechanical robustness which is suitable for HTPEMFC operation.

	ε_{max}	E_{xx}	ΔE_{xx}	E_{yy}	ΔE_{yy}	E_{zz}	ΔE_{zz}
ABPBI (298K)	3×10^{-3}	2.10600	0.00840	3.79110	0.01315	3.00670	0.02988
ABPBI (383K)	6×10^{-3}	1.13770	0.03218	2.58300	0.00809	2.25270	0.00591
PTFE (298K)	5×10^{-4}	0.42180	0.00270	0.46440	0.00193	3.14450	0.00127
PTFE (383K)	4×10^{-3}	0.08840	0.00017	0.20330	0.000017	0.17230	0.00024

Table 4.1: The maximum strain, ε_{max} and Young's Modulus for ABPBI and PTFE at 298K and 383K and 1×10^{-4} (GPa)

For PTFE, the Young's modulus with respect to xx and yy directions range between 0.42 and 0.47 GPa. This is in very good agreement with reported experimental results which range from $0.4GPa$ to $0.522GPa$ [52]. In the zz direction, E_{zz} for PTFE is not similar to that of the other two directions and is most likely as a result of a maximum strain value less than 0.001, which could be influenced by computational noise [41]. At $383K$ PTFE Young's modulus reduces signifantly to range from 0.08 to 0.2 GPa. This shift in Youngs modulus is unfavourable for the mechanical robustness desired for HTPEMFC operation.

4.4.4 Miscibility calculation

Figures 4.5 and 4.6 are plots of the solubility parameters as a function of temperature for PTFE and ABPBI respectively. At $298K$ δ for PTFE lies within a range of $[10.70-11.03](J/cm^3)^{1/2}$ and is close to reported values for it of $12.7(J/cm^3)^{1/2}$ [58]. In agreement with Chen et al [57] the trend for the solubility parameter for both polymers, decreases as temperature increases. When evaluating the reduction of the solubility parameter, for ABPBI the greatest change is found when temperature is increased from

90
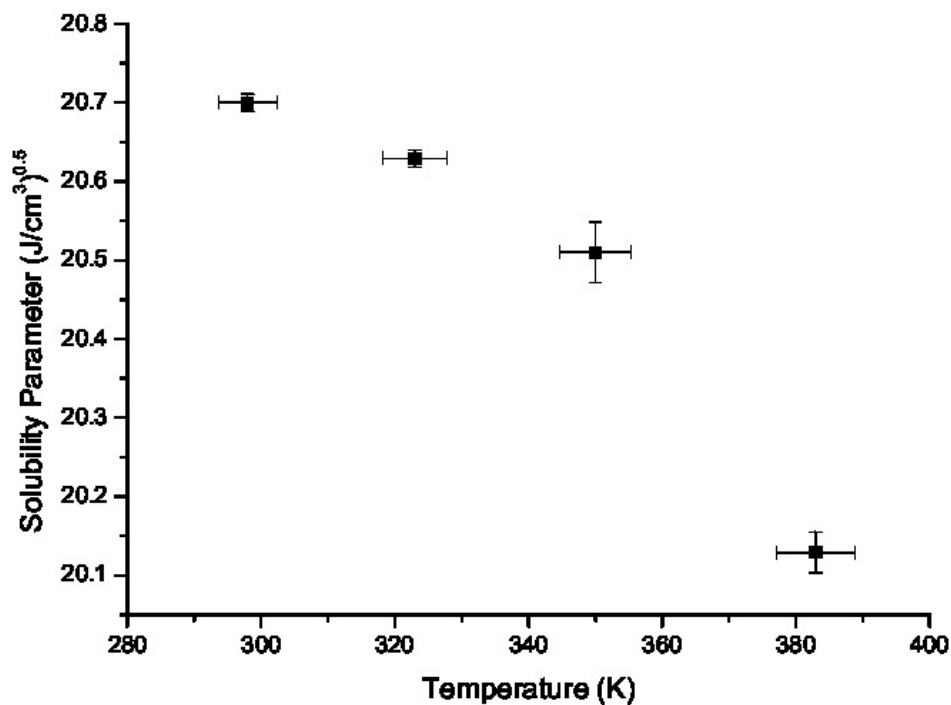
$350K$ to $383K$.

Figure 4.5: Solubility parameter of ABPBI as a function of temperature

For the PTFE however, this increase in temperature from $350K$ to $383K$ gives solubility parameter values within range of each other and could be as a result of the temperature being very close to PTFEs' glass transition temperature.

91
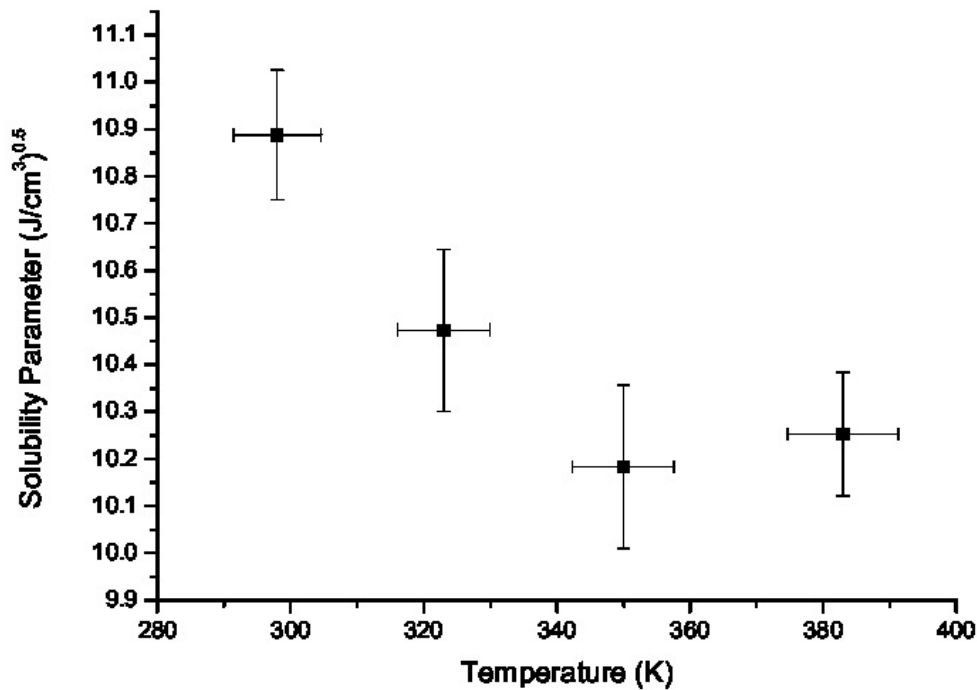
Figure 4.6: Solubility parameter of PTFE as a function of temperature

In order to establish mixing between two materials their solubility parameters can be compared, where similar values support mixing. Table 4.2 specifically compares $298K$ and $383K$ for ABPBI and PTFE. At $298K$ the difference between the solubility parameter values is $\Delta\delta = 9.812(J/cm^3)^{0.5}$ and $\Delta\delta = 9.876(J/cm^3)^{0.5}$ at $383K$. Despite ABPBI and PTFE initially at $298K$ having solubility parameter very different from each other, results support that even as temperature increases to $383K$ a scenario where ABPBI's solubility decreases dramatically and PTFE's reduces slightly which would result in their solubility parameters to be similar to one another, does not occur. Therefore since the two polymer values for δ are not closely related, even at $383K$, no mixing can be expected. This result is an attractive characteristic for a fuel cell with these materials. In chapter 3 the solubility parameter for phosphoric acid was found to range from $45.15\ (J/cm^3)^{1/2}$ to $39.69\ (J/cm^3)^{1/2}$ as temperature increased from $298K$ to $393K$.

92

ABPBI and phosphoric acid can be found in the membrane electrode assembly and the great difference between the values of their solubility parameters infer that the interaction between these two materials are most likely by means of a chemical reaction.

	δ $((J/cm^3)^{0.5})$	$\sigma_\delta ((J/cm^3)^{0.5})$
ABPBI (298K)	20.700	0.011
PTFE (298K)	10.888	0.138
ABPBI (383K)	20.129	0.026
PTFE (383K)	10.253	0.131

Table 4.2: Solubility parameter comparison for ABPBI and PTFE at temperatures of 298K and 383K and pressures of $1 \times 10^{-4} GPa$

A change in δ can be as a result of any of the three contributing factors mentioned in equation 4.12. For ABPBI the δ_h contributor is significant as it assists with hydrogen bond formation. Hydrogen bond formation within the membrane electrode assembly forms the hydrogen bonded network which, amongst other facilitators, assists with proton transfer. Since the reduction in δ is approximately 0.02% as temperature increases, it is reassuring that even if this reduction was only as a result of δ_h, this value change is very low.

4.5   Conclusion

In this work molecular dynamics was used to determine the mechanical and solubility properties of ABPBI and PTFE at $298K$ and $383K$. As temperature increases mechanical and solubility properties decrease indicating the relaxation of the polymers. ABPBI, at room temperature and at $383K$, shows good mechanical properties and the small change in the solubility parameter as temperature is increased. Both these qualities support good proton conductivity. The consequence of the findings found in this work suggest that given the drastic decrease in the mechanical properties of PTFE at elevated

temperatures that limited quantities be used. Results too confirms that ABPBI is an excellent candidate for high temperature polymer electrolyte fuel cells.

Chapter 5: Hydrogen Bonded Network Variation with Increase in Pressure of Doped poly(2,5-benzimidazole) Membrane

Abstract

In this work Molecular Dynamics was used to investigate the relationship between high pressure and one of the factors contributing to good proton conductivity for phosphoric acid doped poly(2.5 -benzimidazole) membranes. The pressure range considered is 1.0×10^{-4} GPa to 7.5×10^{-1} GPa. The factor contributing to good proton conductivity focused on this work if the hydrogen bonded network. A method where the number of hydrogen bonds is counted was utilized to determine the variations in the strength of the hydrogen bonded network as function of pressure. The diffusion coefficients of the atoms representative of the molecules involved were investigated and included to gain a more insight on the proton transfer. Proton conductivity is dependent on the strength of the bonded network and diffusion of proton donor and carrier particles, and therefore its effects can be deduced. Findings support that the number of hydrogen bonds increases as pressure increases and the diffusion coefficients of elements representative of both the polymer and water molecules increase with pressure for a doped, hydrated sample at $453K$. A ratio of $1:3:2.5$ and $1:1.5:1.25$, (polymer: phosphoric acid: water) is considered and compared for temperatures of $298K$ and $453K$. The radial distribution function for the polymer - acid, polymer - water and acid - water interactions was calculated and supports the results found from the hydrogen bond counting method. The proton conductivity has previously been reported to increase as the levels of hydration and acid content increase, and this too is observed when temperature is increased. Each of these methods to improve proton conductivity can further be enhanced by increasing the pressure. The hydrogen bonded network dependency on pressure has not been reported

before.

5.1 Introduction

In the summary done by Kreuer [16] an overview of the models used for proton conductivity is discussed. There are a number of mechanisms limiting proton-conduction; however, the two most important are vehicle and Grotthuss type mechanisms [36]. Vehicle type mechanisms refer to those where the protons travel through a medium referred to as the "vehicle" or a proton solvent. In the Grotthuss-type mechanism, through formation and breaking of hydrogen bonds, protons are transferred from one site to another [27, 40]. This is also termed proton hopping. Therefore proton conductivity is strongly dependent on the rate of diffusion, D, reorganization of the proton environment, and the proton-transfer rate. In comparison to other types of bonds, the hydrogen bond is a weak directional interaction, a characteristic which makes it extremely flexible and adaptable to its environment and sensitive to thermal variations [16]. The hydrogen bond plays a significant role by providing a path for proton transfer from a proton donor to a proton acceptor. In the work done by Maréchal [33], proton transfer along hydrogen bonds appears to limit the overall proton conductivity. As a result hereof, proton transfer through H-bonds can be considered as a third fundamental property.

The transport of protons within the polymer membrane is regarded as a sequential movement of protons along the hydrogen-bond network [31, 188]. The rate by which protons move in the polymer membrane results from the rate at which hydrogen-bonds are formed and broken [31]. The hydrogen bonded network is formed between the constituents of the membrane and provides the path for proton transfer. Therefore one of the precursors for proton transfer is effective hydrogen bonding and reformation, and structural reorganization [12, 18]. High proton conductivity within the fuel cell membrane is essential for achieving a high power density in the fuel cell [12]. One method considered to maintain good conductivity at elevated temperatures is to increase the proton conductivity [17]. For the high temperature fuel cell and in this particular study, the specific species

96

considered is phosphoric acid, poly(2,5)benzimidazole (ABPBI) and water.

Proton transport using molecular dynamic (MD) techniques for the Nafion membrane has been investigated quite extensively [20, 21, 22, 23]. Some of the more recently published work, done by Hofmann et al   [26] produced MD simulations of proton conductivity using a reactive force field for water in a Nafion membrane. The simulations showed that different acid strengths affect proton transport. Sun et al [28] used MD and quantum mechanics (QM) to investigate the proton transfer reaction in the poly(2,5-polybenzimidazole) ABPBI using a molecule simulation technique. The influence of cell temperature and doping content in the ABPBI on the proton transfer was analysed, and the findings support the hypothesis that the doping content controls the proton transfer mechanism. In addition the proton transfer rate increases with increasing temperature, which is a consequence of the growth of transfer reactivity. Vil č iauskas et al [29] performed first principle MD simulations to investigate proton dynamics in phosphoric acid imidazole $2:1$ mixtures. Their results indicate that the local structural, energetic and dynamical effects arise from a reduction in proton density in the proton conducting H_3PO_4 phase, which they conclude is due to the proton transfer from acid to base, and the formation of a very stable imidazolium-dihydrogenphosphate complex. From this they conclude that the changes in the internal charge separation directly influences the local electrostatics of the system, which has a substantial effect on the H-bond network of phosphoric acid. Li et al [14] performed atomistic simulations on neat, hydrated and phosphoric acid doped poly(2,5-benzimidazole) and reported the effects of water concentration, doping level and temperature on hydrogen bonding and vehicular diffusion.

In 2003, Bendler et al [10] developed a defect diffusion model and concluded that for ion doped polymers, ion jumps are connected to the temperature and pressure and is dependent on the concentration of mobile defects. The aim of the current investigation is to gain insight on how the hydrogen bond network changes due to pressure. Studying this together with the variation of diffusion coefficients as a result of changes due to pressure, obtain improved understanding of how proton conductivity changes within phosphoric acid doped

97

poly(2,5-benzimidazole). Protons transfer in a fuel cell membrane along the hydrogen bond network through structural diffusion and occurs in the time scale of picoseconds [19]. The diffusion of the proton carrier between hops and vehicular diffusion, occurs in the time scale of nanoseconds [13]. To study this phenomenon materials modelling is therefore used since it allows for greater numbers of atoms and a longer simulation time. MD is a technique used for computing the equilibrium and transportation properties of a classical many body problem [37, 38]. The advantage of this method is that computations are quicker than quantum mechanical modelling since the electronic component of the atoms is not considered. To account for some of the electronic properties in this work, i.e. bond formation, we consider a hydrogen bond to have formed if and only if the following two criteria are met [15]:

 • hydrogen bond donor and acceptor are found to be less than 2.4 Å apart and

 • hydrogen bond donor and acceptor are at an angle greater than $90°$ with respect to each other, where a hydrogen bond is mainly determined by the distance between the proton donor and acceptor distance [16].

To support the results found from the hydrogen bond counting method, the radial distribution function for the hydrogen donor and acceptor was calculated focussing on the same distance, r of 2.5 Å, which corresponds to a hydrogen bond.

5.2 Method

The purpose of this study is to investigate the effects of pressure on proton transfer across the fuel cell membrane. Proton-transfer across the membrane is assisted through the hydrogen bonded network and vehicle diffusion. In this study the hydrogen-bonded network consists of phosphoric acid, poly(2,5)benzimidazole (ABPBI), and water. The donor and acceptor atoms which allow for the proton transfer and the notation for each is tabulated in table 5.1. The donor and acceptor notation utilized here are forcefield-assigned within Material Studio and COMPASS. The graphical atomic models are shown in figure 5.1.

Interacting Species	Donor and Acceptor Pairs		
Polymer - Water	n2a-o2*	n3a-o2*	
Polymer - Acid	n2a-o2	n3a-o2	n3a-o1=
Polymer - Polymer	n3a-n2a		
Water - Water	o2*-o2*		
Water - Acid	o2*-o2	o2-o2*	o2*-o1=
Acid - Acid	o2-o1=	o2-o2	

Table 5.1: The Polymer, Acid and Water donor and acceptor pair combinations for hydrogen bond formation.
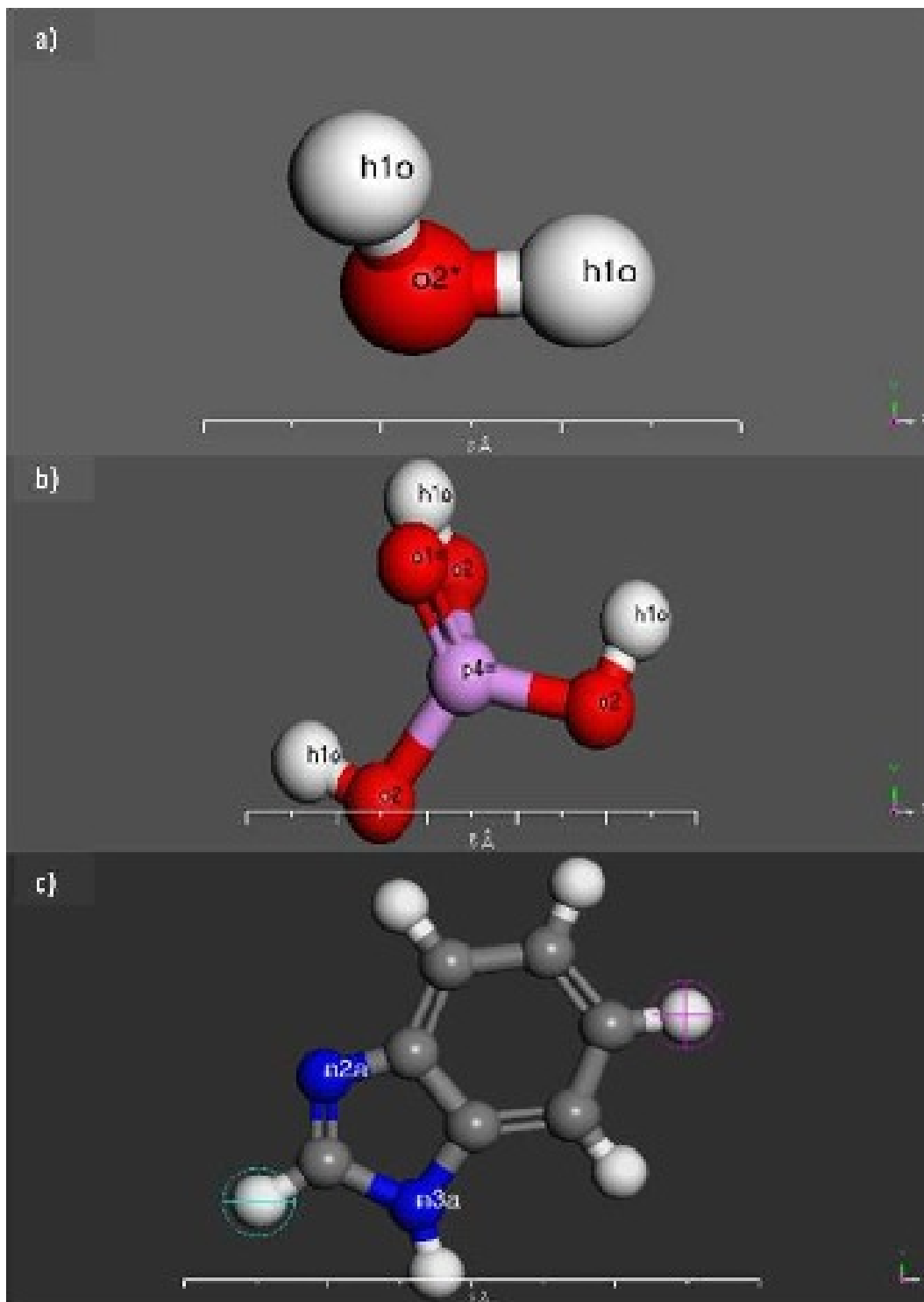
Figure 5.1: figure a)Water's hydrogen bond donor atom $o2*$ **and** $n2a$ **acceptor atom b) Phosphoric acid's hydrogen bond donor** $o2$ **and acceptor atoms** $o2, o1 =$ **and c) Poly(2.5 -benzimidazole) hydrogen bond donor** $n3a$ **and acceptor** $n2a$ **atoms.**

100

The manner by which the hydrogen bonded network variation is evaluated is by counting the number of possible hydrogen bonds, as previously implemented in the work done by Li et al [39], where their investigation included $298K$ and $453K$ at 1.0×10^{-4} GPa. More detail on biological applications of this method can be found in the work done by Torshin et al [15] and Durrant et al [2]. The first part of this investigation reports how the total number of hydrogen bonds changes with an increase in pressure for all samples, at $298K$. To investigate the effect of temperature and pressure, the same composition is investigated at $453K$ and subsequently the effect of pressure on the number of hydrogen bonds is evaluated. To investigate the effect of pressure on different levels of doping and hydration, different compositions are considered. Since the fuel cell under consideration is for high temperature fuel cell operation, special consideration, by means of the radial distribution function calculation, is given to the $453K$ sample (with the highest number of hydrogen bonds).

The radial distribution function (RDF), denoted as $g_{A-B}(r)$ which gives for an atom pair, (A and B), the probability of finding B separated from A by a distance r [38], is given as follows:
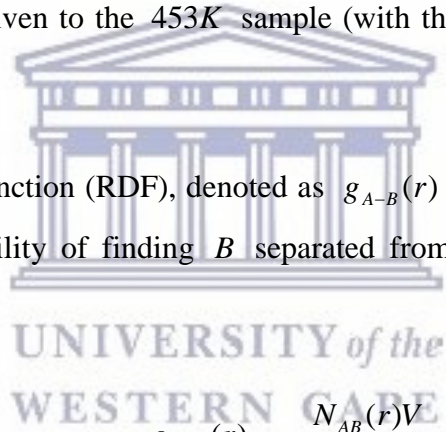
$$g_{A-B}(r) = \frac{N_{AB}(r)V}{N_B N_A 4\pi r^2 dr},$$ (5.1)

where N_{AB} is the number of atoms of type B in the spherical shell surrounding A from radius r to $r+dr$, and N_A and N_B the total number of atoms of type A and B respectively. X-ray diffraction patterns were determined, which are used to calculate the intersegmental/ d-spacing of a material. This is useful for deducing the crystallinity of the structure. The diffusion coefficient, D, was calculated by applying the Einstein equation [35]:

101

$$D = \lim_{t \to \infty} \frac{1}{6t} <|r(t) - r(0)|^2>, \tag{5.2}$$

where $<|r(t) - r(0)|^2>$ is the mean square displacement, the angular brackets the ensemble average and $r(t) - r(0)$ is the vector distance traveled by particles over the time interval of length t. The square magnitude of this vector is averaged over many time intervals.

Fractional Free Volume

Free volume is considered to be the difference between the total volume and the occupied volume and the fractional free volume, the ratio between free voume and total volume [285]. In a study by Matilla[286] on polymer films for breathable textiles, the fractional free volume inceases with temperature according to the respective equations and concluded that this provided more paths for water molecules to pass through the membrane. This increase in free volume and micro-Brownian motion, as a result of the increase in temperature, increases the intermolecular gap enough to allow water vapor molecules to pass through the membrane in the samples considered in their study [286].

For polymers below glass temperature the free volume is determined as follows [287]:

$$f = f^\circ + \frac{C}{M} \quad \text{and} \tag{5.3}$$

$$f \sim (C_2 + C_3 T) + \frac{C}{M} \tag{5.4}$$

Where f° is the fractional free volume, C, C_2, C_3 constants and M the molar mass. The implications of the above equations are that as temperature increases the free volume increases. A deduction hereof would be that the distance between species to increase with increase temperature and this would affect the first criterion for the hydrogen bond in this study. Therefore the number of hydrogen bonds for the higher temperature sample should be less.

Intuitively, it is anticipated that increasing the pressure would reduce the distance between species, reduce the free volume and increase the number of hydrogen bonds according to

102

the stipulated criterea.

Activation Energy

According Na Ni [288] activation energy E_a is the summation of the enthalpy for proton transfer and the defect migration. These two contributors indicate the ease with which proton hopping may occur and the rotation of the donor and acceptor [288]. This relationship leads to the following conclusion, that a high E_a leads to a enthalpy for proton transfer which in turn leads to low proton conducivity [288]. In their investigation of anhydrous H_3PO_4 doped ABPBI/3SO-POSS composite membranes and ABPBI membranes they found that increasing the doing level decreased the E_a. The conclusion they drew was that increasing the level of doping reduced the enthalpy required for proton transfer along the H_3PO_4 and that it was lower than that of the imidazole groups. With this insight, the results found here could mimic the results they found experimentally in that higher proton transfer is found with an increase in doping levels and the likely path for the transfer to be along the acid molecules. Where in this study proton transfer is monitored through an increase in the number of hydrogen bonds formed. What would be interesting to see is which path for proton transfer is favoured when the pressure is increased.

5.3   Computational Procedure

The computational results in this work were obtained using software programs from Accelrys Software Inc [41]. The molecular dynamics calculations were performed with the FORCITE program, and graphical displays generated with Materials Studio. The MD work done by Li et al [14] is in good agreement with experimental results, and the ratio for the acid doping and water molecules to the *ABPBI* monomer, was based on averaging the experimental work done by Asensio et al [3, 5] for the acid weighting, and Diaz et al [7] for the level of hydration. Diaz et als' [7] work reports a level of hydration in their samples ranging from 0.78 to 0.95 . The acidity levels tested in Asensio et al' [3] work corresponds to a ratio of 1:1.5 and 1:3 for *ABPBI* :Phosphoric acid. Using this method,

103

sample cells were created with a ratio for $ABPBI:H_3PO_4:H_2O$ of $1:3:2.5$, $1:1.5:1.25$. An additional sample of $1:3$ at a temperature of $453K$ for $ABPBI:H_3PO_4$ was created, to take into account a dehydrated sample at elevated temperatures. The polymer chain length consisted of 80 repeat units, built at random torsion angles. A geometry minimization procedure was performed to optimize the cell. For the geometry minimization the SMART algorithm was used, which is a cascade of methods successively using steepest descent and conjugate gradient algorithms. The traditional minimization techniques tend to be unable to overcome energy barriers, and fall into the nearest local minimum; however, through annealing the system over a few temperature cycles the best minimum can be achieved [34].

A Condensed-Phase Optimized Molecular Potentials for Atomistic Simulation Studies [24] (COMPASS) forcefield was used, which is suitable for materials investigated here. For cell equilibration a 50 ps molecular dynamics simulation was performed and thereafter $3ns$ constant volume, constant temperature (NVT) dynamics for the diffusion property calculations. 300 ps isothermal-isobaric NPT dynamics was used for the hydrogen bond counting investigation, RDF and XRD calculations. The first 50 ps simulation allows the cells' pressure and temperature to converge to the required values before further dynamics is performed. A time step of 1 fs was used in all simulations [41].

Temperature and pressure was controlled using the Andersen thermostat [25] and Parrinello-Rahman barostat [9]. The Parrinello-Rahman method allows the shape and size of the simulated cell to change under external pressure. The version used in Forcite is the one modified and described by Martyna et al [8, 41]. The Hamiltonian, H of the system is given as:

$$\mathbf{H} = \frac{1}{2}\sum_{i=1}^{N}m_i\dot{\mathbf{s}}_i^T\cdot\mathbf{G}\cdot\dot{\mathbf{s}}_i + \sum_{i=1}^{N-1}\sum_{j=i+1}^{N}\phi(\mathbf{r}_{ij}) + \frac{1}{2}QTr(\mathbf{h}^T\cdot\dot{\mathbf{h}}\cdot\dot{\mathbf{h}}\cdot\mathbf{h}^{-1}) + p_0\Omega. \tag{5.5}$$

104

In the equation, m is the mass of atom i, $\mathbf{s}$ its fractional position and $\dot{\mathbf{s}}$ the time derivative of $\mathbf{s}$. $\mathbf{h} = [\mathbf{abc}]$ is the cell vector matrix where the metric tensor is $\mathbf{G} = \mathbf{h}^T \cdot \mathbf{h}$. where Q is the rate of change of the volume matrix [41], as in the case of Martyna et al [8] modification and ϕ is the interaction potential of atoms. The kinetic energy, $E_{kin,V}$ is given by the following equation:

$$E_{kin,V} = \frac{1}{2} Q_{PR} Tr(\mathbf{h}^T \cdot \dot{\mathbf{h}} \cdot), \qquad (5.6)$$

The dot above $\mathbf{h}$ are indicative of the time derivative of $\mathbf{h}$ and T for the transpose of a variable. The Ewald summation method was used to compute the non-bond energies in the periodic systems. After the production runs, a Perl script code, found in appendix B and created to count the number of eligible hydrogen bonds based on the donor-acceptor criterion, was executed.

5.4   Results and Discussion

5.4.1   Hydrogen bond counting

The resultant, simulated cell of a $ABPBI : H_3PO_4 : H_2O$, $1 : 3 : 2.5$ ratio was created in Materials Studio and is illustrated in figure 5.2. The average number of hydrogen bonds and its standard deviation was calculated over the last 100 ps of the molecular dynamics simulation, where the convergence criterion is met. Figures 5.3 to 5.6 show the results using this method, where the overall trend shows an increase in the number of hydrogen bonds with an increase in pressure. When determining the number of hydrogen bonds formed between two materials, all combinations of donor and acceptor pairs is considered.

105
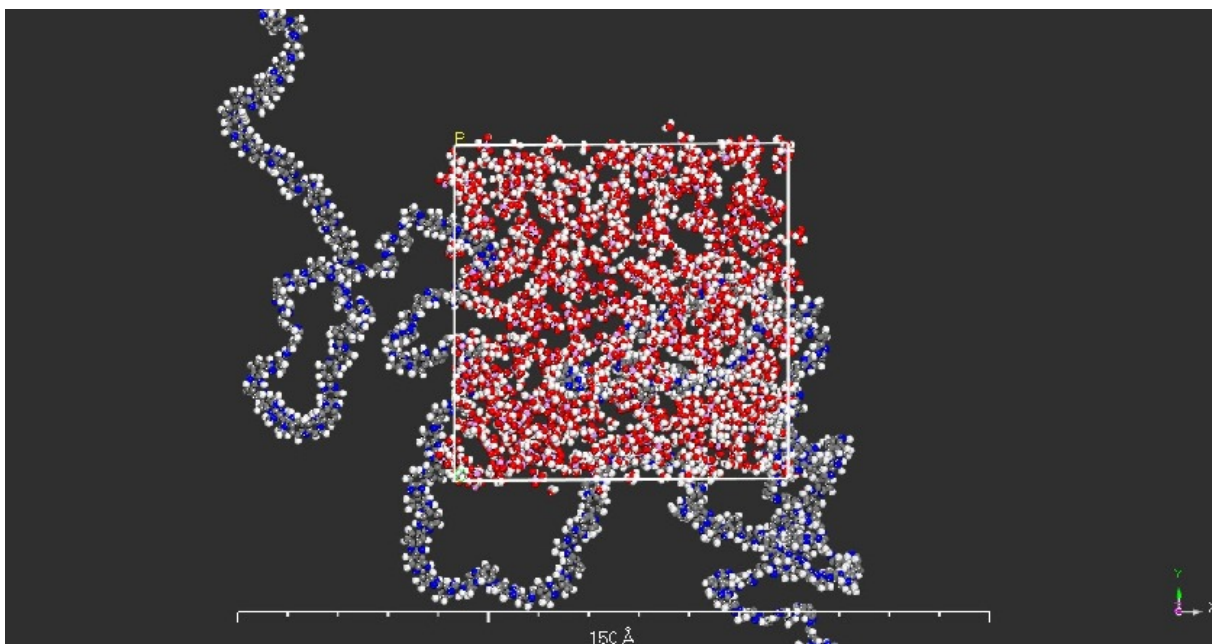
Figure 5.2: Molecular Dynamics simulation cell consisting of $ABPBI : H_3PO_4 : H_2O$, $1:3:2.5$ **ratio.**

Figure 5.3 reveals that each of the samples' total number of hydrogen bonds increases with increasing pressure. The $1:3:2.5$ sample at $298K$ has the most hydrogen bonds, followed by the $453K$ sample of the same composition. The difference in the number of hydrogen bonds between $298K$ and $453K$ $1:3:2.5$ samples decreases as the pressure increases. The $1:1.5:1.25$ sample at $453K$, has the least number of hydrogen bonds, however, as pressure increases this number too, increases. Notably the dehydrated sample at $453K$ at atmospheric pressure has approximately the same number of hydrogen bonds as that the $1:1.5:1.25$ sample at $298K$. As the pressure increases however the dehydrated sample supersedes the $1:1.5:1.25$ sample at $298K$ in number of hydrogen bonds. A deduction from these results is that the ratio of ABPBI to PA is of greater significance than that of the level of hydration.

106
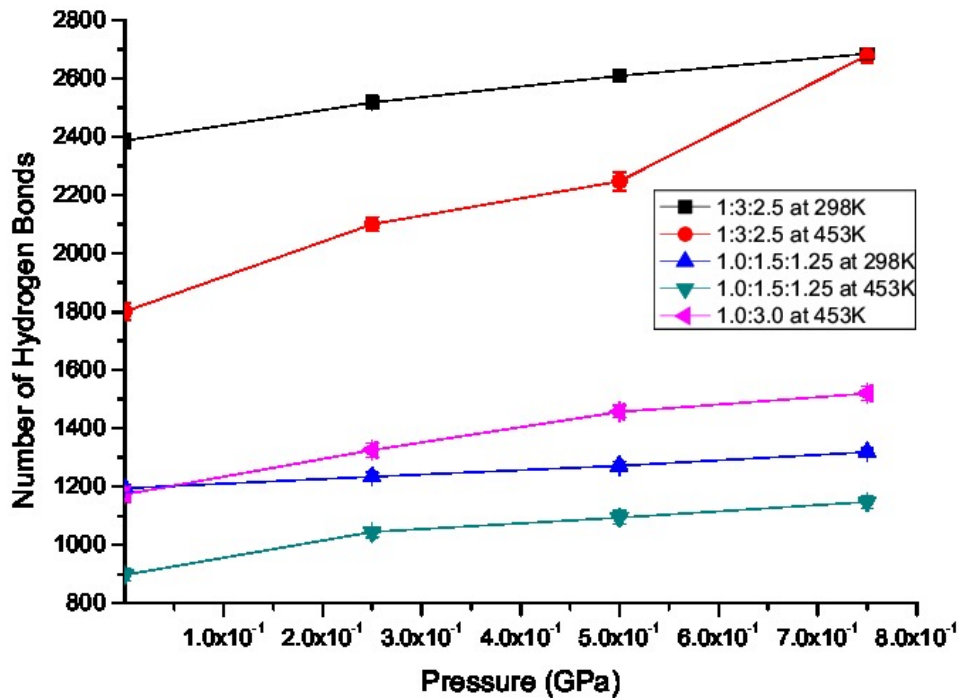
Figure 5.3: The total number of hydrogen bonds at 298K and 453K for samples of 1:3:2.5, 1:1.5:1.25 and 1:3:0 (ABPBI: PA: WATER doping ratios) as pressure increases.

Figure 5.4 shows specific specie interaction for the $1:1.5:1.25$ samples and the comparison between $298K$ and $453K$ as pressure increases. At $298K$, as pressure increases, the number of hydrogen bonds increases for all interacting species except the polymer - water and polymer - polymer pairs. This trend is also observed at $453K$, however, the number of hydrogen bonds for water - water interaction pairs remains approximately the same. When comparing $298K$ and $453K$ at 1.0×10^{-4} GPa, the number of hydrogen bonds in the $298K$ scenario is substantially greater than at $453K$. This would be a result of the free volume increasing as temperature increases. This is also true for all interacting species except for the polymer - polymer and water - water pairs, where they remain within range of each other. At the higher pressure, the difference between the number of hydrogen bonds at the different temperatures is less. Notably, the

107

$453K$ sample at 7.5×10^{-1} GPa is within range of the $298K$ at 1.0×10^{-4} GPa. This implies that for this doping ratio when the pressure reaches the 7.5×10^{-1} GPa range, only then does the sample at $453K$ sample have hydrogen bonds comparable to its $298K$ counterpart at atmospheric pressure.
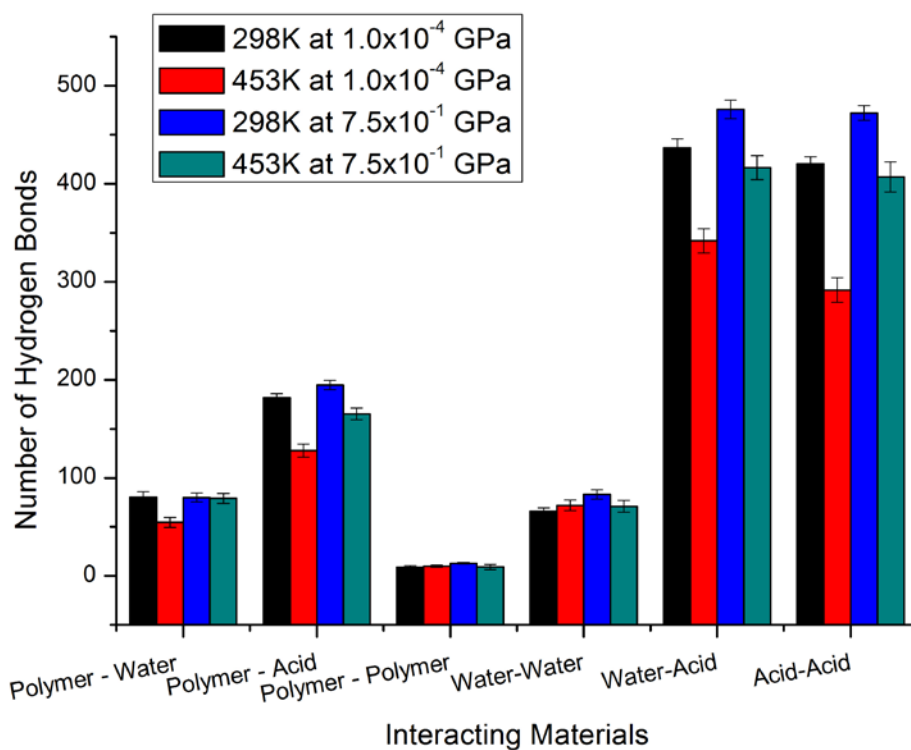
Figure 5.4: A comparison of the distribution of the number of hydrogen bonds amongst interacting materials for 298K and 453K for the 1:1.5:1.25 samples at 1.0×10^{-4} **GPa and** 7.5×10^{-1} **GPa.**

Figure 5.5 shows results for specific specie interaction for the $1:3:2.5$ samples at $298K$ and $453K$ as pressure increases. As with the $1:1.5:1.25$ sample, the number of hydrogen bonds increases with increase in pressure. Remarkably, for $1:3:2.5$ sample at $453K$ and 7.5×10^{-1} GPa the number of hydrogen bonds found exceeds what is found for the same sample at $298K$ and 1.0×10^{-4} GPa. Figure 5.6 looks at the $1:3:2.5$ at $453K$ sample and the progression of specie interaction is displayed as pressure increases. Here it becomes evident that a significant increase in

108

specie interaction occurs as the pressure is increased from 5×10^{-1} GPa to 7.5×10^{-1} GPa. The highest contributors to this growth are a result of the water – acid and acid – acid interactions.
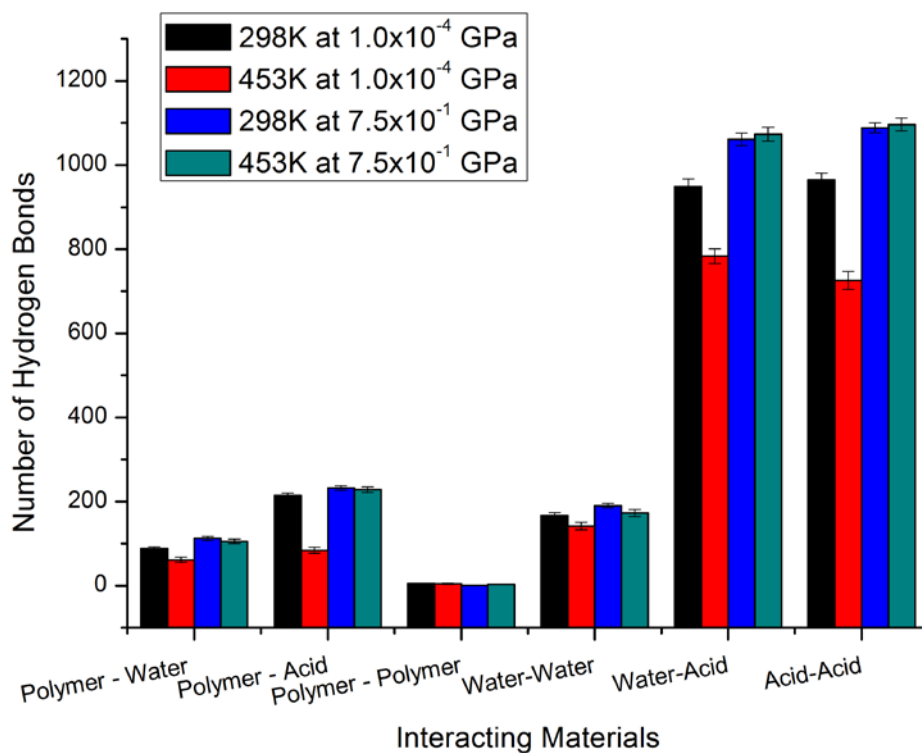
Figure 5.5: A comparison of the distribution of the number of hydrogen bonds amongst interacting materials for 298K and 453K for the 1:3:2.5 samples at 1.0×10^{-4} **GPa and** 7.5×10^{-4} **GPa.**
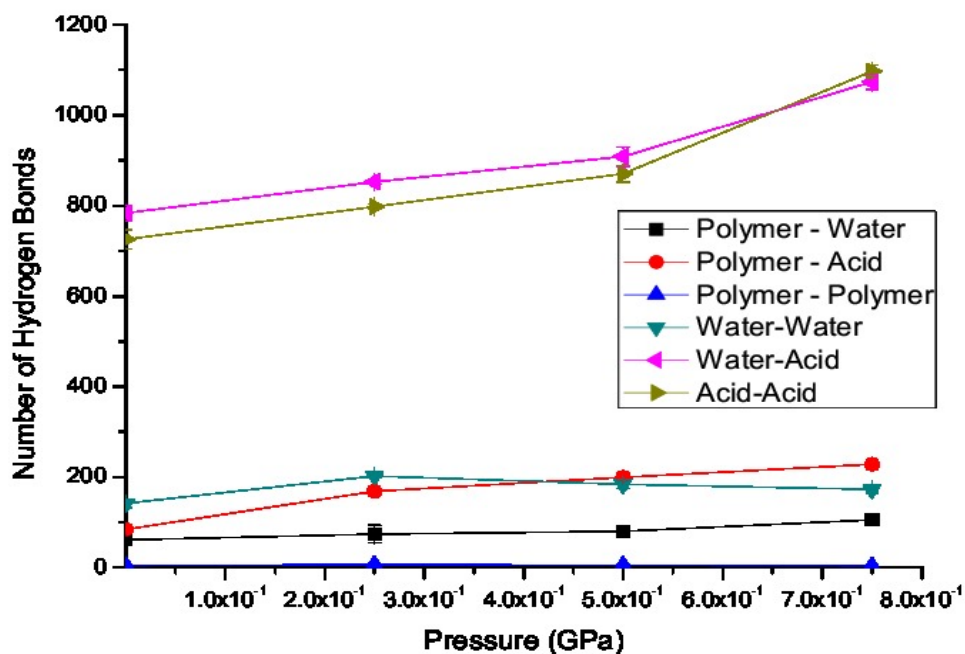
Figure 5.6: The variation in the number of hydrogen bonds for the 1:3:2.5, 453K sample, as pressure increases.

Figures 5.7 and 5.8 shows a comparison of different doping levels at $298K$ and $453K$ respectively. At both temperatures the figures depict an increase in the number of hydrogen bonds as the pressure increases. The most significant increase for both levels of doping and hydration can be found in the water-acid and acid-acid interaction. When comparing the different doping levels it is especially evident in the $453K$ sample, that increasing the levels of doping and hydration increases the number of hydrogen bonds and that by further increasing the pressure it would increase the hydrogen bonds formed between interacting species.
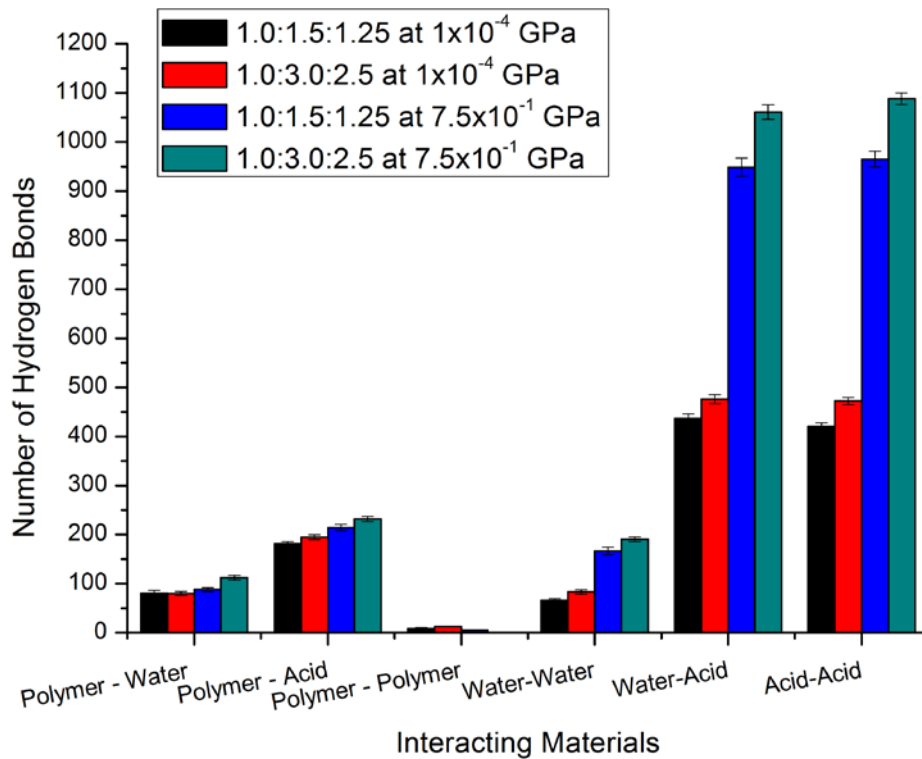
Figure 5.7: The variation in the number of hydrogen bonds with increasing phosphoric acid doping level at 298K with increasing pressure.

111
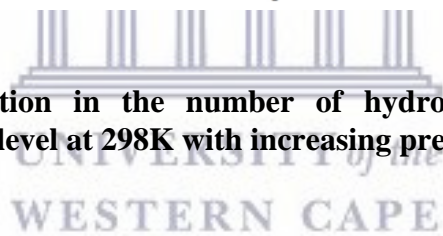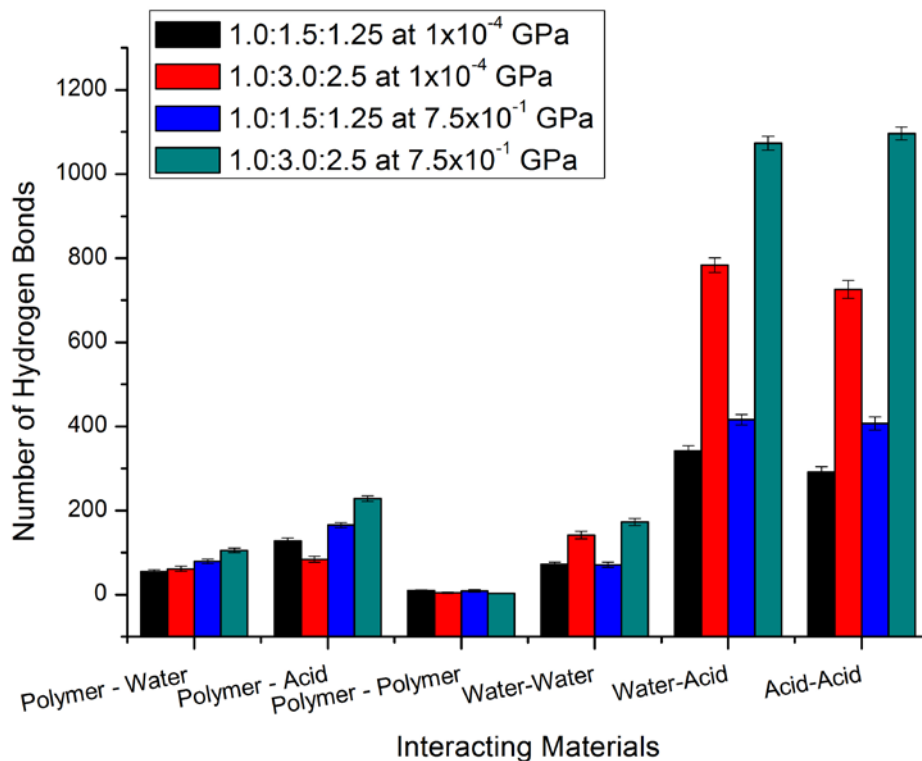
Figure 5.8: The variation in the number of hydrogen bonds with increasing phosphoric acid doping level at 453K with increasing pressure.

Overall, the results support that as pressure increases, the number of atoms forming the hydrogen bonded network increases, from this it can be deduced that proton transfer would mostly be facilitated along acid - acid and acid - water hydrogen bonds. Our results not only show that the number of hydrogen bonds involving phosphoric acid increases with phosphoric acid-doping level, which is in agreement with the work done by Li et al [14], and Na Ni [288] but that increasing the pressure would substantially increase the number of hydrogen bonds formed.

5.4.2   Radial Distribution Function

Figures 5.9 to 5.12 display the results of RDF calculations for polymer - water pairs, polymer - acid pairs and water - acid pairs respectively.

112

Figure 5.9: The radial distribution function for polymer and water donor and acceptor atoms for the 1:3:2.5, 453K sample at 1.0×10^{-4} **GPa and** 7.5×10^{-1} **GPa.**

The range of the distance considered corresponds to that of the hydrogen bond distance criterion of 2.5 Å. From figure 5.9 it becomes evident the hydrogen bond formation between the water and polymer molecules are most likely to occur through the n2a, nitrogen atom. This likelihood then further increases under the influence of an increased pressure. For the polymer and acid bond formation three options was considered, n3a – o2, n3a–o1=, shown in figure 5.10 and n2a-o2, shown in figure 5.11. In figure 5.10 the hydrogen bond formation between the polymer and acid is observed. At elevated pressures the bond formation is most likely to occur through the n3a nitrogen and o1= oxygen atoms. Notably, at normal pressure conditions the hydrogen bond formation favours the n3a nitrogen and o2 oxygen atoms and is the only pair that decreases in likelihood as pressure increases. Figure 5.11 illustrating the probability of the formation of bond formation between n2a nitrogen and o2 oxygen atoms again supports an increase in bond formation

113

as pressure increases. Figure 5.12 which shows the effects of increased pressure on the hydrogen bond formation between the acid and the water molecules. The figure shows the same trend found in figures 5.9 - 5.11 where an increase in bond formation was found as pressure increases. Specifically to the bond formation between the water and the acid molecules, the results show that this is most likely to occur between the o2* - o2 oxygen atoms.

When considering the total number of atoms meeting the hydrogen bond criteria in comparison with the total number of atoms in the sample, at $298K$ and $453K$ for the $1.0:3.0:2.5$ sample, it consists of 67% and 50% of the total system respectively. This fraction, for both temperatures, increases to 75% of the total system as pressure increases to 7.5×10^{-1} GPa. However, when looking at particular interactions the probability of two atom types a distance of approximately 2.5 Å apart, is very low and the changes with increase in pressure compared to the total number of atoms involved is exceptionally small. The trend however, can still be observed using the RDF method, and supports the results found by the hydrogen bond counting method, where pressure increase from 1.0×10^{-4} GPa to 7.5×10^{-1} GPa results in an increase of the number of hydrogen bonds. A drawback using the RDF method is that the angle criterion can not be taken into account.

114
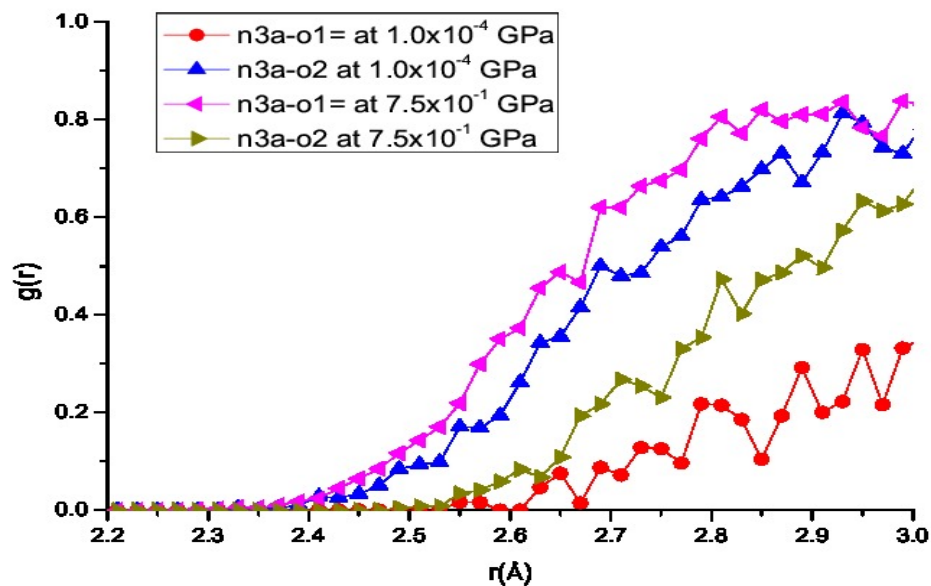
Figure 5.10: The radial distribution function for polymer donor and acid donor and acceptor atoms for the 1:3:2.5, 453K sample at 1.0×10^{-4} **GPa and** 7.5×10^{-1} **GPa.**
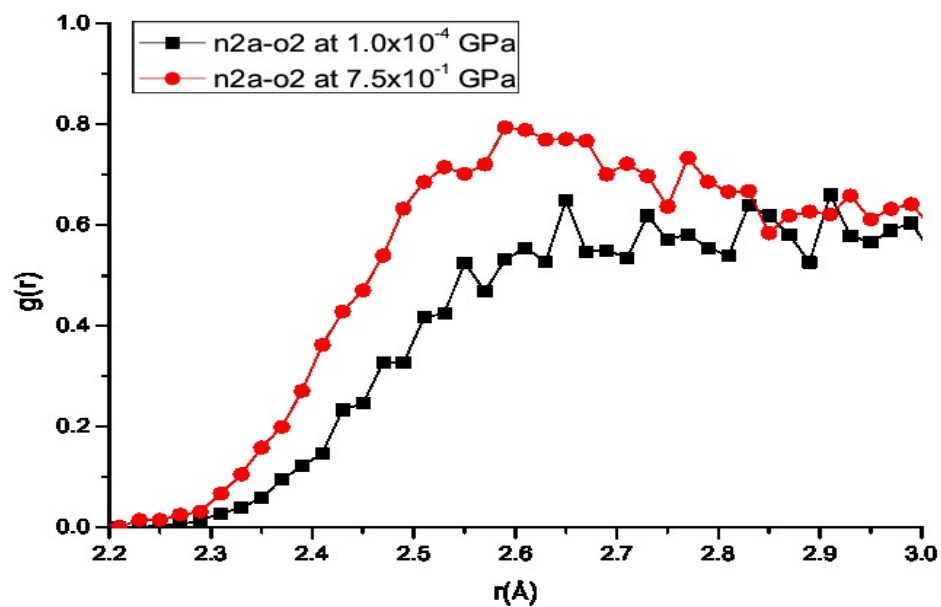
Figure 5.11: The radial distribution function for polymer acceptor and acid donor atoms for the 1:3:2.5, 453K sample at 1.0×10^{-4} **GPa and** 7.5×10^{-1} **GPa.**
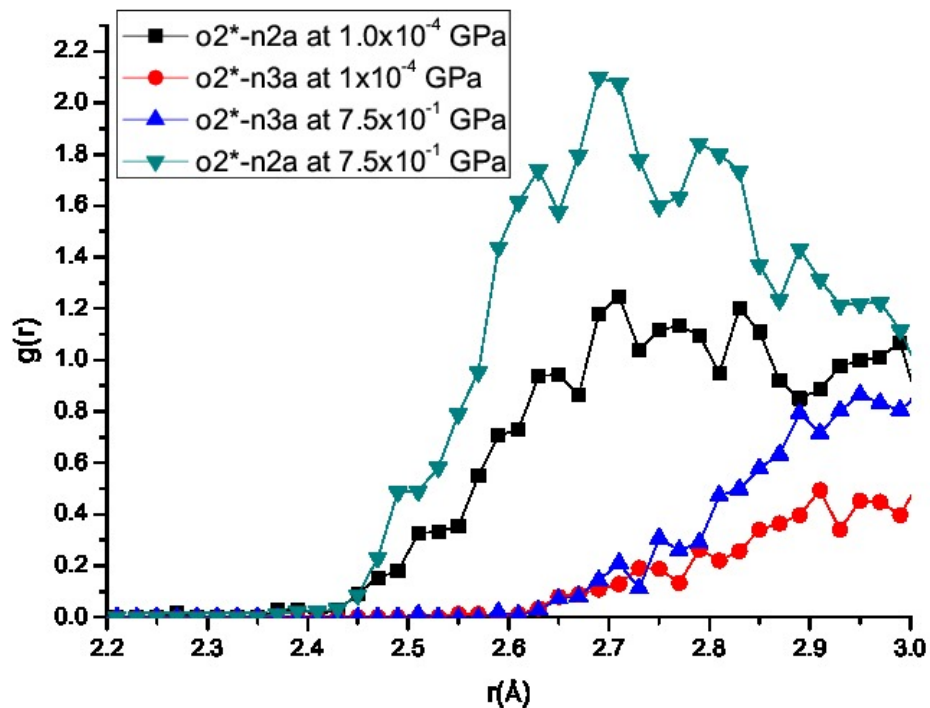
115
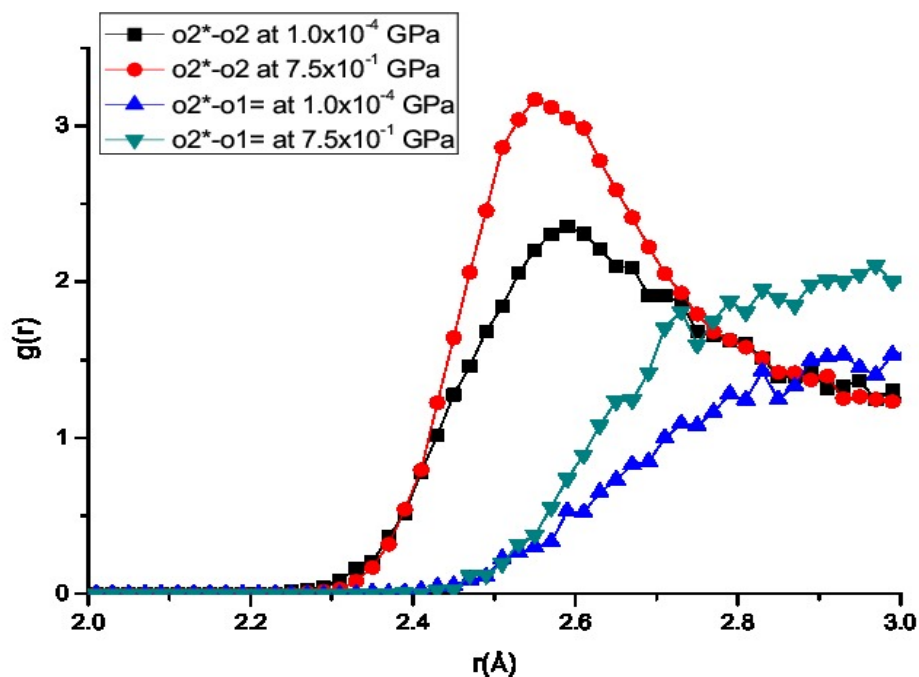
Figure 5.12: The radial distribution function for acid and water donor and acceptor atoms for the 1:3:2.5, 453K sample at 1.0×10^{-4} **GPa and** 7.5×10^{-1} **GPa.**

5.4.3 Wide Angle X-ray Diffraction

The X-ray diffraction patterns shown in figures 5.13 and 5.14 were calculated using the REFLEX module available from Materials Studio, where $\lambda = 1.5418\,\text{Å}$, Cu K$\alpha$ radiation was used for 2θ between 5 and 45° with a 0.05° step. In experimental investigations of $1:3$, ABPBI:Phosphoric acid, Wereta [6], using MSA-cast ABPBI films, reported $2\theta = 25^\circ$. Liu et al [1] report a value $2\theta = 26^\circ$ for pristine ABPBI and a corresponding d-spacing value of $3.3\,\text{Å}$. This they attribute to the stacking of ABPBI chains. Asensio et al [4], using a direct acid-cast method, found a diffraction peak at approximately 25° which appeared to consist of overlapping peaks and a new broad peak at approximately $7-8^\circ$. Li et al [14], using molecular dynamics, found at 1.0×10^{-4} GPa, the peaks for

116

$1:3:2.5$ and $1:3:0$ samples to be at $21.4°$ and $21.7°$ respectively.
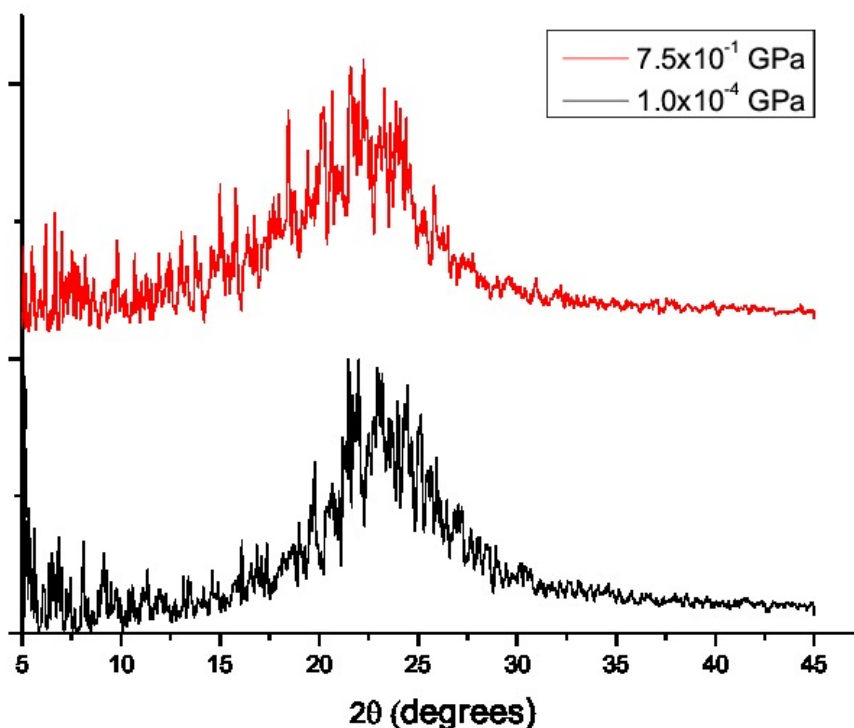
Figure 5.13: The X-ray diffraction pattern for the 1:3, 453K sample at 1.0×10^{-4} **GPa and** 7.5×10^{-1} **GPa.**

Figure 5.13 shows the X-ray diffraction pattern for the $1:3$, ABPBI:phosphoric acid sample at $453K$. We find our dominant broad peak to be in the region of $22°$ and as the pressure is increased to 7.5×10^{-1} GPa the peak is found in the same region and intensity. A broader peak was found for the doped hydrated sample, as shown in figure 5.14, and is found at approximately $20°$ for the 1.0×10^{-4} GPa sample. This peak broadening is most likely as a result of the presence of the water molecules. As the pressure increases to 7.5×10^{-1} GPa, the peak flattens out and is indicative of a changeover from crystallinity to amorphicity. From the hydrogen bond counting method, figure 5.8 in particular, the peak flattening at this high pressure could be as a result of a significant increase in the number

117

of hydrogen bonds formed between water - acid and acid - acid interaction pairs.
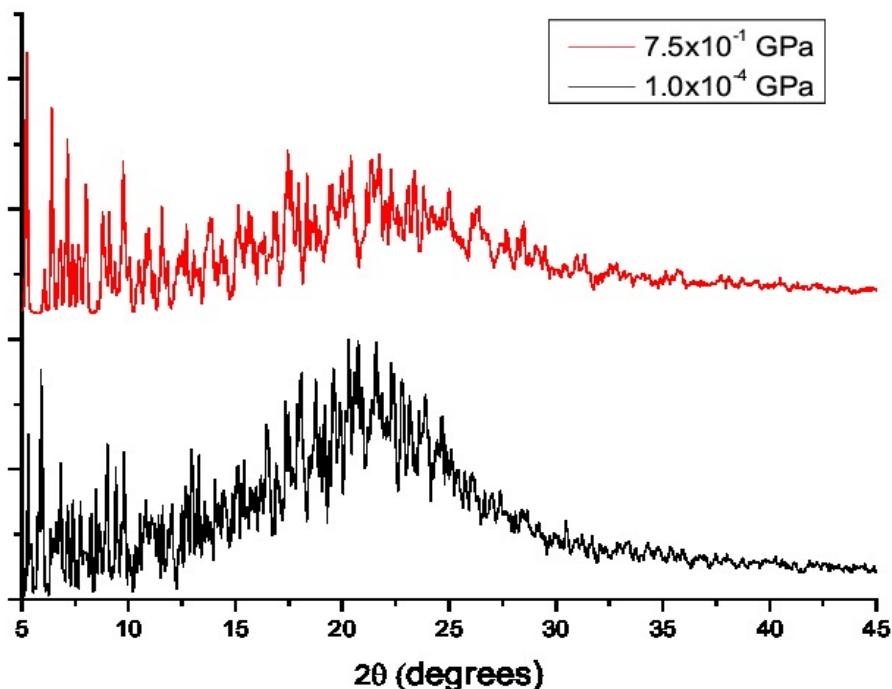
Figure 5.14: The X-ray diffraction pattern for the 1:3:2.5, 453K sample at 1.0×10^{-4}
GPa and 7.5×10^{-1} **GPa.**

5.4.4 Diffusion Coefficients

The diffusion coefficients were obtained for nitrogen, N, phosphorous, P and the oxygen, O linked to the water molecule. The nitrogen and phosphorous elements are representative of ABPBI and the phosphoric acid respectively. In table 5.2 the diffusivity of each of these three elements, N, P, O are shown to increase as the temperature increases. For nitrogen, representative of the polymer, the diffusion coefficient increases even further with increasing the pressure for the $1:1.5:1.25$ at $453K$, $1:3:2.5$ at $298K$ and $453K$ samples. For the more saturated, doped, hydrated sample ($1:3:2.5$), increasing the pressure increases the diffusion coefficient at either temperature. For the dehydrated sample, it would appear that the polymer chain would require water for further mobility.

118

Similar results were found by Brandell et al [23], in their work on the Nafion membrane; that generally high water content promotes mobility. Kreuer et al [32], in their work on molecular diffusion, proton conductivity and proton conduction mechanisms in Nafion membranes, discovered that proton conductivity is correlated with the diffusion of water for low degrees of hydration.

	D_N ($\times 10^{-8}$ $cm^2 s^{-1}$)		D_P ($\times 10^{-8}$ $cm^2 s^{-1}$)		D_O ($\times 10^{-8}$ $cm^2 s^{-1}$)	
Sample/ Pressure (GPa)	1.0×10^{-4}	7.5×10^{-1}	1.0×10^{-4}	7.5×10^{-1}	1.0×10^{-4}	7.5×10^{-1}
$1:1.5:1.25$ - $298K$	6.5	5.9	24.6	26.1	111.5	103.1
$1:1.5:1.25$ - $453K$	21.5	32.2	358.1	348.3	1189.1	1391.7
$1:3:25$ - $298K$	12.9	189.0	50.1	55.4	226.7	20.7
$1:3:2.5$ - $453K$	39.2	44.7	648.2	611.2	2143.2	2150.8
$1:3:0$ - $453K$	38.7	36.0	360.7	338.5	_	_

Table 5.2: The diffusion coefficients, D, for Nitrogen (N), Phosphorous (P) and Oxygen (O) atoms in the ABPBI polymer, phosphoric acid and water molecules samples.

For the phosphorous element, representative of the phosphoric acid, the diffusion coefficient increases with the increase in pressure only at ambient temperatures. Increasing the mobility of the phosphoric acid could contribute to the leaking of the acid from the membraneous area, which has been found to be problematic as traces have been found to be adsorbed on the active platinum catalyst sites [30]. In all other samples at $453K$ the diffusion coefficient for the phosphorous decreases. For oxygen atoms, representative of the water molecules, the diffusion coefficients for the $453K$ samples increase.

5.5   Conclusion

In this investigation the effects of high pressure on the hydrogen bond network formed by hydrated, doped poly(2,5)benzimidazole (ABPBI) were determined. Molecular dynamics was used to model the changes in the network, which provides the framework for proton

119

transfer. It was found that the number of hydrogen bonds that could form between constituents of the polymer membrane increased. The inference from the radial distribution function of hydrogen bond atom pairs support the hydrogen bond counting method and we conclude that up to $0.75\ GPa$, the pressure and the strength of the hydrogen bonded network are linearly related. The results found in this investigation supports a conclusion that the increase in pressure reduces the distance between constituents, thereby supporting the mediation of ions through segmental motions of polymers [11] and other constituents making up the polymer membrane. Reporting on the influence of high pressure on proton conductivity for doped, hydrated ABPBI has not, to be the best of our knowledge, been reported before. This study has gives insight on morphological changes and the effects on proton conductivity, as a result of high pressure, within this area. So far, limited studies were performed on the effects of pressure on the vehicular diffusion and structural changes in doped polymers. Our findings signify that the incorporation of increased pressure, improves both vehicular diffusion and the sequential movement of protons along the hydrogen-bond, which promotes greater proton conductivity.
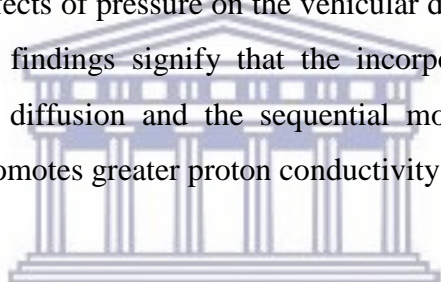
Chapter 6: Adsorption of Phosphoric Acid Anions on Platinum (111)

Abstract

The adsorption of phosphoric acid anions on the platinum (111) plane is investigated using Monte Carlo and Density Functional Theory methods. The minimum energy structure is used to generate the adsorption configurations, indicating the preferred adsorption sites. The bond lengths was found from density functional theory calculations and used to gain further insight on the structure due to adsorption. From the density functional calculations the scanning tunnelling microscopy image of the specie with the lowest adsorption energy configuration and shortest bond length was produced.

6.1   Introduction

In high temperature fuel cells phosphoric acid is considered to be an excellent doping agent. One of the disadvantages however is that the acid has been found to leak from the membrane area and adsorbed onto the platinum catalysts sites [30]. Phosphoric acid dissociates in the following manner:

$$H_3PO_4 \leftrightharpoons H_2PO_4^- + H^+ \tag{6.1}$$

$$H_2PO_4^- \leftrightharpoons HPO_4^{2-} + H^+ \tag{6.2}$$

$$HPO_4^{2-} \leftrightharpoons PO_4^{3-} + H^+ \tag{6.3}$$

Each of these species may adsorb, with or without charge transfer and the removal of a proton on the Pt surface [175]. This process is also known as deprotonation. Tanaka et al [209] studied the oxygen reduction reaction on low Pt index planes in $0.1M$ and 85%

121

H_3PO_4 using a hanging meniscus rotating disc electrode technique. The results support the conclusion that of the four low index Pt single crystal electrodes studied, the kinetic current for ORR of Pt(111) was found to have the greatest decline. It is with this in mind that the Pt(111) is considered in this investigation. He et al [210] supported this result using the method of hanging a meniscus rotating disk electrode in 0.1 M perchloric acid and in the presence of varied concentrations of H_3PO_4. Langkau and Baltruschat [176] measured impedance spectra for Pt(111) and Rh(111) electrodes in various electrolytes, where the adsorption of Cl^-, HSO_4^- and $H_2PO_4^-$ was observed. Cl^-, HSO_4^- adsorption on Pt(111) was found to occur at a very fast rates and with limited detectability. The adsorption of $H_2PO_4^-$ however, they concluded, could be described as two parallel processes, one of which could be connected to deprotonation. Arruda et al [177] looked into the competitive and site-specific nature of three other anion adsorptions on platinum using in situ X-ray absorption spectroscopy in order to gain a further understanding of the nature of poisoning on different faces/ sites of carbon supported platinum clusters. Fukuda and Aramata [178] used a potential step up method to study the kinetics of phosphate anion adsorption on Pt(111). Their investigations was performed for acidic solutions of pH 4.3 and 0.8. Experimental investigations into phosphoric acid adsorption on platinum catalysts was done by Kamat et al [179]. Kamat et al [179] concluded that because of the orientation of the adsorbed phosphate species on the platinum catalyst surface, changes in temperature, cell voltage and ageing effects are observed. Tripkoi c′ et al [180] studied the ORR mechanism on a Pt(111) surface using density functional theory calculations and found that at low overpotentials the surface was covered with a half dissociated water layer. Gisbert et al [175] studied the adsorption of phosphate anions from phosphate solutions at poly-orientated and single crystal platinum electrodes over a wide range of pH . They primarily focused on Pt(111) using cyclic voltammetry. According to Gisbert et al [175] the general consensus in single crystal literature is that the adsorption of phosphate is not related to the atomic-level surface geometry [182]. Nart [181] and Weber [211]. Markovi c′ et al [212] however found results that support the conclusion that sensitive kinetics of the ORR arise primarily due to sensitive structural adsorption of the anions.

122

Further investigations by Nart [181] and Weber [211] using cyclic voltammetry of the basal plane of different platinum electrodes in a phosphate solution discovered a significant variation in their results and analysis thereof using infrared spectroscopy, confirmed a difference in results for platinum single-crystal and polycrystalline electrodes at pH : 3.

Understanding these processes at the nanoscale is imperative to the development of atomistic engineering in catalysis. The objective of this study is to determine the resultant adsorbed phosphoric acid anions on Pt(111) and report on the activation energy, anion location and their respective bond lengths. The activation energy and bond lengths give insight to the type and strength of the bonds formed which in turn could further assist with understanding how preventative measures can be taken.

6.2 Method

The approach taken to study the adsorption of phosphoric acid anions onto platinum (111) was material modelling. The modelling techniques used were namely Monte Carlo (MC) and Density Functional Theory (DFT) methods.

6.3 Computational Procedure

The computational results in this work were obtained using software programs, Adsorption Locator, Dmol3 and CASTEP, provided by Accelrys Software incorported [41]. Adsorption Locator uses Monte Carlo searches of a samples' configurational space to identify possible adsorption configurations. COMPASS II was used as a forcefield in the energy calculations where Ewald and atom based methods were used in electrostatic and Van der Waals summations. COMPASS II is an extension to the COMPASS forcefield whereby the coverage of the number of drugs and compounds was significantly increased. COMPASS is an Ab Initio forcefield which uses the following potential to calculate atomic interaction:

123

$$U = U_b + U_\theta + U_\phi + U_\chi + U_{bb'} + U_{b\theta} + U_{b\phi} + U_{\theta\theta'} + U_{\theta\theta'\phi} + U_{elec} + U_{LJ}, \tag{6.4}$$

where U_b is the potential due to bond stretching, U_θ the potential due to bond bending where an angle θ is created between three atoms. U_ϕ considers the torsion angle, ϕ formed by four particles and its change with respect to an equilibrium position. The fourth term U_χ is a potential which considers angles formed between four particles where an inversion angle is formed. The last two potentials take into account non-bonded and Coulomb interactions. $U_{bb'} + U_{b\theta} + U_{b\phi} + U_{\theta\theta'} + U_{\theta\theta'\phi}$ are termed as cross-coupling terms between internal coordinates, important for the calculation of the vibrational frequencies and structural variations as a result of conformational changes [41].

Adsorption Locator has been used by Al-Ghamdi et al [269], Khaled et al [270], Shalabi et al [279], Tan et al [280] and Guo et al [281] to study the adsorption of various species. Dmol3, a Density Functional Theory (DFT) package, was used to perform geometry optimisation of adsorbed species. Optimised adsorbed species were then used in Adsorption Locator to determine the final adsorption configuration locations. CASTEP, a DFT package, is then used to perform geometry optimization of the resultant adsorbate-substrate configuration. All the electronic structure calculations have been carried using Generalized Gradient Approximations (GGA) and Revised Perdew Burke Ernzerhof (RPBE) functional for exchange and correlation [180]. The convergence criteria for the resultant structure was $2.231 \times 10^{-2} eV/atom$ for energy, $6.786 eV/$ Å force and 2.646×10^1 Å maximum displacement. A plane wave basis cut-off of $340.000 eV$ was then considered.

6.4 Results and Discussion

From the Adsorption Locator simulations the adsorption energies for the adsorption configurations was determined and shown in tables 6.1, 6.2 and 6.3. The number of layers

124

implemented was chosen such that the surface depth is greater than the non-bond cut-off used in the calculation. A Monte Carlo simulation technique was used to find the preferential adsorption sites on a platinum surface through finding the low-energy adsorption locations [41]. Through identifying the preferred site, geometry optimization could be performed thereafter using CASTEP.

6.4.1   Adsorption Energies

Figures 6.1, 6.2 and 6.3 illustrate the density of adsorption of $H_2PO_4^-$, HPO_4^{2-} and PO_4^- on Pt(111) respectively. The unit cell investigated in each instance spans a width of less than 10Å. A colour density scale is used to show where adsorption is greatest. Energies of adsorbate-substrate configurations parameters are shown in tables 6.1, 6.2 and 6.3. The total energy is the sum of the initial energy of the adsorbate and the resultant adsorption energy. The adsorption energy is the sum of the rigid adsorption and deformation energies. The rigid adsorption energy denotes the energy released or required by the system for adsorption of an adsorbate component that has not undergone any deformation as a result of adsorption, indicated by its associated negative or positive sign respectively [270]. When adsorbed adsorbate components are relaxed on the substrate-adsorbate configurations and one of the adsorbate components removed, the deformation energy quantifies the energy released [270]. The platinum substrate surface is taken to be zero, similarly to the work done on an iron surface by Khaled [270].

6.4.1.1 Adsorption of $H_2PO_4^-$ on Pt(111)

The initial conditions are such that the substrate has a zero energy and $H_2PO_4^-$ $-6.14eV$. The resultant configuration with the lowest adsorption energy of the seven possible configurations for $H_2PO_4^-$ was $-2.07eV$, where the negative sign indicates energy released to system. In table 6.1 the number of adsorbed configurations is indicated with respective resultant adsorbed-substrate structure energy. Figure 6.1 illustrates the

125

concentration of adsorbed species of the seven adsorbed species.
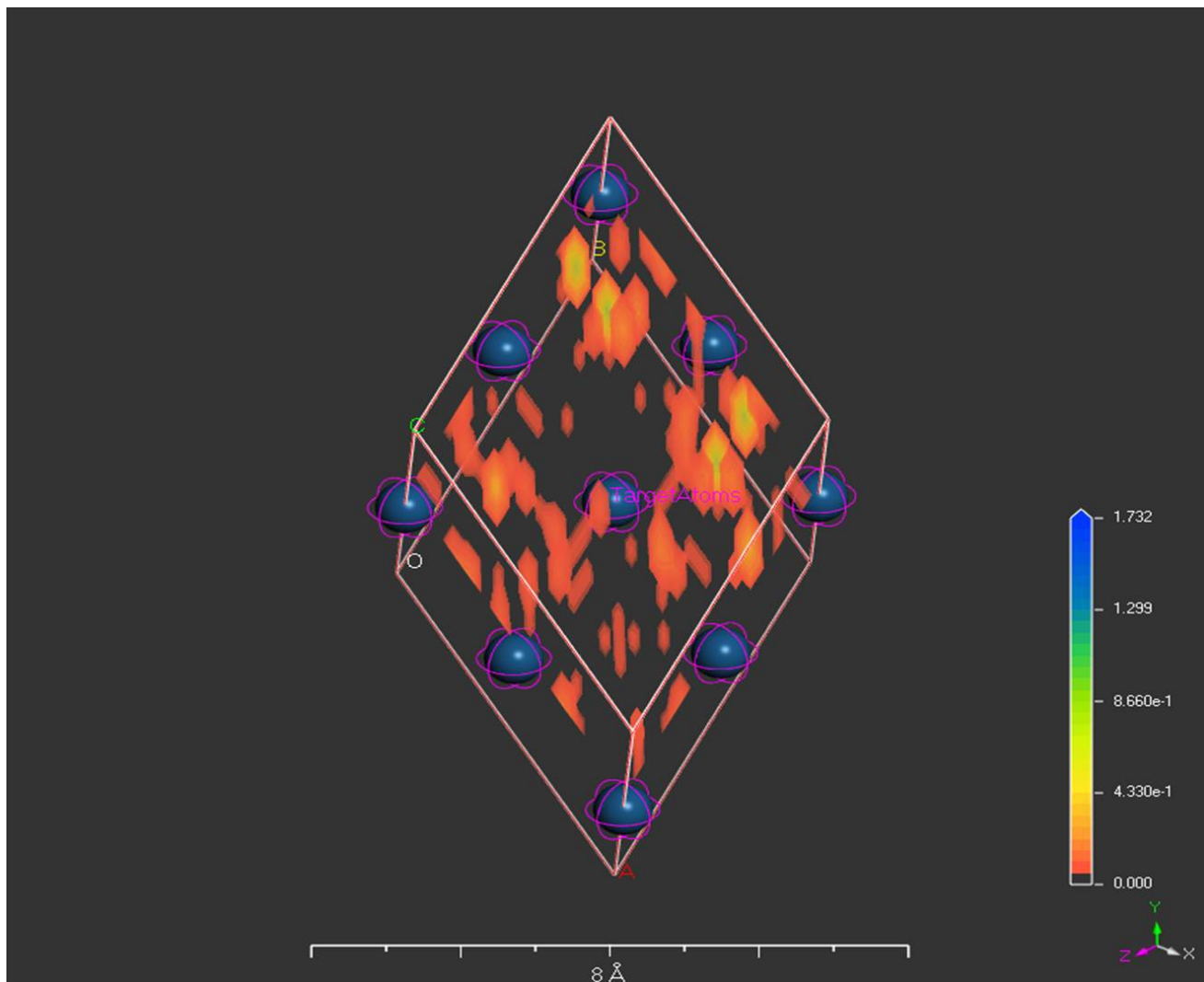
Figure 6.1: The density of the adsorption of $H_2PO_4^-$ **on Pt(111) (** g/cm^3 **)**

The density of adsorption as a result of the seven possible low energy configurations reveal hollow/bridge locations for $H_2PO_4^-$. The range for the density is [0 1.732] g/cm^3 where at the identified location a density of approximately 0.866 g/cm^3 is observed.

126

Structure Number	Total Energy of Adsorbate and Substrate (eV)	Adsorption Energy (eV)	Rigid Adsorption Energy (eV)	Deformation Energy (eV)
1	-8.21	-2.07	1.35	-3.41
2	-8.08	-1.94	1.46	-3.39
3	-8.07	-1.92	1.46	-3.39
4	-7.35	-1.21	1.69	-2.90
5	-7.34	-1.19	1.67	-2.86
6	-6.97	-0.82	1.21	-2.04
7	-6.91	-0.76	1.26	-2.02

Table 6.1: The number of adsorption configurations and corresponding energies for $H_2PO_4^-$ on Pt(111)

The rigid adsorption energy for $H_2PO_4^-$, which denotes the energy released or required by the system for adsorption of an adsorbate component that has not undergone any deformation as a result of adsorption, is positive and this suggests that deformation of the $H_2PO_4^-$ species is more likely to occur when adsorption occurs.

6.4.1.2 Adsorption of HPO_4^{2-} on Pt(111)

For the adsorption of HPO_4^{2-} the initial conditions are such that the substrate has a zero energy and $2.40eV$ for HPO_4^{2-}. For HPO_4^{2-} adsorption three locations were identified and figure 6.2 displays the concentration of adsorbed species.

127
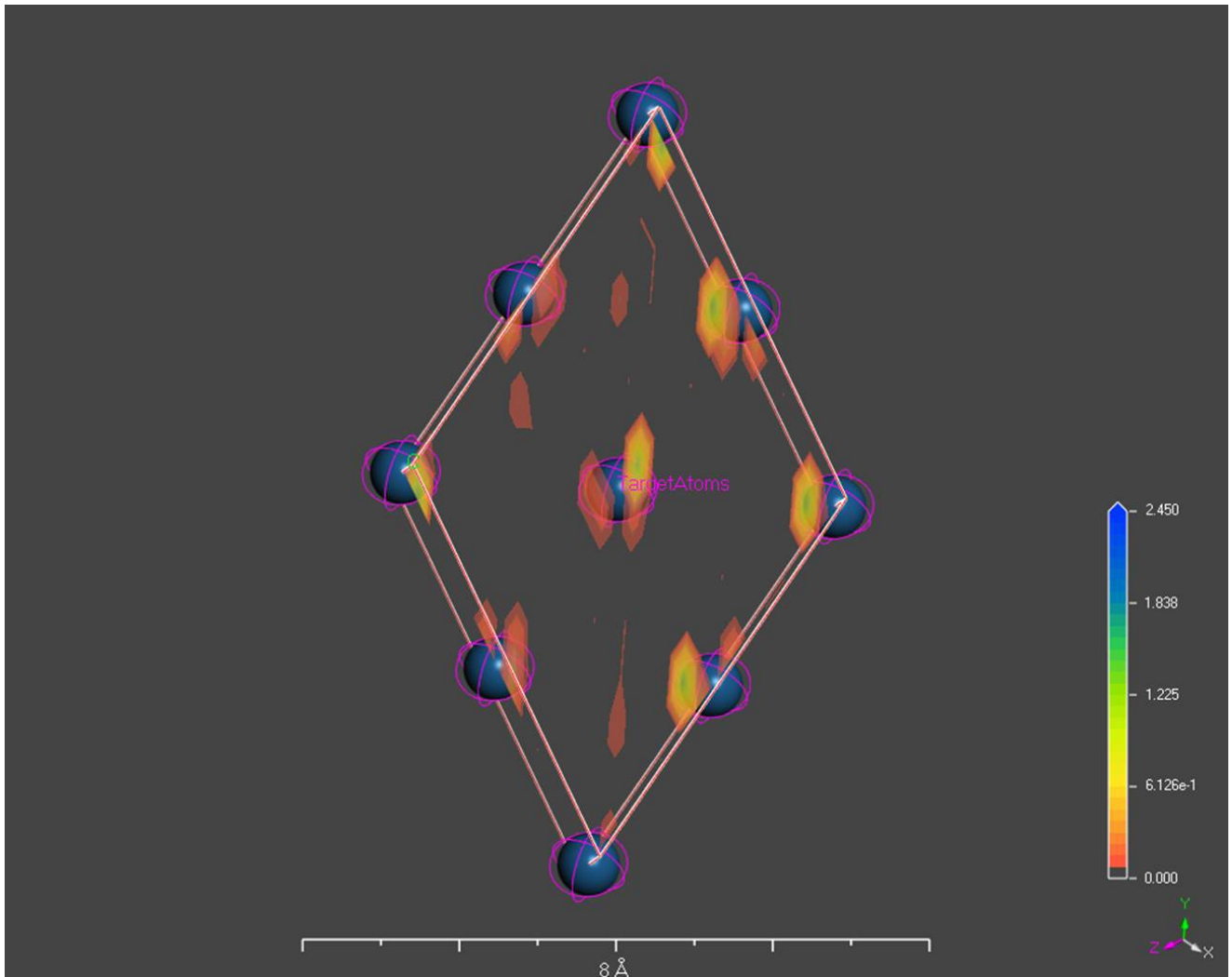
Figure 6.2: The density of the adsorption of HPO_4^{2-} **on Pt(111) (** g/cm^3 **)**

Figure 6.2 indicates that the adsorbed HPO_4^{2-} species would have an off atop orientation. The various resultant adsorption locations and respective energies are shown in table 6.2.

128

Structure Number	Total Energy of Adsorbate and Substrate (eV)	Adsorption Energy (eV)	Rigid Adsorption Energy (eV)	Deformation Energy (eV)
1	-0.79	-3.19	-1.12	-2.06
2	-0.78	-3.17	-1.11	-2.06
3	-0.64	-3.04	-0.98	-2.06

Table 4.2: The number of adsorption configurations and corresponding energies for HPO_4^{2-} on Pt(111)

For HPO_4^{2-} the lowest energy configuration has an adsorption energy of 3.19 eV. For all three possible configurations both the rigid and deformation of the species adsorbed do not require energy from the system suggesting that both rigid and deformed specie adsorption is equally likely.

6.4.1.3 Adsorption of PO_4^{3-} on Pt(111)

For the third species considered, PO_4^- the initial conditions included a substrate zero energy of zero and $10.59eV$ for the adsorbate, PO_4^-. Figure 6.3 displays the density of adsorbed species and reveals a hollow orientation and a density of approximately 2.4 g/cm^3 .

129
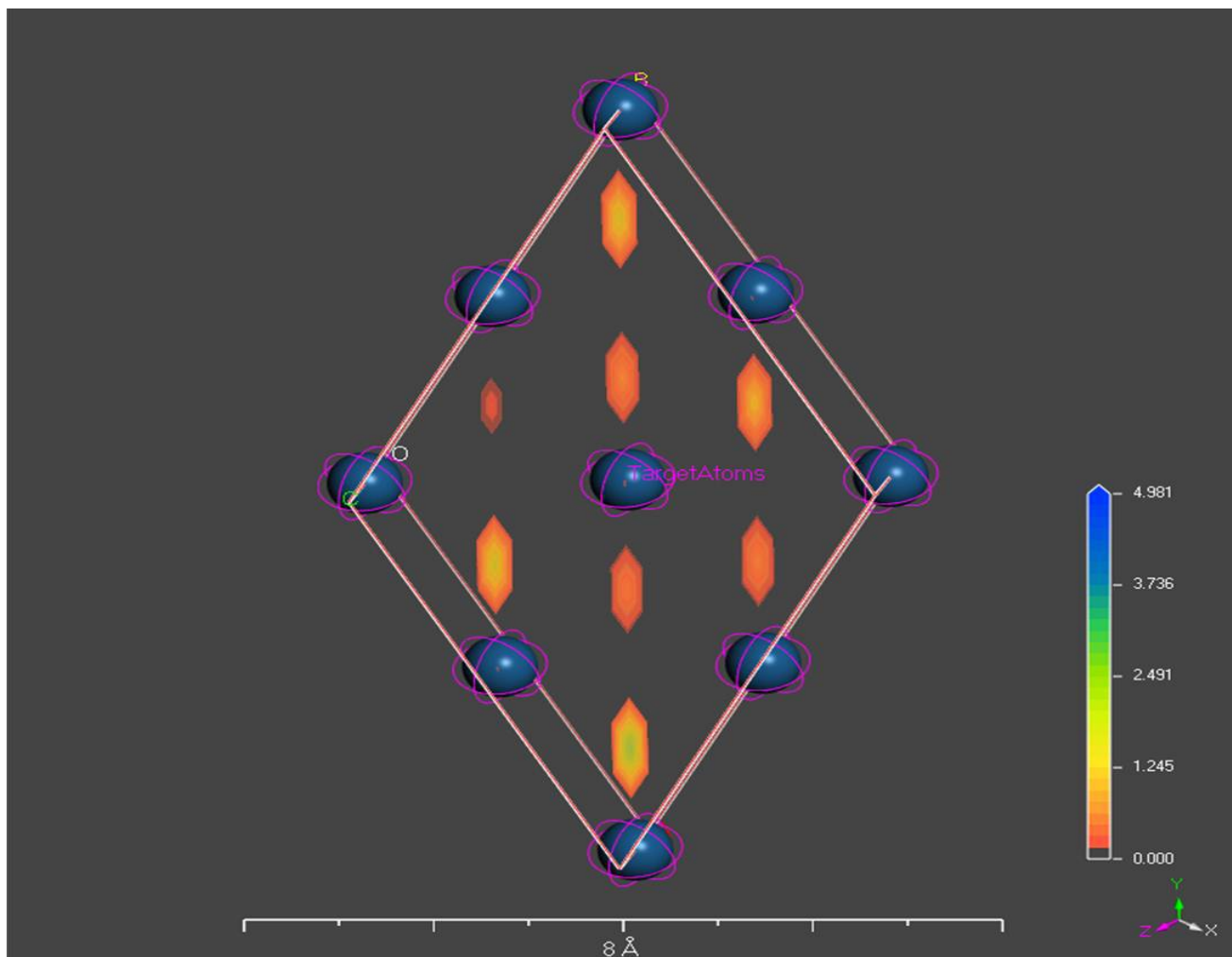
Figure 6.3: The density of the adsorption of PO_4^{3-} on Pt(111)

The resultant adsorption energies for the two adsorption configurations identified is given in table 6.3.

Structure Number	Total Energy of Adsorbate and Substrate (eV)	Adsorption Energy (eV)	Rigid Adsorption Energy (eV)	Deformation Energy (eV)
1	8.00	-2.59	-1.02	-1.56
2	8.02	-2.57	-1.01	-1.56

Table 6.3: The number of adsorption configurations and corresponding energies for PO_4^{3-} on Pt(111)

130

The lowest energy configuration has an adsorption energy of 2.59 eV. For all configurations both the rigid and deformation of the species adsorbed do not require energy. This infers that both rigid and deformed adsorption of the PO_4^{3-} specie is likely to occur.

6.4.2   Bond lengths

From the DFT calculations bond lengths of adsorbed species were determined. The fractional coordinates of atoms involved with bond formation are given in the respective tables and assists with the identification of the atoms involved with bond formation. Figures 6.4, 6.5 and 6.6 illustrate the bonds formed.

6.4.2.1 Adsorption of $H_2PO_4^-$ on Pt(111)

The fractional coordinate positions of $H_2PO_4^-$ and platinum atoms involved with bond formation is shown in the table below. This assists with spacial identification of the atoms involved with the formation of bonds. Bond formation occurs through an oxygen atom, $O4$ and the platinum atoms with which bond formation could occur is illustrated in figure 6.4.

Element	u	v	w
H1	1,060	0,223	0,546
H2	1,346	-0,024	0,563
O1	1,088	0,289	0,579
O2	1,350	0,012	0,597
O3	1,466	0,471	0,638
O4	1,354	0,149	0,517
P1	1,342	0,283	0,600
Pt3	0,009	-0,021	0,465
Pt10	0,514	-0,018	0,465
Pt24	0,517	0,487	0,466

Table 6.4: Fractional coordinates of elements participating in $H_2PO_4^-$ adsorption on Pt(111)
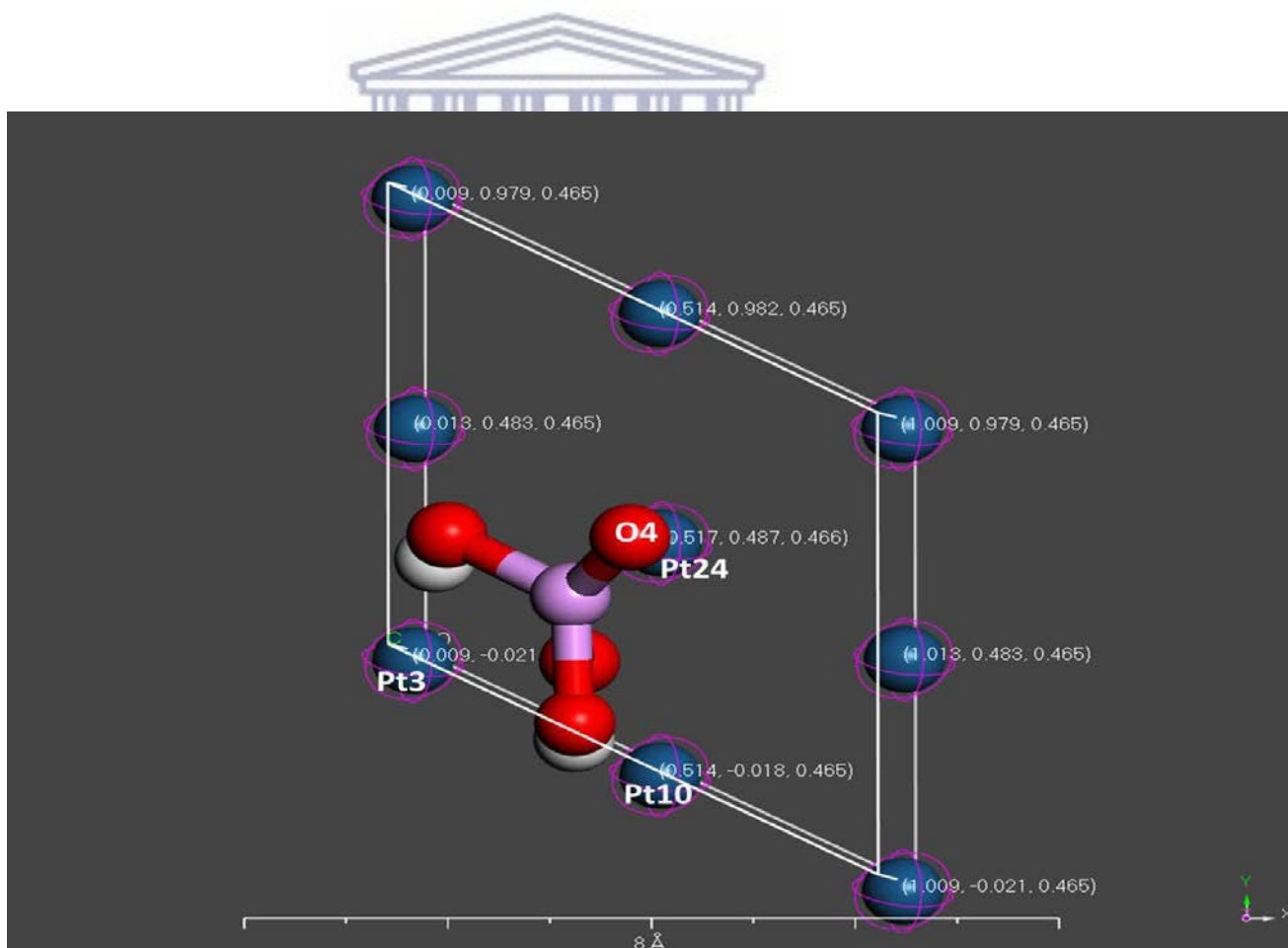
Figure 6.4: The adsorption of $H_2PO_4^-$ on Pt(111)

132

In the adsorption of $H_2PO_4^-$ bond formation most likely occurs between by the oxygen atom $O4$ and platinum atoms, $Pt3$, $Pt10$ and $Pt24$. The resultant bond lengths are given in the table below.

Elements between which a bond is formed	Bond length (Å)
O 4 – Pt 10	2.192
O 4 – Pt 24	2.219
O 4 – Pt 3	2.244

Table 6.5: Bond lengths of $H_2PO_4^-$ on Pt(111)

Figure 6.4 shows the lowest energy location for $H_2PO_4^-$. In order for bond formation to occur with $O4$ a deformation in the $H_2PO_4^-$ species would be required, which supports the results found in the adsorption calculation. Of the three possible bonds formed the bond formed by $O4$ and $Pt10$ results in the shortest bond length and as a result it would have the greatest bond energy [284].

6.4.2.2 Adsorption of HPO_4^{2-} on Pt(111)

For HPO_4^{2-} the fractional coordinate positions of atoms involved with bond formation is shown in the table below. Without the reduction of the double bond formed by the oxygen atom $O4$ and the phosphate atom to a single bond, the molecule is able to adsorb through two oxygen atoms.

133

Element	u	v	w
H1	1.303	3.046	0.567
O1	1.221	2.898	0.544
O2	1.032	2.389	0.533
O3	0.963	2.532	0.608
O4	0.700	2.578	0.539
P1	0.965	2.588	0.560
Pt3	0.023	-0.045	0.466
Pt17	0.024	0.449	0.465
Pt24	0.532	0.457	0.470

Table 6.6: The fractional coordinates of elements in HPO_4^{2-} adsorption on Pt(111)

The results from the CASTEP simulation for HPO_4^{2-} show three possibilities for adsorption. Without the transformation of the double bond into a singe bond and the deprotonation of $O1$, adsorption is likely to occur between $O2$ - $Pt17$.

134
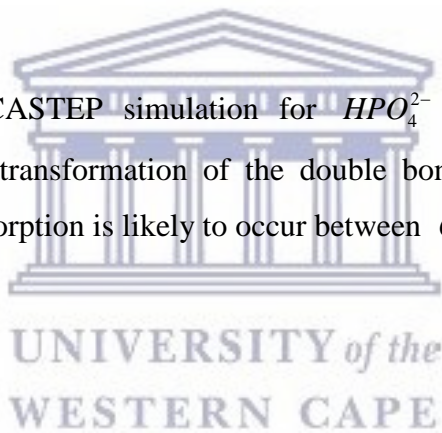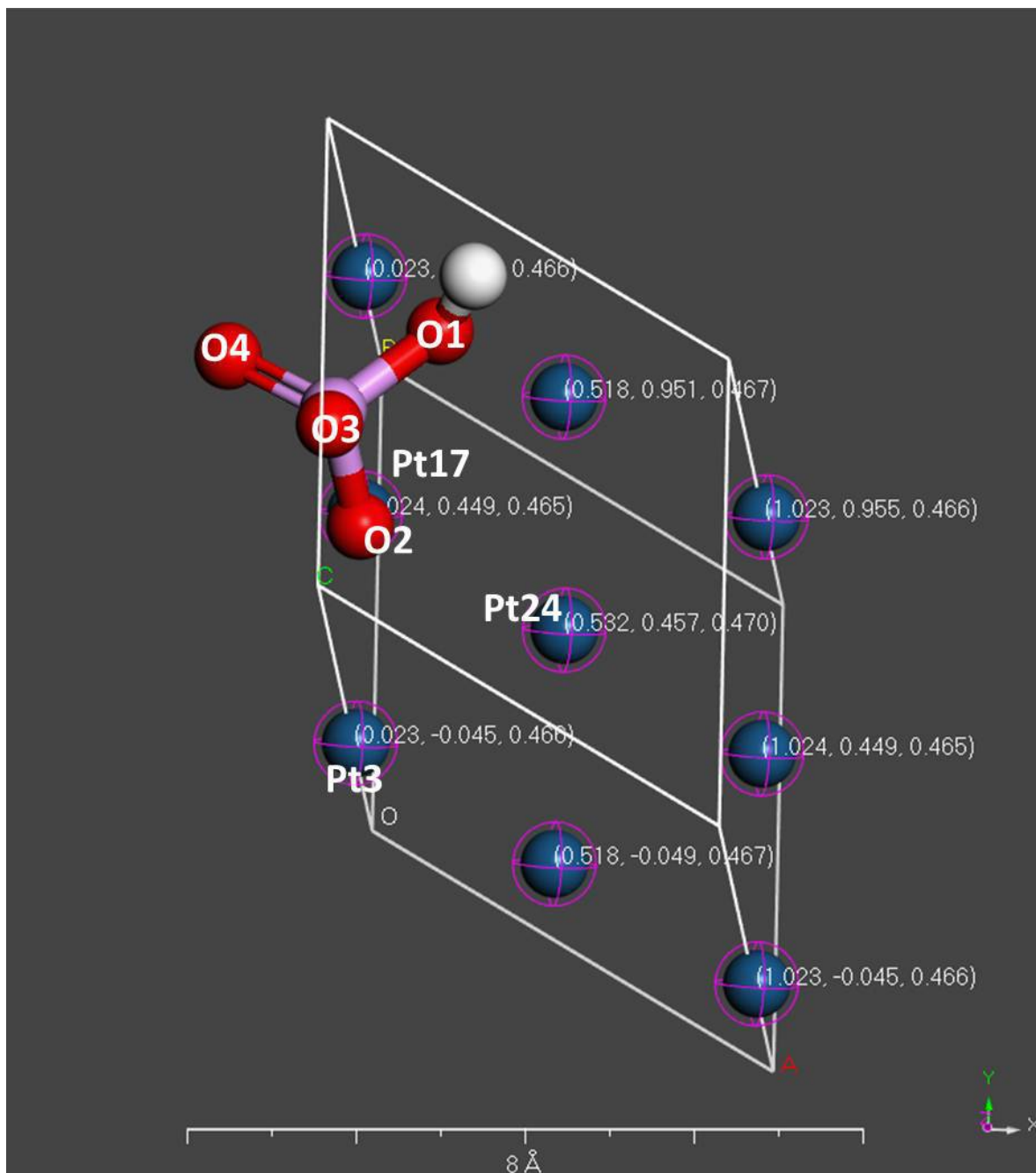
Figure 6.5: The adsorption of HPO_4^{2-} **on Pt(111)**

Elements between which a bond is formed	Bond length (Å)
O 2 – Pt 17	2.034
O 4 – Pt 24	2.221
O 1 – Pt 3	2.651

Table 6.7: Bond lengths of HPO_4^{2-} on Pt(111)

6.4.2.3 Adsorption of PO_4^{3-} on Pt(111)

In figure 6.6 the resultant PO_4^{3-} on Pt(111) configuration from the Adsorption Locator simulation is shown. PO_4^{3-} has three oxygen atoms through which bond formation can occur and the fractional positions of atoms considered is shown in the table below.

Element	u	v	w
O1	0.662	1.338	0.605
O2	0.608	1.046	0.537
O3	0.956	1.565	0.537
O4	0.433	1.391	0.536
P1	0.665	1.332	0.556
Pt10	0.504	-0.002	0.469
Pt17	0.001	0.505	0.469
Pt24	0.495	0.495	0.469

Table 6.8: Fractional coordinates of elements in PO_4^{3-} adsorption on Pt(111)

Adsorption of PO_4^{3-} can occur through, $O4$ and $Pt24$, $O3$ and $Pt17$ and $O2$ and $Pt10$. This is shown in figure 6.6 and their resultant respective bonds given in table 6.9.

136
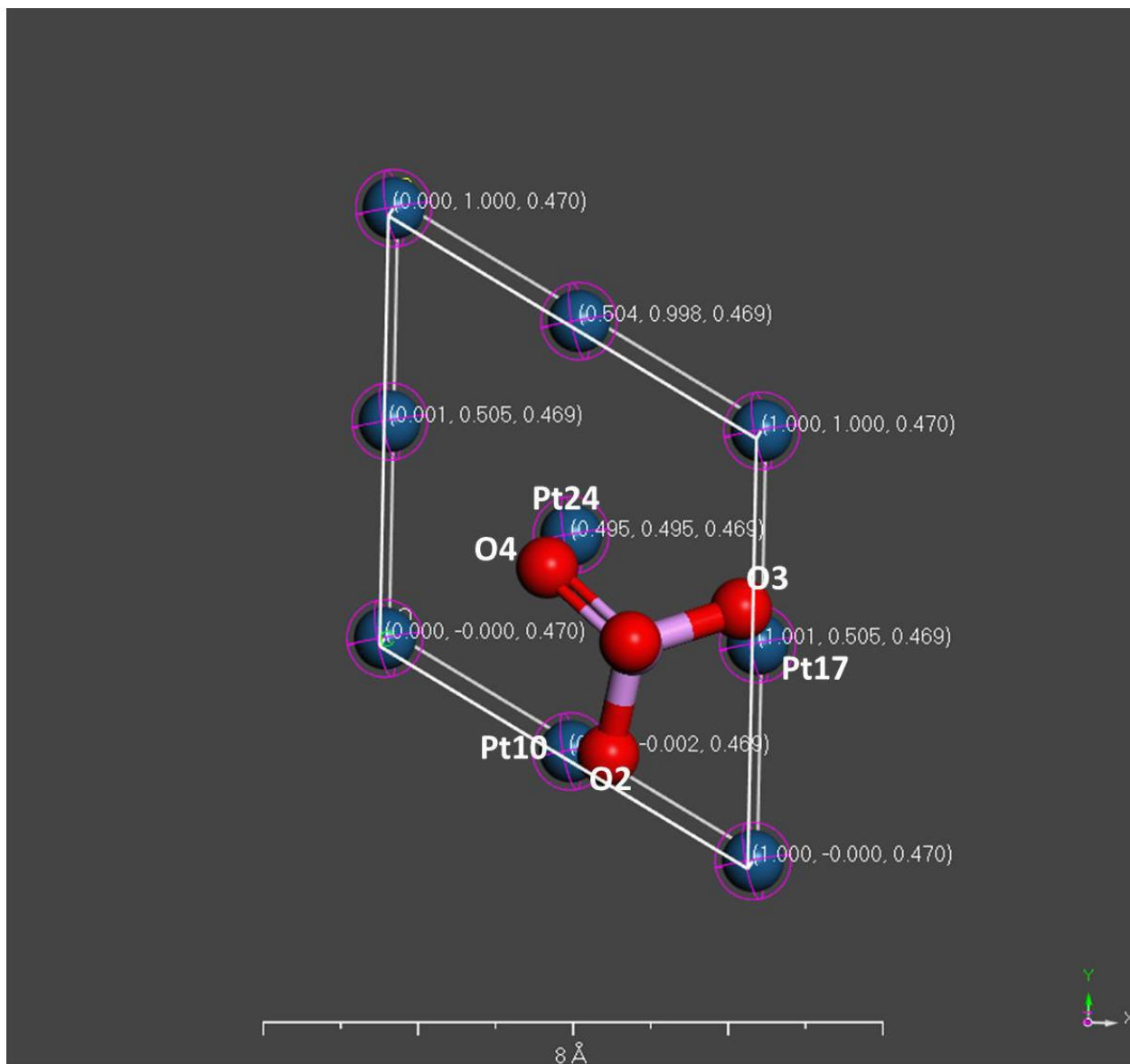
Figure 6.6: The adsorption of PO_4^{3-} **on Pt(111) bond formed by** $O1$ **and** $Pt10$

Elements between which a bond is formed	Bond length (Å)
O 4 – Pt 24	2.051
O 3 – Pt 17	2.056
O 2 – Pt 10	2.061

Table 6.9: Bond lengths of PO_4^{3-} **on Pt(111)**

137

6.4.3   Scanning Tunnelling Microscopy

The DFT package CASTEP permits the analysis of results through the production of Scanning Tunnelling Microscopy (STM) profiles. These profiles represents an isosurface of the electron density generated only by states at a certain energy away from the Fermi level [41]. The applied bias used in the generated profiles was 1V and corresponds to distance from the Fermi level. The plane considered is parallel to the y-z axis and chosen to best illustrate the bonds formed. When a positive bias is used it would correspond to imaging of empty (conduction) states, while negative bias produces images of occupied (valence) states. In CASTEP the approach does not take into account the actual geometry of the STM tip and makes use of the Tersoff-Hamman approximation [282] for tunneling transport [41]. The STM profile of HPO_4^{2-} is shown in figure 6.7 as it releases the most energy to the system. The bond formed, illustrated here corresponds with the shortest bond length, $O2--Pt17$ according to table 6.7.

138
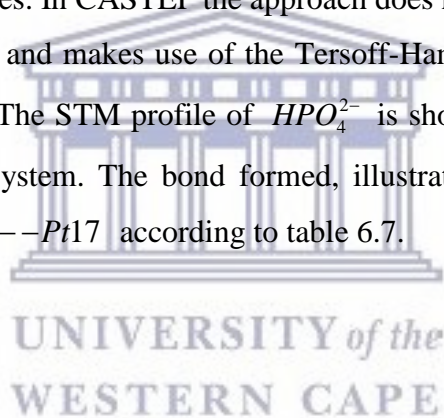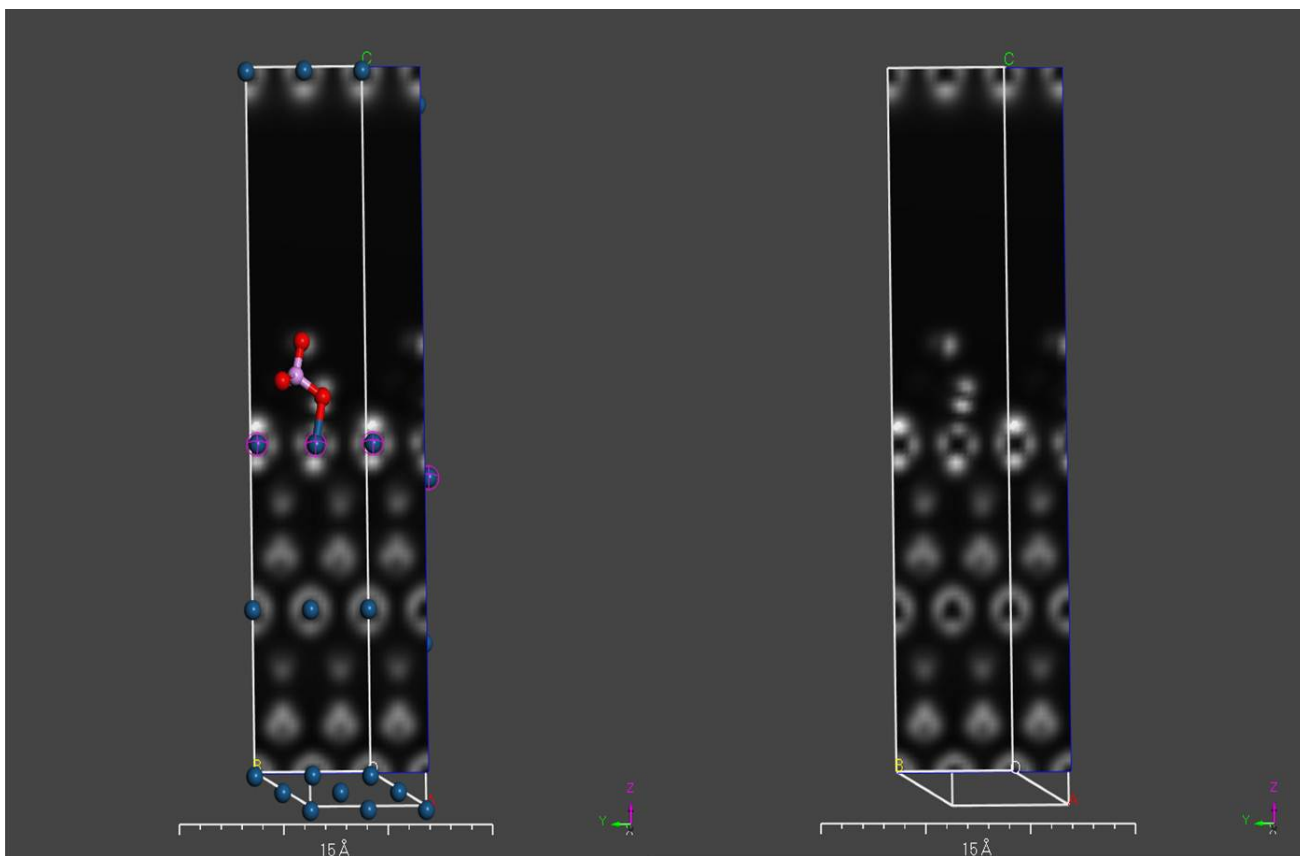
Figure 6.7: The STM profile of the adsorption of HPO_4^{2-} on Pt(111) through the $O2--Pt10$

The lighter areas in figure 6.7 indicate the empty, conduction states and corresponds to the locations of atoms.

6.5 Conclusion

In this work the adsorption of phosphoric acid anions on Pt(111) was investigated through materials modelling. The intent is to provide fundamental insight into a problem associated with the reduction in catalytic activity found in high temperature polymer electrolyte fuel cells. Monte Carlo methods was used to determine the adsorption energies of HPO_4^{2-}, PO_4^{3-} and $H_2PO_4^-$. The adsorption energies corresponding to the lowest energy configurations for each of the species was $-3.19eV$, $-2.59eV$ and $-2.07eV$ for

139

HPO_4^{2-}, PO_4^{3-} and $H_2PO_4^-$ respectively. According to the work done by Inglezakis et al [283] adsorption energies of this order corresponds to chemisorption. This in turn according to their findings results in values heat of adsorption and activation energies of greater than $0.829eV$ and $0.415eV$ respectively.

The resultant density of adsorption for each of the species revealed off atop, hollow and hollow/bridge locations for HPO_4^{2-}, PO_4^{3-} and $H_2PO_4^-$ respectively. The bond lengths for the adsorbed species is shown in respective tables and to the best of the authors knowledge have not been reported before. The scanning tunnelling microscopy profile for the bond corresponding to the shortest bond length formed for HPO_4^{2-} adsorption is shown in figure 6.7 and purpose hereof is to have a basis for comparison for future experimental work.

140

Summary of findings

Fossil fuels has for the longest time been the primary source of energy and supply has as a result of an ever increasing energy dependent population taken on strain. Consequently an urgent look at alternative energy sources has become a forefront of research and development globally. The types of alternative energy considered by a country to meet its energy needs is dependent on the capital it has available to invest into the sector, the technological advances in a particular field, its natural available resources and its topographical features. At present in South Africa, a decision has been made to increase its nuclear power generation and the number of coal power stations. With respect to renewable energy South Africa is fortunate in that it can take advantage of many options. In terms of hydroelectric energy South Africa intended to strengthen work in this field however South Africa's current water crisis places this avenue as less likely to be pursued. In South Africa solar energy resources which are amongst the highest in the world. Currently there are 33 Photovoltaic and 5 Solar thermal projects. A third renewable energy resource South Africa is able to take advantage of is wind power and it currently has 22 Renewable Energy Independent Power Producer Procurement Program onshore wind projects. Biomass, because of its ability to become available in liquid form i.e. biofuels it has transportation applications. At present South Africa is at the implementation stage of having a blended biofuel/ petrol and biofuel/ diesel products ready for the market. Wave energy, another form of harnessing energy is not a promising candidate as only a small fraction of its energy can be harnessed and therefore it is unlikely to be taken advantage of in the near future.

On an international scale fuel cells are considered a strong contender for the portable application. A key element for the catalyst layer in most fuel cells is from the platinum metal group. South Africa, rich in many minerals has more than 80% of the worlds platinum reserves. With this in mind, South Africa's intends to participating in the hydrogen fuel cell sector from a research, development and manufacturing perspective.

141

This would ensure that when it is able to make the transition to the hydrogen economy its raw minerals does not then at that later stage have to be repurchased at an exorbitant cost. This has been also identified as an employment opportunity which the country very desperately needs.

The renewable energy considered in this work is hydrogen fuel cells. A hydrogen fuel cell consists of an anode and cathode end for which each side has bipolar plates, flow channels, gas diffusion layers, catalyst layers, which are on either side of a proton exchange membrane. The fuel cell operates in the following manner; the hydrogen flows with respect to its channels, meets the electrode layer where it diffuses in the gas diffusion layer. At the anode end the hydrogen is separated into protons and electrons. The electrons travel to the carbon cloth, flow field plate, to the contact, and then to the load. The protons travel through the polymer exchange membrane to the cathode. At the cathode catalyst layer, oxygen combines with the protons to form water.

In this work the factors hindering the transportation of protons is investigated in a high temperature hydrogen fuel cell. Materials modelling is used as the tool investigate identified problems. Material modelling provides a theoretical and fundamental view on the fuel cell operation. The theoretical techniques used in this would work is discussed in chapter 2 and chapter 3 establishes the correct tools to use for molecular modelling used in the chapters that follow it. In particular it focusses on the doping agent, phosphoric acid, found within the fuel cell membrane area and establishes whether or not using an improved thermostat algorithm at the cost of computational time is worth utilizing. The improved thermostat when compared to reported to results supports the usage of this algorithm despite a small increase in computational time and reports the values for the solubility, activation energy and transportation properties of phosphoric acid.

In chapter 4 the mechanical properties of two polymers found in the membrane electrode assembly is studied. Excellent mechanical strength of these polymers would assist in stability of the overall fuel cell and assist in good proton conductivity. Using molecular

modelling these two polymers' mechanical and miscibility properties are investigated at room temperature and an operational temperature for high temperature fuel cells. Using this method of investigation to check for mixing and reporting on how both these properties are affected as a result of temperature has not been reported before. Chapter 5 looks at improving proton conductivity over the membrane area by increasing the pressure. Exploring this characteristic using material modelling too has not been reported before where results support that increasing the pressure improves the proton conductivity.

The rate at which protons are transferred is reduced when in a fuel cell the catalytic activity of the platinum is hindered. This occurs in high temperature fuel cells when the doping agent is adsorbed onto the platinum active sites. Chapter 6 looks at the atomic scale adsorption of the phosphoric acid anions onto the Pt(111) plane and reports the orientation of species, bond lengths and their respective activation energies. As far as the authors are aware these properties using Monte Carlo and density functional theory simulation methods have not been reported before.

Research output

Through the course of this thesis the author has presented aspects of the work at the following conferences and or schools

1. Research proposal - Poster presentation (Understanding Molecular Simulations 2011, Amsterdam, January 2012.)

2. The effects of pressure on the hydrogen bonded network of doped and hydrated ABPBI (preliminary results) - Poster presentation (Hydrogen and Fuel Cell conference, California, July 2013.)

3. Hydrogen Bonded Network Variation with Increase in Pressure of Doped poly(2,5-benzimidazole) Membrane - Oral presentation (5th World Hydrogen Technologies Convention, Shanghai, September 2013.)

4. The Influence of Increased Temperature on the Miscibility & Mechanical Properties of ABPBI & PTFE - Oral presentation (South African Institute of Physics national conference, South Africa, June 2015.)

At the time of submission of thesis the mechanical properties studied in chapter 4, the effects of pressure on the hydrogen bonded network investigated in chapter 5 and the final chapter, chapter 6 were in the process of publication submission and awaits the outcome thereof.

Appendices

A: Reference Tables

Symbol	Description	Atomic Unit value	Value in SI units
m_e	Electron mass	1	$9.1094 \times 10^{-31} Kg$
e	Electron charge	1	$1.6022 \times 10^{-19} C$
h	Plancks constant	2π	$6.626 \times 10^{-34} Js$
$4\pi\varepsilon_0$	Vacuum permittivity	1	$1.113 \times 10^{-10} C^2 J^{-1} m^{-1}$
c	Speed of light	137.036	$2.988 \times 10^8 ms^{-1}$

Table 10: Atomic Units [146] [145]

B: Perl Script

```
use strict;
use Getopt::Long;
use MateriasScript qw(:all);

#specify which document should be evaluated my $doc="ABPBI"; #file name
#How many frames would you like to consider? segments counted from end frame
my $FramesEvaluated=40; #$last 200ps only
my $trajectory=$Documents{"$doc.xtd"}; #specifically requesting .xtd
my $totalframes = $trajectory->NumFrames

# create a table to record results

my $StudyTable = Documents->New("Hydrogen_Bonds.std");
my $calcSheet =$StudyTable->ActiveSheet;
```

145

```perl
#Donors: ABPBI(N-n3a), H2O(O-o2*), H3PO4(O-o2)
#specimen(atom-forcefieldtype) # only pick one at a time, therefore comment
#out the donor you are not considering

my $donor="N";
my $donor="O";
my $donorffType = $doc->ForcefieldTypes("n3a");
my $donorffType = $doc->ForcefieldTypes("o2*");
my $donorffType = $doc->ForcefieldTypes("o2");

#Acceptors: ABPBI(N-n2a), H2O(O-o2*), H3PO4(O-o1=) my $acceptor="N";

my $acceptor="O";
my $acceptorffType = $doc->ForcefieldTypes("n2a");
my $acceptorffType = $doc->ForcefieldTypes("o2*");
my $acceptorffType = $doc->ForcefieldTypes("o1=");

$calcSheet->Title = "$donorffType - $acceptorffType";
$calcSheet->ColumnHeading(0)="FrameNum";
$calcSheet->ColumnHeading(1)="NumHbonds";

# initialization of variables my $totalnumhbonds=0; my $avenumhbonds=0;
#loop over all frames for (my $i=0; $i<=$FramesEvaluated; ++$i){
# Calculate hbond using the automated function available in Materials Studio by specifying
#the donor atoms you should consider
#initialize

Tools->BondCalculation->HBonds->ClearDonors;
Tools->BondCalculation->HBonds->ClearAcceptors;
Tools->BondCalculation->HBonds->AddDonor($donor);
```

146

```perl
Tools->BondCalculation->HBonds->AddAcceptor($acceptor);

$calcsheet->Cell($i,0)=$totalframes;

$trajectory->CurrentFrame = $totalframes;   #Let the current frame be the last frame

my $workingdoc-Documents->New("$trajectory.xsd");
$workingdoc->CopyFrom($trajectory);

Tools->BondCalculation->Hbonds->Calculate($workingdoc);
my $hbonds=$workingdoc->UnitCell->HydrogenBonds;
#only what's in the unit cell
my $numhbonds=0;

# In each frame do the following
foreach my $hbonds(@$hbonds){
#access the array
            if(($hbonds->Donor->ForcefieldType eq
    $donorffType)&&($hbonds->Donor->ForcefieldType eq $acceptorffType)){

                        $numhbonds++;
        }

    }
                    $total_frames--; # To look at the next frame
}

# specify unit cell

# Then since you want to specifically count the hbonds that have the specific forcefield
```

```
#criterea we'll have to have an if statement
# Now count the hbond
# print the number of hbond in frame number
# print average number hbond in all frames
```

References

[1]   Q. Liu, X. Bao , D. Rogers and S. Zou, Novel ABPBI/POSS Composite Membranes for High Temperature PEMFC Applications, ECS Transactions, 30, 25-32 (2011)

[2]   J. Durrant and J. McCammon, HBonanza: A Computer Algorithm for Molecular-Dynamics-Trajectory Hydrogen-Bond Analysis, Journal of Molecular Graphics and Modelling, 31, 5-9 (2011)

[3]   J. Asensio , S. Borrós and P. Gómez-Romero, Polymer Electrolyte Fuel Cells Based on Phosphoric Acid-Impregnated Poly(2,5-benzimidazole) Membranes, The Electrochemical Society, 151, A304-A310 (2004)

[4]   J. Asensio , S. Borrós and P. Gómez-Romero, Proton-conducting membranes based on poly(2,5-benzimidazole) (ABPBI) and phosphoric acid prepared by direct acid casting, Journal of Membrane Science, 241, 89-93 (2004)

[5]   J. Asensio , S. Borrós and P. Gómez-Romero, Recent Developments on Proton Conducting Poly(2,5-benzimidazole) (ABPBI) Membranes for High temperature Polymer Electrolyte Membrane Fuel Cells, Journal of Fuel Cells, 5, 336-343 (2005)

[6]   A. Wereta , M. Gehatia and D. Wiff, Morphological and physical property effects for solvent cast films of poly-2, 5(6) benzimidazole, Journal of Polymer Engineering and Science, 18, 204-209 (1978)

[7]   L. Diaz , G. Abuin and H. Corti, Water and phosphoric acid uptake of poly [2, 5-benzimidazole](ABPBI) membranes prepared by low and high temperature casting, Journal of Power Sources, 188, 45-50 (2009)

[8]   G. Martyna , J. Tobias and M. Klein, Constant pressure molecular dynamics algorithms, Journal of Chemical Physics, 101, 4177-4189 (1994)

[9]   M. Parrinello and A. Rahman, Polymorphic transitions in single crystals: A new molecular dynamics method, Journal of Applied Physics, 52, 7182 (1981)

[10]   J. Bendler , J. Fontanella and M. Shlesinger, Why conductivity decreases with pressure in ion-doped polymers, Fractals, 11, 93-97 (2003)

[11]   J. Fontanella , M. Wintersgill , J. Wainright , R. Savinell and M. Litt, High pressure electrical conductivity studies of acid doped polybenzimidazole, Electrochimica Acta, 43, 1289-1294 (1998)

[12]   S. Bose , T. Kuila , T. Nguyen , N. Kim , K. Lau and J. Lee, Polymer membranes for

149

high temperature proton exchange membrane fuel cell: recent advances and challenges, Progress in Polymer Science, 36, 813-843 (2011)

[13]   S. Li , J. Fried , J. Colebrook and J. Burkhardt, Molecular simulations of neat, hydrated and phosphoric acid-doped polybenzimidazoles. Part 1: Poly(2,2'-m-phenylene-5,5'-bibenzimidazole) (PBI), poly(2,5-benzimidazole)(ABPBI), and poly(p-phenylene benzobisimidazole) (PBDI), Journal of Polymer, 51, 5640-5648 (2010)

[14]   S. Li , J. Fried and J. Colebrook, Molecular simulations of poly (2, 5-benzimidazole): Effect of water concentration, phosphoric acid doping, and temperature on hydrogen bonding and vehicular diffusion, Polymer Engineering & Science, 53, 597-608 (2013)

[15]   I. Torshin , I. Weber and R. Harrison, Geometric criterea of hydrogen bonds in proteins and identification of 'bifurcated' hydrogen bonds, Journal of Protein Engineering, 15, 359-363 (2002)

[16]   K. Kreuer, Proton conductivity: materials and applications, Chemistry of Materials, 8, 610-641 (1996)

[17]   L. Yan , S. Zhu , X. Ji and W. Lu, Proton hopping in phosphoric acid solvated NAFION membrane: A molecular simulation study, The Journal of Physical Chemistry B, 111, 6357-6363 (2007)

[18]   K Kreuer , S. Paddison , E. Spohr and M. Schuster, Transport in proton conductors for fuel-cell applications: simulations, elementary reactions, and phenomenology, Chemical Reviews, 104, 4637-4678 (2004)

[19]   D. Marx, Proton transfer 200 years after von Grotthuss: Insights from Ab Initio simulations, ChemPhysChem, 7, 1848-1870 (2006)

[20]   S. Jang , V. Molinero , T. Cagin and W. Goddard, Nanophase-segregation and transport in Nafion 117 from molecular dynamics simulations: effect of monomeric sequence, Physical Chemistry B, 108, 3149-3157 (2004)

[21]   A. Venkatnathan , R. Devanathan and M. Dupuis, Atomistic simulations of hydrated Nafion and temperature effects on hydronium ion mobility, Physical Chemistry B, 111, 7234-7244 (2007)

[22]   R. Devanathan , A. Venkatnathan and M. Dupuis, Atomistic simulation of Nafion membrane: I. Effect of hydration on membrane nanostructure, Physical Chemistry B, 111, 8069-8079 (2007)

[23]   D. Brandell , J. Karo , A. Liivat and J. Thomas, Molecular dynamics studies of the

Nafion, Dow and Aciplex fuel-cell polymer membrane systems, Journal of Molecular Modeling, 13, 1039-1046 (2007)

[24] H. Sun, COMPASS: An Ab Initio Force-Field Optimized for Condensed-Phase Applications Overview with Details on Alkane and Benzene Compounds, Journal of General Physical Chemistry, 102, 7338-7364 (1998)

[25] H. Andersen, Molecular dynamics simulations at constant pressure and/or temperature, Journal of Chemical Physics, 72, 2384 (1980)

[26] D. Hofmann , L. Kuleshova and B. D'Aguanno, Theoretical simulations of proton conductivity: Basic principles for improving the proton conductor, Journal of Power Sources, 195, 7743-7750 (2010)

[27] Z. Zuo , Y. Fu and A. Manthiram, Novel blend membranes based on acid-base interactions for fuel cells, Polymers, 4, 1627-1644 (2012)

[28] H. Sun , J. Zuo , X. Wang and Y. Wan, Proton transfer reaction in poly (2 , 5 -polybenzimidazole) doping with H_3PO_4, International Journal of Hydrogen Energy, 39, 13808-13815 (2014)

[29] L. Vilč iauskas , M. Tuckerman , J. Melchior, P. Jan , G. Bester and K. Kreuer, First principles molecular dynamics study of proton dynamics and transport in phosphoric acid/imidazole (2: 1) system, Solid State Ionics, 252, 34-39 (2013)

[30] Q. He , B. Shyam , M. Nishijima , D. Ramaker and S. Mukerjee, Mitigating Phosphate Anion poisoning of Cathodic Pt/C Catalyst in Phosphoric Acid Fuel Cells, Physical Chemistry C, 117, 4877-4887, (2013)

[31] M. Eikerling , A. Kornyshev and E. Spohr, Proton-conducting polymer electrolyte membranes: water and structure in charge. In: G. Günther, S. Scherer (eds) Fuel Cells I, pp 15-54. Springer (2008)

[32] K. Kreuer , T. Dippel , W. Meyer and J. Maier (1992) Nafion Membranes: Molecular Diffusion, Proton Conductivity and Proton Conduction Mechanism. In: MRS Proceedings, pp 273. Cambridge Univ Press, (1992)

[33] Y. Maréchal, Transfers of Protons as a Third Fundamental Property of H-Bonds - Importance of Cooperative Resonance Type in Cyclic Structures. In: T. Bountis (eds) Proton Transfer in Hydrogen-Bonded Systems, pp 1-15. Springer US (1992)

[34] J. Kalivas, Adaption of Simulated Annealing to Chemical Optimization Problems. Elsevier, (1995)

[35]   M. Karttunen , I. Vattulainen and A. Lukkarinen, Novel methods in soft matter simulations. Springer Science & Business Media, (2004)

[36]   W. Gao , Z. Li and N. Sammes, An Introduction to Electronic Materials for Engineers. World Scientific, (2011)

[37]   D. Frenkel and B. Smit, Understanding Molecular Simulation from Algorithms to Applications. Academic Press, New York, (1996)

[38]   A. Hinchliffe, Molecular Modelling for Beginners, second edition. John Wiley & Sons Ltd, United Kingdom, (2008)

[39]   S. Li, Molecular Simulation of Phosphoric Acid-Doped Polybenzimidazoles as High - Temperature Proton Exchange Membranes. PhD Dissertation, University of Cincinnati College of Engineering and Applied Science (2011)

[40]   M. Di Vona, E. Sgreccia and S. Tosto, Diffusion in Solid Proton Conductors: Theoretical Aspects and Nuclear Magnetic Resonance Analysis. In P. Knauth and M. Di Vona Solid State Proton Conductors: Properties and Applications in Fuel Cells pp 25-70. John Wiley & Sons, Ltd, (2012)

[41]   Accelrys, Materials Studio Release Notes, Accelrys Software Inc, San Diego, (2011)

[42]   A. Kumar and R. Gupta, Fundamentals of Polymer Engineering, Revised and Expanded, Plastics Engineering. Taylor & Francis, (2003)

[43]   H. Moeller, Progress in Polymer Degradation and Stability Research. Nova Science Publishers, (2007)

[44]   P. Gode, G. Lindbergh and G. Sundholm, In-situ measurements of gas permeability in fuel cell membranes using a cylindrical microelectrode, Journal of Electroanalytical Chemistry, 518, 2, 115-122, (2002)

[45]   A. Kelly, Concise Encyclopedia of Composite Materials, Advances in Materials Sciences and Engineering. Elsevier Science, (2012)

[46] , C. Daniels, Polymers: Structure and Properties. CDC Press (1989)

[47]   R. Stokes and D. Evans, Fundamentals of Interfacial Engineering. John Wiley & Sons, (1997)

[48]   M. Alger, Polymer Science Dictionary. Springer Science and Business Media, (1997)

[49]   T. Helminiak , W. Hwang , D. Wiff , C. Benner and G. Price, Molecular level

152

composite of PBT/ABPBI: phase relationships, processing and properties, AIR FORCE WRIGHT AERONAUTICAL LABORATORIES, AFWAL-TR-82-4039, (1982)

[50]   Q. Liu , X. Bao , D. Rogers and A. Zou, Novel ABPBI/POSS Composite Membranes for High Temperature PEMFC Applications, ECS Transactions, (2011)

[51]   T. Cagin, Mechanical Response of high Perfomrance Polymers: ABPBO, ABPBI and ABPBT, Materials Research Society Symposium, 291, 321-324, (1993)

[52]   M. Ashby, Materials Selection in Mechanical Design. Elsevier Science, (2010)

[53]   C. Hansen, Hansen Solubility Parameters: A User's Handbook, Second Edition. CRC Press, (2007)

[54]   J. Asensio and P. Gomez-Romero, Recent developments on proton conducting poly (2, 5-benzimidazole)(ABPBI) membranes for high temperature polymer electrolyte membrane fuel cells, Fuel Cells, 5, 3, 336-343, (2005)

[55]   J. Asensio , S. Borrós and P. Gómez-Romero, Enhanced conductivity in polyanion-containing polybenzimidazoles. Improved materials for proton-exchange membranes and PEM fuel cells, Electrochemistry Communications, 5, 11, 967-972, (2003)

[56]   K. Chee, Temperature Dependence of Solubility Parameters of Polymers, Maylaysian Journal of Chemistry, 7, 1, 051-061, (2005)

[57]   X. Chen , C. Yuan , C. Wong and G. Zhang, Molecular modeling of temperature dependence of solubility parameters for amorphous polymers, Journal of Molecular Modeling, 18, 2333-2341, (2012)

[58]   C. Carraher and R. Seymour, Structure-Property Relationships in Polymers. Springer US, (2012)

[59]   L. Sperling, Introduction to Physical Polymer Science. John Wiley and Sons, (2005)

[60]   J. Nicholson, The Chemistry of Polymers, Royal Society of Chemistry, (2012)

[61]   W. Soboyejo, Mechanical Properties of Engineered Materials. CRC Press, (2002)

[62]   J. Mark, Physical Properties of Polymers Handbook Second Edition, Solubility Parameters, 289-304. Springer Science and Business Media, (2007)

[63]   J. Hildebrand, Solubility. 111. Relative values of internal pressures and their practical application, American Chemical Society, 41, 1067-1080, (1919)

[64]   J. Hildebrand and R. Scott, The solubility of nonelectrolytes, Reinhold Pub. Corp,

153

(1950)

[65]   J. Hildebrand, SOLUBILITY, American Chemical Society, 38, 1452-1473, (1916)

[66]   G. Scatchard, Equilibria in non-electrolyte solution in relation to the vapor pressures and densities of components, Chem Rev, 8, 321-333, (1931)

[67]   S. Nosé, A molecular dynamics method for simulations in the canonical ensemble, Molecular Physics, 52, 2, 255-268, (1984)

[68]   S. Nosé, A unified formulation of the constant temperature molecular dynamics methods, The Journal of Chemical Physics, 81, 1, 511-519, (1984)

[69]   H. Berendsen, J. Postma, W. van Gunsteren, A. DiNola and J. R. Haak, Molecular dynamics with coupling to an external bath, Chemical Physics, 81, 3684, (1984)

[70]   J. Drobny, Fluoroplastics, rapra TECHNOLOGY, Review Reports, 16, 4, (2005)

[71]   J. Drobny, Technology of Fluoropolymers. CRC Press, (2014)

[72]   Q. Li, J. Jensen, R. Savinell and N. Bjerrum, High temperature proton exchange membranes based on polybenzimidazoles for fuel cells, Progress in Polymer Science, 34, 449-477, (2009)

[73]   P. Corbo, F. Migliardini and O. Veneri, Hydrogen Fuel Cells for Road Vehicles, Green Energy and Technology. Springer London, (2011)

[74]   S. Basu, Recent Trends in Fuel Cell Science and Technology. Springer, (2007)

[75]   A. Spieser , B. Leeflang , L. Kroon-Batenburg and J. Kroon, A Force Field for Phosphoric Acid: Comparison of Simulated with Experimental Data in the Solid and Liquid State, Phys. Chem. A, 104, 7333-7338, (2000)

[76]   M. More, S. Pahari, S. Roy and A. Venkatnathan, Characterization of the structures and dynamics of phosphoric acid doped benzimidazole mixtures: a molecular dynamics study, Mol Model, 19, 109-118, (2013)

[77]   P. Hünenberger, Thermostat algorithms for molecular dynamics simulations, Advanced computer simulation. Springer, 105-149, (2005)

[78]   P. Hünenberger, Thermostat Algorithms for Molecular Dynamics Simulations, Advances in Polymer Science, 173, 105-149, (2005)

[79]   R. Tromp, A neutron diffraction and computer modelling study of the interatomic structure of phosphoric acid, Chemical Physics, 110, 4, 2145- 2150, (1999)

[80]   S. Nosé, Constant temperature molecular dynamics methods, Progress of Theoretical Physics Supplement, 103, 1-46, (1991)

[81]   W. Hoover, Canonical dynamics: equilibrium phase-space distributions, Physical Review A, APS 31, 3, 1695, (1985)

[82]   G. Mansoori, Principles of Nanotechnology: Molecular-Based Study of Condensed Matter in Small Systems. World Scientific, (2005)

[83]   M. Allen and D. Tildesley, Computer Simulation of Liquids. Oxford University Press, (1987)

[84]   J. Burke, Solubility Parameters: Theory and Application, The Book and Paper Group ANNUAL, 3, 105-149, (1984)

[85]   E. Anslyn and D. Dougherty, Modern Physical Organic Chemistry. University of Science Books, (2006)

[86]   S. Arrhenius, Über die Dissociationswärme und den Einfluss der Temperatur auf den Dissociationsgrad der Elektrolyte, Wilhelm Engelmann, (1889)

[87]   D. Ernst and J. Köhler, Measuring a diffusion coefficient by single-particle tracking: statistical analysis of experimental mean squared displacement curves, Physical Chemistry Chemical Physics, 15, 845-849, (2013)

[88]   Y. Aihara, A. Sonai, M. Hattori and K. Hayamizu, Ion Conduction Mechanisms and Thermal Properties of Hydrated and Anhydrous Phosphoric Acids Studied with ^{1}H, ^{2}H and ^{31}P NMR, J. Phys. Chem. B, 110, 24999-25006, (2006)

[89]   B. Bharat, Springer Hand Book of Nanotechnology, Second Edition. Springer, (2007)

[90]   D. MacDonald and J. Boyack, Density, Electrical Conductivity, and Vapor Pressure of Concentrated Phosphoric Acid, Chemical and Engineering Data, 380-384, (1969)

[91]   E. Egan and B. Luff, Measurements at 15° to 80° C - Density of Aqueous Solutions of Phosphoric Acid, Industrial & Engineering Chemistry, 47, 1280-1281, (1955)

[92]   B. Pfrommer, M. Côté, S. Louie and M. Cohen, Relaxation of crystals with the quasi-Newton method, Journal of Computational Physics, 131, 1, 233-240, (1997)

[93]   M. Ferrario, G. Ciccotti, K. Binder, Ettore Majorana Foundation and Centre for Scientific Culture, Computer Simulations in Condensed Matter: From Materials to

Chemical Biology, Computer Simulations in Condensed Matter Systems: From Materials to Chemical Biology. Springer, (2006)

[94]   H. Ibach and H. Lüth, Solid-State Physics: An Introduction to Principles of Materials Science, In: Advanced texts in physics. Springer Berlin Heidelberg, (2009)

[95]   M. Steinhauser, Computer Simulation in Physics and Engineering. De Gruyter, (2012)

[96]   S. Salinas, Introduction to Statistical Physics, Graduate Texts in Contemporary Physics. Springer, (2001)

[97]   W. Davis, Physical Chemistry: A Modern Introduction, Second Edition. CRC Press, (2001)

[98]   A. Constantinescu and A. Korsunsky, Elasticity with Mathematica : An Introduction to Continuum Mechanics and Linear Elasticity, Engineering Pro collection. Cambridge University Press (2007)

[99]   R. Soutas-Little, Elasticity, Dover Books on Physics Series. Dover Publications, (1999)

[100]   A. Ragab and S. Bayoumi, Engineering Solid Mechanics: Fundamentals and Applications. Taylor & Francis, (1998)

[101]   E. Gopal, Statistical Mechanics and Properties of Matter: Theory and Applications. Ellis Horwood, (1974)

[102]   J. Seddon and J. Gale, Thermodynamics and Statistical Mechanics, Tutorial chemistry texts. Royal Society of Chemistry (2001)

[103]   H. Berendsen, Simulating the Physical World: Hierarchical Modeling from Quantum Mechanics to Fluid Dynamics. Cambridge University Press (2007)

[104]   R. Pathria and P. Beale, Statistical Mechanics. Elsevier Science (2011)

[105]   F. Mandl, Statistical Physics, Manchester Physics Series. Wiley (2013)

[106]   D. Yoshioka, Statistical Physics: An Introduction. Springer Science & Business Media, (2007)

[107]   R. Martin, Electronic Structure: Basic Theory and Practical Methods. Cambridge University Press (2004)

[108]   C. Roothaan, New Developments in Molecular Orbital Theory, Reviews of Modern

Physics, 23, 2, 69-89, (1951)

[109]   K. Ramachandran , G. Deepa and K. Namboori, Computational Chemistry and Molecular Modeling: Principles and Applications. Springer Science & Business Media, (2008)

[110]   J. Bort and J. Rusca, Theoretical and Computational Chemistry: Foundations, Methods and Techniques. Universitat Jaume I, (2007)

[111]   P. Hedvig, Experimental Quantum chemistry. Elsevier Science (2012)

[112]   S. Goudsmit and G. Uhlenbeck, Over Het Roteerende Electron En de Structuur der Spectra, Physica, 6, 273-290, (1929)

[113]   H. Kuhn, H. Försterling and D. Waldeck, Principles of Physical Chemistry. Wiley, (2009)

[114]   M. Tuckerman, Statistical Mechanics and Molecular Simulations. Oxford University Press, (2008)

[115]   N. Metropolis, A. Rosenbluth, M. Rosenbluth, A. Teller and E. Teller, Equation of State Calculations by Fast Computing Machines, The Journal of Chemical Physics, 21, 6, 1087-1092, (1953)

[116]   S. Kirkpatrick, C. Gelatt and M. Vecchi, Optimization by Simulated Annealing, Science, 220, 4598, 671-680, (1983)

[117]   V. Č erný, Thermodynamical approach to the traveling salesman problem: An efficient simulation algorithm, Journal of Optimization Theory and Applications, 45, 1, 41-51, (1985)

[118]   A. Wymyslowski, N. Iwamoto, M. Yuen and H. Fan, Molecular Modeling and Multiscaling Issues for Electronic Material Applications, Second Volume. Springer (2014)

[119]   B. Hammer, L. Hansen and J. Nørskov, Improved adsorption energetics within density-functional theory using revised Perdew-Burke-Ernzerhof functionals, Physical Review B Condensed Matter, 59, 11, 7413-7421, (1999)

[120]   J. Perdew, K. Burke and M. Ernzerhof, Generalized Gradient Approximation Made Simple, Physical Review Letters, 77, 18, 3865-3868, (1996)

[121]   J. Perdew, J. Chevary, S. Vosko, K. Jackson, M. Pederson, D. Singh and C. Fiolhais, Atoms, molecules, solids, and surfaces: Applications of the generalized gradient approximation for exchange and correlation, Physical Review B, 46, 11, 6671-6687,

(1992)

[122]   D. Ceperley and B. Alder, Ground State of the Electron Gas by a Stochastic Method, Physical Review Letters, 45, 7, 566-569, (1980)

[123]   J. Perdew and A. Zunger, Self-interaction correction to density-functional approximations for many-electron systems, Physical Review B, 23, 10, 5048-5079, (1981)

[124]   M. Payne, M. Teter, D. Allan, T. Arias and J. Joannopoulos, Iterative minimization techniques for *Ab Initio* total-energy calculations: molecular dynamics and conjugate gradients, Reviews of Modern Physics., 64, 4, 1045-1097, (1992)

[125]   U. von Barth and L. Hedin, A local exchange-correlation potential for the spin polarized case. i, Journal of Physics C: Solid State Physics, 5, 13, 1629, (1972)

[126]   O. Gunnarsson and B. Lundqvist, Exchange and correlation in atoms, molecules, and solids by the spin-density-functional formalism, Physical Review B, 13, 10, 4274-4298, (1976)

[127]   J. Perdew and Y. Wang, Accurate and simple analytic representation of the electron-gas correlation energy, Physical Review B, 45, 23, 13244-13249, (1992)

[128]   J. Slater, A Simplification of the Hartree-Fock Method, Phys. Rev., 81, 3, 385-390, (1951)

[129]   L. Hedin and B. Lundqvist, Explicit local exchange-correlation potentials, Journal of Physics C: Solid State Physics, 4, 14, 2064, (1971)

[130]   M. Levy, Universal variational functionals of electron densities, first-order density matrices, and natural spin-orbitals and solution of the v-representability problem, Proceedings of the National Academy of Sciences, 76, 12, 6062-6065, (1979)

[131]   W. Kohn and L. Sham, Self-Consistent Equations Including Exchange and Correlation Effects, Physical Review, 140, 4A, A1133-A1138, (1965)

[132]   J. Slater, A Generalized Self-Consistent Field Method, Physical Review, 91, 3, 528-530, (1953)

[133]   C. Sherrill, An introduction to Hartree-Fock molecular orbital theory. School of Chemistry and Biochemistry Georgia Institute of Technology, (2000)

[134]   S. Zumdahl, Chemical Principles. Cengage Learning, (2007)

[135]   S. Sharma, Atomic And Nuclear Physics. Pearson Education India, (2008)

[136]   F. Wang, Physics with MAPLE: The Computer Algebra Resource for Mathematical Methods in Physics. John Wiley & Sons, (2008)

[137]   J. Van Wazer, Electron densities in molecular and molecular orbitals. Elsevier, (2012)

[138]   T. Pang, An Introduction to Computational Physics. Cambridge University Press, (2006)

[139]   J. Singh, Quantum Mechanics: Fundamentals and Applications to Technology. John Wiley & Sons, (2008)

[140]   J. Yates and J. Johnson, Molecular Physical Chemistry for Engineers. University Science Books, (2007)

[141]   J. Fan, Multiscale Analysis of Deformation and Failure of Materials. John Wiley & Sons, (2011)

[142]   F. Amirouche, Fundamentals of Multibody Dynamics: Theory and Applications. Birkhäuser, (2006)

[143]   P. Paneth and A. Dybala-Defratyka, Kinetics and Dynamics: From Nano- to Bio-Scale. Springer Science & Business Media, (2010)

[144]   H. Berendsen, Simulating the Physical World: Hierarchical Modeling from Quantum Mechanics to Fluid Dynamics. Cambridge University Press, (2007)

[145]   F. Weinhold and C. Landis, Discovering Chemistry With Natural Bond Orbitals. John Wiley & Sons, Inc., (2012)

[146]   E. Podgoršak and International Atomic Energy Agency, Radiation Oncology Physics: A HandBook for Teachers and Students. International Atomic Energy Agency, (2005)

[147]   M. Born and R. Oppenheimer, Zur Quantentheorie der Molekeln, Annalen der Physik, 389, 20, 457-484, (1927)

[148]   M. Tukkerman and G. Martyna, Understanding Modern Molecular Dynamics: Techniques and Applications, Physical Chemistry B, 104, 20, 159-178, (2000)

[149]   L. Verlet, Computer "Experiments" on Classical Fluids. I. Thermodynamical Properties of Lennard-Jones Molecules, Physical Review, 159, 1, 98-103, (1967)

[150]   J. Li, Basic Molecular Dynamics, In: HandBook of Materials Modelling, pp 565-588. Springer, (2005)

[151]   S.   Shell,   Advanced   molecular   dynamics   techniques,   June   2009, http://www.engr.ucsb.edu/ shell/che210d/

[152]   J. Cuevas and E. Scheer, Molecular Electronics: An Introduction to Theory and Experiment, World Scientific series in nanoscience and nanotechnology volume 1. World Scientific, (2010)

[153]   I. Mayer, Simple Theorems, proofs, and Derivations in Quantum Chemistry, Mathematical and Computational Chemistry series. Kluwer Academic/Plenum (2003)

[154]   F. Jansen, Introducion to Computational Chemistry. Wiley, (1999)

[155]   D. Marx and J. Hutter, Ab Initio Molecular Dynamics: Basic and Advanced Methods. Cambridge University Press, (2009)

[156]   A. Atta and H. E. Ali, Structural and Thermal Properties of PTFE Films by Argon and Oxygen Plasma, Arab Journal of Nuclear Science and Applications, 46, 5, 106-114, (2013)

[157]   S. Krause, Polymer-polymer miscibility, Pure and Applied Chemistry, 58, 12, 1553-1560, (1986)

[158]   S. Kumbharkar and U. Kharul, New N-substituted ABPBI: Synthesis and evaluation of gas permeation properties, Journal of Membrane Science, 360, 418-425, (2010)

[159]   B. Miller-Chou and J. Koenig, A review of polymer dissolution, Progress Polymer Science, 28, 1223-1270, (2003)

[160]   T. Richardson and E. Lokensgard, Industrial Plastics: Theory and Applications, pp 92. Thomson, (2004)

[161]   L. Pilato and M. Michno, Advanced Composite Materials. Springer-Verlang Berlin Heidelberg New York, (1994)

[162]   S. Ebnesajjad, Fluoroplastics, Volume 1: Non-Melt Processible Fluoroplastics. William Andrew, (2000)

[163]   X. Li, D. Moore and S. Iyengar, Insights from first principles molecular dynamics studies toward infrared multiple-photon and single-photon action spectroscopy; Case study of the proton-bound dimethyl ether dimer, Chemical Physics, 128, 184308, (2008)

[164]   E. Tsuchida, Ab Initio Molecular-Dynamics Simulation of Concentrated Phosphoric of phosphoric acid, Physical Society of Japan, 75, 5, 054801-1-054801-5,

160

(2006)

[165]   D. Ebbing and S. Gammon, General Chemistry 6th edition. Brooks Cole, (1999)

[166]   O. Olabis, Polymer-Polymer Miscibility. Elsevier, (2012)

[167]   Editors of the American Heritage Dictionaries, The American Heritage Science Dictionary, (2014)

[168]   D. Qi, J. Hinkley and G. He, Molecular dynamics simulation of thermal and mechanical properties of polyimide-carbon-nanotube composites, Modelling and Simulation in Materials Science and Engineering, 13, 493, (2005)

[169]   S. Shen and S. Atluri, Atomic-level Stress Calculation and Continuum-Molecular System Equivalence, Computer Modeling in Engineering and Sciences, 6, 1, 91-104, (2004)

[170]   C. Hoppel, T Bogetti and J. Gillespie(Jr.), Effects of Hydrostatic Pressure on the Behavior of Composite Materials, ARL-TR-727. U.S Army Research Laboratory, (1995)

[171]   K. Pae and S. Bhateja, The Effects of Hydrostatic Pressure on the Mechanical Behavior of Polymers, Journal of Macromolecular Science, 13, 1, 1-75, (1975)

[172]   P. Rae and D. Dattelbaum, The properties of poly(tetrafluoroethylene) (PTFE) in compression, Journal of Polymer, 45, 7615-7625, (2004)

[173]   J. Bernal and R. Fowler, A theory of water and ionic solution, with particular reference to hydrogen and hydroxyl ions, The Journal of Chemical Physics, 1, 8, 515-548, (1933)

[174]   S. Bose, T. Kuila, T. Nguyen, N. Kim and K. Lau, High temperature proton exchange membranes based on polybenzimidazoles for fuel cells, Progress in Polymer Science, 34, 449-477, (2009)

[175]   R. Gisbert, G. García and M. Koper, Adsorption of phosphate species on poly-oriented Pt and Pt(111) electrodes over a wide range of pH, Electrochimica Acta, 55, 52, 7961-7968, (2010)

[176]   T. Langkau and H. Baltruschat, The rate of anion and hydrogen adsorption on Pt(111) and Rh(111), Electrochimica Acta, 44, 909-918, (1998)

[177]   T. Arruda, B. Shyam, J. Ziegelbauer, S. Mukerjee and D. Ramaker, Investigation into the Competitive and Site-Specific Nature of Anion Adsorption of Pt Using In Situ X-ray absorption Spectroscopy, Journal of Physical Chemistry C, 112, 18087-18097, (2008)

[178]   T. Fukuda and A. Aramata, The kinetic study of specific adsorption of phosphate species on Pt(111) in acidic solutions, Journal of Electroanalytical Chemistry, 440, 153-161, (1997)

[179]   A. Kamat, M. Herrmann, D. Ternes, O. Klein, U. Krewer and S. Scholl, Experimental Investigation into Phosphoric Acid Adsorption on Platinum Catalysts in a High Temperature PEM Fuel Cell, Fuel Cells, 11, 511-517, (2011)

[180]   V. Tripkovic' , E. Skúlason , S. Siahrostami , J. Nørskov and J. Rossmeisl, The oxygen reduction reaction mechanism on Pt(111) from density functional theory calculations, Electrochemica Acta, 55, 7975-7981, (2010)

[181]   F. Nart and T. Iwasita, On the adsorption of $H_2PO_4^-$ and H_3PO_4 on platinum: an in situ FT-ir study, Electrochimica Acta, 37, 3, 385-391, (1992)

[182]   H. Kita, S. Ye, A. Aramata and N. Furuya, Adsorption of hydrogen on platinum single crystal electrodes in acid and alkali solutions, Journal of Electroanalytical Chemistry and Interfacial Electrochemistry, 295, 1-2, 317-331, (1990)

[183]   P. Hohenberg and W. Kohn, Inhomogeneous electron gas, Physical Review, 136, B864-B871, (1964)

[184]   W. Kohn and L. Sham, Self-consistent equations including exchange and correlation effects, Physical Review, 140, A1133-A1138, (1965)

[185]   M. Payne, M. Teter, D. Allan, T. Arias. and J. Joannopoulos, Iterative minimization techniques for ab initio total-energy calculations - molecular-dynamics and conjugate gradients, Reviews of Modern Physics, 64, 1045-1097, (1992)

[186]   S. Clark, M. Segall, C. Pickard, P. Hasnip, M. Probert, K. Refson and M. Payne, First principles methods using CASTEP, Zeitschrift für Kristallographie - Crystalline Materials, 220, 567-570, (2005)

[187]   E. O'Reilly, Quantum Theory of Solids. CRC Press, (2003)

[188]   M. Selvan and D. Keffer, Molecular-Level Modeling of the Structure and Proton Transport within the Membrane Electrode Assembly of Hydrogen Proton Exchange Membrane Fuel Cells, In: Theory and Experiment in Electrocatalysis, pp 133-202. Springer, (2010)

[189]   D. Tsai, The virial theorem and stress calculation in molecular dynamics, Chemical Physics, 70, 3, 1375, (1979)

[190] Y. Ma, The fundamental studies of polybenzimidazole/phosphoric acid polymer electrolyte for fuel cells, Case Western Reserve University, (2004)

[191] T. Dippel, K. Kreuer, J. Lassegues and D. Rodriguez, Proton conductivity in fused phosphoric acid; a 1 H/31 P PFG-NMR and QNS study, Solid State Ionics, 61, 1, 41-46, (1993)

[192] K. Kreuer, Fuel Cells Second Edition. Springer, (2012)

[193] P. Wilkinson, J. Zhang, R. Hui, J. Fergus and X. Li, Proton exchange membrane fuel cells: materials properties and performance. CRC Press, (2009)

[194] J. Perdew, A. Ruzsinszky, G. Csonka, O. Vydrov, G. Scuseria, L. Constantin, X. Zhou, K. Burke, Restoring the density-gradient expansion for exchange in solids and surfaces, Physical Review Letters, 100, 13, 136406, (2008)

[195] Z. Wu and R. Cohen, More accurate generalized gradient approximation for solids, Physical Review B, 73, 23, 235116, (2006)

[196] A. Dupuis, Proton exchange membranes for fuel cells operated at medium temperatures: Materials and experimental techniques. Progress in Material Science, pp. 289-327, (2010)

[197] Y. Lee, B. Bingöl, T. Murakhtina and D. Sebastiani, W. Meyer, G. Wegner, H. Spiess, High-resolution solid-state NMR studies of poly (vinyl phosphonic acid) proton-conducting polymer: Molecular structure and proton dynamics, The Journal of Physical Chemistry B, 111, 33, 9711-9721, (2007)

[198] G. Hoogers, Fuel Cell Technology Handbook. Washington DC. CRC Press LLC, (2003)

[199] Q. Li and J. Jensen, R. Savinell and N. Bjerrum, High temperature proton exchange membranes based on polybenzimidazoles for fuel cells, Progress in Polymer Science, 34, 5, 449-477, (2009)

[200] J. Zhang, Z. Xie, J. Zhang, Y. Tang, C. Song, T. Navessin, Z. Shi, D. Song, H. Wang, D. Wilkinson and others, High temperature PEM fuel cells, Journal of power Sources, 160, 2, 872-891, (2006)

[201] L. Yan, S. Zhu, X. Ji and W. Lu, Proton hopping in phosphoric acid solvated NAFION membrane: a molecular simulation study, The Journal of Physical Chemistry B, 111, 23, 6357-6363, (2007)

[202] S. Aharoni and M. Litt, Synthesis and some properties of poly-(2, 5-trimethylene benzimidazole) and poly-(2, 5-trimethylene benzimidazole hydrochloride), Journal of

163

Polymer Science: Polymer Chemistry Edition, 12, 3, 639-650, (1974)

[203]   J. Wainright, J. Wang, D. Weng, R. Savinell and M. Litt, Acid-Doped Polybenzimidazoles: A New Polymer Electrolyte, Journal of the Electrochemical Society, 142, 7, L121-L123, (1995)

[204]   K. Jiao, I. Alaefour and X. Li, Three-dimensional non-isothermal modeling of carbon monoxide poisoning in high temperature proton exchange membrane fuel cells with phosphoric acid doped polybenzimidazole membranes, Fuel, 90, 2, 568-582, (2011)

[205]   R. He, Q. Che and B. Sun, The acid doping behavior of polybenzimidazole membranes in phosphoric acid for proton exchange membrane fuel cells, Fibers and Polymers, 9, 6, 679-684, (2008)

[206]   K. Scott, S. Pilditch and M. Mamlouk, Modelling and experimental validation of a high temperature polymer electrolyte fuel cell, Journal of Applied Electrochemistry, 37, 11, 1245-1259, (2007)

[207]   Fuel Cell Today, The Fuel Cell Industry Review 2013. Johnson Matthey PLC trading, (2013)

[208]   S. Curtin and J. Gangi, 2013 Fuel Cell Technologies Market Report, U.S. Department of Energy Fuel Cell Technologies Office, (2014)

[209]   A. Tanaka, R. Adži c′ and B. Nikoli c′, Oxygen reduction on single crystal platinum electrodes in phosphoric acid solutions, Journal of Serberian Chemical Society, 64, 11, 695-705, (1999)

[210]   Q. He, X. Yang, W. Chen, S. Mukerjee and B. Koel, Influence of phosphate anion adsorption on the kinetics of oxygen electroreduction on low index Pt(hkl) single crystals, Physical Chemistry Chemical Physics, 12, 1254-1255, (2010)

[211]   M. Weber, F. Nart, I. de Moraes and T. Iwasita, Adsorption of Phosphate Species on Pt(111) and Pt(100) As Studied by in Situ FTIR Spectroscopy, Journal of Physical Chemistry, 100, 19933-19938, (1996)

[212]   N. Markovi c′, T. Schmidt, V Stamenkovi c′ and P. Ross, Oxygen Reduction Reaction on Pt and Pt Bimetallic Surfaces: A Selective Review, Fuel Cells, 1, 2, 105-116, (2001)

[213]   M. Boxwell, Solar Electricity Handbook: A Simple, Practical Guide to Solar Energy : how to Design and Install Photovoltaic Solar Electric Systems. Greenstream Publishing (2012)

[214]   R. Neville, Solar Energy Conversion: The Solar Cell. Elsevier Science, (1995)

164

[215]   SolarGIS©, 2015 GeoModel Solar

[216]   Ibp Incorporated, South Africa Investment and Business Guide Volume 1 Strategic and Practical Information. International Business Publications USA, (2013)

[217]   B. Verspagen, Mapping technological trajectories as patent citation networks: A study on the history of fuel cell research. Advances in Complex Systems 10.01, 93-115, (2007)

[218]   C. Spiegel, PEM Fuel Cell Modeling and Simulation Using Matlab. Elsevier Science, (2011)

[219]   L. Qingfeng, H. Hjuler and N. Bjerrum, Phosphoric acid doped polybenzimidazole membranes: Physiochemical characterization and fuel cell applications, Journal of Applied Electrochemistry, 31, 7, 773-779, (2001)

[220]   H. Bai and W Ho, Recent developments in fuel-processing and proton-exchange membranes for fuel cells, Polymer International 60, 1, 26-41, (2011)

[221]   N. Djilali, Computational modelling of polymer electrolyte membrane (PEM) fuel cells: challenges and opportunities. Energy 32, 4, 269-280, (2007)

[222]   J. Zhang, Z. Xie, J. Zhang, Y. Tang, C. Song, T. Navessin, Z. Shi, D. Song, H. Wang, D. Wilkinson, Z. Liu and S. Holdcroft, High temperature PEM fuel cells, Journal of Power Sources, 160, 2, 872-891, (2006)

[223]   N. Jalani, M. Ramani, K. Ohlsson, S. Buelte, G. Pacifico, R. Pollard, R. Staudt and R. Datta, Performance analysis and impedance spectral signatures of high temperature PBI-phosphoric acid gel membrane fuel cells, Journal of Power Sources, 160(2), 1096-1103, (2006)

[224]   R. He, Q. Che, and B. Sun, The acid doping behavior of polybenzimidazole membranes in phosphoric acid for proton exchange membrane fuel cells. Fibers and Polymers, 9(6), 679-684, (2008)

[225]   A. Shah, K. Luo, T. Ralph, and F.Walsh, Recent trends and developments in polymer electrolyte membrane fuel cell modelling, Electrochimica Acta 56, 11, 3731-3757, (2011)

[226]   W. Klunne, Hydropower database at hydro4Africa.

[227]   W. Van Zyl and B. Prior, South Africa biofuels. IEA Taskgroup, 39, (2009)

[228]   R. Cawthorn, The platinum group element deposits of the Bushveld Complex in

165

South Africa, Platinum Metals Review, 54(4), 205-215, (2010)

[229]   T. Ayodele, A. Jimoh, J. Munda, and J. Agee, Statistical analysis of wind speed and wind power potential of Port Elizabeth using Weibull parameters, Journal of Energy in Southern Africa, 23, 2, 31, (2012)

[230]   D. Newton, World Energy Crisis: A Reference Handbook, Contemporary world issues. ABC-CLIO, (2013)

[231]   R. Blanchard, D. Richardson, P. O'Farrell and G. Von Maltitz, Biofuels and biodiversity in South Africa. South African Journal of Science, 107(5-6), 19-26, (2011)

[232]   EARTH, URBAN, South African Carbon Snapshot, (2012)

[233]   Department of Energy of Republic of South Africa, Annual Performance Plan (2015/2016)

[234]   Department of Minerals and Energy Pretoria, Capacity Building in Energy Efficiency and Renewable Energy, Report No. 2.3.4-19, February 2004

[235]   R. Diab, Wind Atlas of South Africa. Department of Mineral and Energy Affairs, (1995)

[236]   R. Sharma, Future Power, Future Energy: Wind Power. The Energy and Resources Institute (TERI), (2008)

[237]   J. Cavanagh, J. Clarke and R. Price, Ocean energy systems. Renewable Energy: Sources for Fuels and Electricity, 513-547, (1993)

[238]   O. Edenhofer, R. Pichs-Madruga, Y. Sokona, K. Seyboth, S. Kadner, T. Zwickel, P. Eickemeier, G. Hansen, S. Schlömer, C. von Stechow, and P. Matschoss, Renewable Energy Sources and Climate Change Mitigation: Special Report of the Intergovernmental Panel on Climate Change. Cambridge University Press, (2011)

[239]   DME, Eskom, CSIR, 2001 South African Renewable Energy Resource Database,http://www.sabregen.co.za, date accessed: 1 October 2015

[240]   D. Banks and J. Schäffler. The potential contribution of renewable energy in South Africa. Draft Update Report (2006)

[241]   Department of Research and Information, Opportunities for downstream value addition in the platinum group metals value chain: Fuel cells, Industry analysis. February 2013

[242]   S. Barrett, HySA Infrastructure: producing and using hydrogen for energy in South

166

Africa, Fuel Cells Bulletin, 6, 12-17, (2013)

[243]   A. Edwards, M. Silk and Council for Mineral Technology (South Africa), Platinum in South Africa. Council for Mineral Technology, (1987)

[244]   T. Johansson and L. Burnham, Renewable Energy: Sources for Fuels and Electricity. Island Press, (1993)

[245]   J. Valenta and S. Mirabella, Nanotechnology and Photovoltaic Devices: Light Energy Harvesting with Group IV Nanostructures. Pan Stanford, (2015)

[246]   M. Kaltschmitt, W. Streicher and A. Wiese, Renewable Energy: Technology, Economics and Environment. Springer Berlin Heidelberg, (2007)

[247]   J. Van Wyk, South Africa's nuclear future, (2014)

[248] Map of Eskom power stations, http://www.eskom.co.za/Whatweredoing/ElectricityGeneration/PowerStations/Pages/Map_Of_Eskom_Power_Stations.aspx, date accessed: 5 November 2015

[249]   Eskom, COP17 fact sheet, Medupi and Kusile

[250]   S. Subianto, Recent advances in polybenzimidazole/phosphoric acid membranes for high-temperature fuel cells. Polymer International, 63, 7, 1134-1144, (2014)

[251]   W. Callister and D. Rethwisch, Fundamentals of Materials Science and Engineering: An Integrated Approach. Wiley, (2012)

[252]   H. Zheng, L. Petrik and M. Mathe, Preparation and characterisation of porous poly(2,5benzimidazole) (ABPBI) membranes using surfactants as templates for polymer electrolyte membrane fuel cells. International Journal of Hydrogen Energy, 35, 8, 3745 - 3750, (2010)

[253]   Y. Lebedev, Y. Korolev, V. Polikarpov, L. Ignat'eva and E. Antipov, X-ray powder diffraction study of polytetrafluoroethylene. Crystallography Reports, 55, 4, 609-614, (2010)

[254]   X. Bao, F. Zhang and Q. Liu, Sulfonated poly(2,5-benzimidazole) (ABPBI)/MMt/ionic liquids composite membrane for high temperature PEM applications. International Journal of Hydrogen Energy, 1-8, (2015)

[255]   International Energy Agency, IEA Key World Energy Statistics, (2015)

[256]   International Energy Agency (IEA) and World Bank Group, Sustainable Energy for All, 2013-2014: Global Tracking Framework Report (2014)

167

[257]   L. Van Vuuren, Water resource management : drought management - Strengthening our knowledge armoury : cover story. Water Wheel, 14, 6, 14-17, (2015)

[258]   S. Hedden and J. Cilliers, Parched prospects-the emerging water crisis in South Africa. Institute for Security Studies Papers, 11, (2014)

[259]   A. Eberhard, J. Kolker and J. Leigland, South Africa's Renewable Energy IPP Procurement Program: Success Factors and Lessons. World Bank Group, Washington, DC, (2014)

[260]   Concentrating solar power systems, Southern African Solar thermal and energy , http://sastela.org, date accessed: 1 December 2015

[261]   J. Zhang, PEM fuel cell electrocatalysts and catalyst layers: fundamentals and applications. Springer Science & Business Media, (2008)

[262]   S. Paddison, and K. Promislow, Device and materials modeling in PEM fuel cells (Vol. 113). Springer Science & Business Media, (2008)

[263]   J. Pukrushpan, A. Stefanopoulou and H. Peng, Modeling and control for PEM fuel cell stack system. In American Control Conference, 2002. Proceedings, 4, 3117-3122

[264]   T. Berning, D. Lu and N. Djilali, Three-dimensional computational analysis of transport phenomena in a PEM fuel cell. Journal of power sources, 106 ,1, 284-294, (2002)

[265]   A. Kazim, H. Liu and P. Forges, Modelling of performance of PEM fuel cells with conventional and interdigitated flow fields. Journal of Applied Electrochemistry, 29, 12, 1409-1416, (1999)

[266]   R. Salim, H. Noura, M. Nabag, and A. Fardoun, Modeling and Temperature Analysis of the Nexa 1.2 kW Fuel Cell System. Journal of Fuel Cell Science and Technology, (2015)

[267]   B. Saripella, U. Koylu and M. Leu, Experimental and Computational Evaluation of Performance and Water Management Characteristics of a Bio-inspired PEM Fuel Cell. Journal of Fuel Cell Science and Technology, (2015)

[268]   M. Quiroga, K. Malek, and A. Franco, A Multiparadigm Modeling Investigation of Membrane Chemical Degradation in PEM Fuel Cells. Journal of The Electrochemical Society, 163, 2, F59-F70, (2016)

[269]   A. Al-Ghamdi, E. Shalaan, F. Al-Hazmi, A. Faidah, S. Al-Heniti, M. Husain, Adsorption sites of hydrogen atom on pure and Mg-doped multi-walled carbon nanotubes. Journal of Nanomaterials, 2012, 89, (2012)

168

[270]   K. Khaled and A. El-Sherik, Using Molecular Dynamics Simulations and Genetic Function Approximation to Model Corrosion Inhibition of Iron in Chloride Solutions. International Journal of Electrochemical Science, 8, 10022-10043, (2013)

[271]   F. Bauer and M. Willert-Porada, Comparison between Nafion and a Nafion Zirconium Phosphate Nano-Composite in Fuel Cell Applications. Fuel Cells, 6(3-4), 261-269, (2006).

[272] T. Kim, T. Lim, Y. Park, K. Shin and J. Lee, Proton-Conducting Zirconium Pyrophosphate/Poly(2,5-benzimidazole) Composite Membranes Prepared by a PPA Direct Casting Method. Macromolecular Chemistry and Physics, 208, 21, (2007)

[273]   G. Alberti, M. Casciola, D. Capitani, A. Donnadio, R. Narducci, M. Pica and M. Sganappa, Novel Nafion–zirconium phosphate nanocomposite membranes with enhanced stability of proton conductivity at medium temperature and high relative humidity. Electrochimica Acta, 52, 28, 8125 - 8132, (2007)

[274]   D. Truffier-Boutry, A. De Geyer, L. Guetaz, O. Diat and G. Gebel, Structural Study of Zirconium Phosphate−Nafion Hybrid Membranes for High-Temperature Proton Exchange Membrane Fuel Cell Applications, Macromolecules, 40, 23, 8259-8264, (2007)

[275] G. Alberti, M. Casciola, A. Donnadio, R. Narducci, M. Pica and M. Sganappa, Preparation and properties of nafion membranes containing nanoparticles of zirconium phosphate. Desalination, 199(1), pp.280-282, (2006)

[276] C. Yang, S. Srinivasan, A. Bocarsly, S. Tulyani and J. Benziger, A comparison of physical properties and fuel cell performance of Nafion and zirconium phosphate/Nafion composite membranes. Journal of Membrane Science, 237, 1, 145-161, 2004

[277]   H. Zheng and M. Mathe, Enhanced conductivity and stability of composite membranes based on poly (2,5-benzimidazole) and zirconium oxide nanoparticles for fuel cells, Journal of Power Sources , 196, 3, 894 - 898, (2011)

[278] C. Dyer, P. Moseley, Z. Ogumi, D. Rand, B. Scrosati and J. Garche, Encyclopedia of Electrochemical Power Sources. Elsevier Science, (2013)

[279]   K. Shalabi, Y. Abdallah, H. Hassan and A. Fouda, Adsorption and corrosion inhibition of Atropa Belladonna extract on carbon steel in 1 M HCl solution. International Journal of Electrochemical Science, 9, pp.1468-1487, (2014)

[280]   J. Tan, L. Guo, T. Lv and S. Zhang, Experimental and Computational Evaluation of 3-indolebutyric Acid as a Corrosion Inhibitor for Mild Steel in Sulfuric Acid Solution. International Journal of Electrochemical Science, 10, pp.823-837, (2015)

[281]   L. Guo, X. Ren, Y. Zhou, S. Xu and Y. Gong. Monte Carlo simulations of corrosion inhibition of copper by two Schiff bases, (2015)

[282]   J. Tersoff, and D.Hamann. Theory of the scanning tunneling microscope. Scanning Tunneling Microscopy. Springer Netherlands, 59-67, (1985)

[283]   V. Inglezakis and A. Zorpas, Heat of adsorption, adsorption energy and activation energy in adsorption and ion exchange systems. Desalination and Water Treatment, 39(1-3), 149-157, (2012)

[284] R. Sharma, Chemistry of Chemical Bonding. Discovery Publishing House, (2007)

[285] A. Dupasquier, A Mills and Societ{\`a} italiana di fisica, Positron Spectroscopy of Solids, IOS Press, (1995)

[286] H. Matilla and Textile Institute (Manchester, England), Intelligent Textiles and Clothing, Woodhead publishing in textiles, Woodhead, (2006)

[287] U. Gedde, Polymer Physics, Springer, (1995)

[288] X. Duan, Material Science and Environmental Engineering: The Proceedings of 2016 International Workshop on Material Science and Environmental Engineering, World Scientific Publishing Company, (2016)

170